

*Crystal Orientations in Glass-Ceramics*

*determined using*

*Electron Backscatter Diffraction*

*(EBSD)*

**Dissertation**

zur Erlangung des akademischen Grades doctor rerum naturalium  
(Dr. rer. nat.)

vorgelegt dem Rat der Chemisch-Geowissenschaftlichen Fakultät der  
Friedrich-Schiller-Universität Jena

von Dipl. Ing. Wolfgang Wisniewski

geboren am 18.05.1982 in Jena

Gutachter:

1. Prof. Christian Rüssel  
(Otto-Schott-Institut, FSU Jena)
2. Prof. Thomas Höche  
(Fraunhofer Institut für Werkstoffmechanik, Halle)
3. Prof. Joachim Deubener  
(Institut für Nichtmetallische Werkstoffe, TU Clausthal)

Tag der öffentlichen Verteidigung: 04. Mai 2011

The experimental work for this thesis was done between October 2008 and December 2010 at the Otto-Schott-Institut of the Jena University under the guidance of Prof. Dr. C. Rüssel.

Die experimentelle Arbeit für diese Promotion wurde im Zeitraum zwischen Oktober 2008 und Dezember 2010 am Otto Schott Institut der Friedrich Schiller Universität Jena unter der Betreuung von Prof. Dr. C. Rüssel durchgeführt.

## **Zusammenfassung**

Im Rahmen dieser Arbeit wurden verschiedene glaskeramische Materialien hergestellt und mit verschiedenen Methoden charakterisiert, wobei der Schwerpunkt auf Untersuchungen mittels EBSD lag. Besonders die Untersuchung von Oberflächenkristallisation zeigte, dass bisherige Modelle über die Bildung orientierter Schichten auf diesem Weg falsch bzw. unvollständig waren und ermöglichte eine korrektere Beschreibung der auftretenden orientierten Schichten und deren Entstehung.

Auch die Untersuchung von Glaskeramiken die mittels elektrochemisch induzierter Keimbildung hergestellt wurden führte zu neuen Erkenntnissen wie z.B. der Detektion von abweichend orientierten Kristallen in den sonst extrem homogen orientierten Dendriten. Weiterhin wurde festgestellt, dass die Orientierung innerhalb gewachsener Mullitnadeln keineswegs homogen ist sondern vielmehr lokal variiert. Die bisher angenommen Orientierung der Mullitkristallen konnte auf den experimentellen Aufbau anstatt der Methode der Kristallisation zurückgeführt werden.

Letztlich konnten auch offenstehende Fragen über die Entstehung von Kristallen, die sowohl Hämatit als auch Magnetit enthalten, d.h. aus zwei Phasen bestehen, anhand der mit EBSD ermittelten Kristallorientierungen der beiden Phasen beantwortet werden.

Es kann folglich gesagt werden, dass EBSD erfolgreich auf glaskeramische Materialien angewendet werden konnte. Für Phasen die in keiner der verfügbaren EBSD-Datenbanken (TSL und AMCS) vorhanden waren konnten Materialdateien erstellt und erfolgreich optimiert werden. Es wurde gezeigt, dass die Möglichkeit Kristallorientierungen lokal zu messen neue Erkenntnisse über Keimbildung und Kristallisation bringen kann.

## Contents

1. Introduction.....	6
2. Electron Backscatter Diffraction.....	8
3. Publications:	
3.1. W. Wisniewski, M. Nagel, G. Völksch and C. Rüssel: <i>Electron Backscatter Diffraction of Fresnoite Crystals Grown from the Surface of a <math>2 \text{ BaO} \cdot \text{TiO}_2 \cdot 2.75 \text{ SiO}_2</math> Glass.</i> <i>Cryst. Growth Des.</i> , 2010, <b>10</b> , 1414- 1418. ....	14
3.2. W. Wisniewski, M. Nagel, G. Völksch and C. Rüssel: <i>New Insights into the Microstructure of Oriented Fresnoite Dendrites in the System <math>\text{Ba}_2\text{TiSi}_2\text{O}_8\text{-SiO}_2</math> Through Electron Backscatter Diffraction (EBSD).</i> <i>Cryst. Growth Des.</i> , 2010, <b>10</b> , 1939-1945. ....	20
3.3. W. Wisniewski, M. Nagel, G. Völksch and C. Rüssel: <i>Irregular Fourfold Hierarchy in Fresnoite Dendrites Grown via Electrochemically Induced Nucleation of a <math>\text{Ba}_2\text{TiSi}_{2.75}\text{O}_{9.5}</math> Glass.</i> <i>Cryst. Growth Des.</i> 2010, <b>10</b> , 4526-4530. ....	28
3.4. W. Wisniewski, T. Zscheckel, G. Völksch and C. Rüssel: <i>Electron Backscatter Diffraction of <math>\text{BaAl}_2\text{B}_2\text{O}_7</math> Crystals Grown from the Surface of a <math>\text{BaO} \cdot \text{Al}_2\text{O}_3 \cdot \text{B}_2\text{O}_3</math> Glass.</i> <i>CrystEngComm</i> 2010, <b>12</b> , 3105-3111. ....	34
3.5. R. Carl, W. Wisniewski and C. Rüssel: <i>Reactions During Electrochemically Induced Nucleation of Mullite from a <math>\text{MgO}/\text{Al}_2\text{O}_3/\text{TiO}_2/\text{SiO}_2/\text{B}_2\text{O}_3/\text{CaO}</math> Melt.</i> <i>Cryst. Growth Des.</i> , 2010, <b>10</b> , 3257-3262. ....	42
3.6. W. Wisniewski, R. Carl, G. Völksch, and C. Rüssel: <i>Mullite Needles Grown from a <math>\text{MgO}/\text{Al}_2\text{O}_3/\text{TiO}_2/\text{SiO}_2/\text{B}_2\text{O}_3/\text{CaO}</math> Glass Melt: Orientation and Diffusion Barriers.</i> <i>Cryst. Growth Des.</i> , DOI: 10.1021/cg101402r.....	49
3.7. W. Wisniewski, R. Harizanova, G. Völksch and C. Rüssel: <i>Crystallisation of Iron Containing Glass-Ceramics and the Transformation of Hematite to Magnetite.</i> <i>CrystEngComm</i> 2010, DOI:10.1039/C0CE00629G.....	57
4. Summary.....	65
5. References.....	69
6. Abbreviations.....	72
7. Presentations.....	73
8. Posters.....	73
9. Acknowledgements/ Danksagung.....	74
10. Statement/ Erklärung.....	75
11. Curriculum Vitae/ Lebenslauf (de).....	76

## 1. Introduction

Glass-ceramics are partially microcrystalline solids combining the properties of crystal phases with the properties of the amorphous glass phase surrounding them. They are usually produced by the controlled devitrification of glass during thermal annealing. Generally a glass is produced by melting the respective raw materials in a furnace and cooling the melt to inhibit nucleation and crystal growth. In a second step the amorphous solid is then heated to a defined temperature for a defined time during which nucleation and crystal growth occur.

Many materials with anisotropic properties have important applications, e.g. wood as construction material. Glass-ceramics show great potential for creating anisotropic materials with individually controlled mechanical, electromechanical or magnetic properties. Otherwise, glass-ceramics enable the production of small crystals in a desired size and shape if the glass matrix is selectively dissolved, e.g. by using an acid. Crystals in the form of needles or plates may increase the tensile and bending strength of glass-ceramic materials [1] while nano scale crystals of very narrow size distribution may affect various properties without affecting the transparency of the glass [2-4].

So called ultratransparent glass-ceramics, e. g. those containing rare-earth-doped metal fluoride crystals, are of interest with respect to their fluorescence [5], luminescence [6,7] and up conversion properties [8,9]. Crystallizing phases with desirable properties from a glass, e.g. fersnoite with its piezoelectric, pyroelectric and surface acoustic wave properties [10,11], may enable the fabrication of materials showing desired properties without the need to produce macroscopic single crystals. Oriented crystallization is essential if a glass-ceramic is meant to show properties similar to a single crystal of the targeted phase, especially if the lack of centrosymmetry is essential to achieve the respective properties.

Three principle routes have been proposed for the preparation of oriented non-metallic inorganic materials: kinetic control, mechanical deformation and thermodynamic control [12]. Kinetic control is based upon the combination of localized nucleation and subsequent anisotropic crystal growth, resulting in a kinetic selection and leading to an orientation of the crystals in some relationship to the fastest direction of crystal growth. Kinetic control finds application in the examples of surface crystallization [13-16], crystallization induced by electrochemical nucleation [17-22] as well as laser induced crystallization [23-26]. Mechanical deformation of melts occurs during the extrusion of a partially crystalline melt and may also lead to oriented glass-ceramics [27-31].

Thermodynamic control of crystal orientation would mean the crystals are oriented in some specific way to minimize their energy during nucleation or subsequent crystallization. While it has been reported that thermodynamics might contribute to nucleation at the surface and thus leading to a localized nucleation [32], oriented crystals resulting from such a nucleation would rather fit the profile of kinetic control as the nucleation itself is not oriented.

While asymmetric crystal growth can be caused by thermodynamic reasons, an oriented crystallization of a glass-ceramic would mean independent crystals are oriented in a specific way due to some thermodynamic reason and not simply localized nucleation followed by a kinetic selection of orientations through asymmetric crystal growth. Oriented nucleation, which would be the basic precondition for such a phenomenon, has not been proven to occur so far.

In order to enable the control and to predict the oriented growth of crystals in glass-ceramics, it is necessary to understand the growth mechanism in the respective preparation procedure. Concerning the surface crystallization of fresnoite type-crystals, for example, there is no consensus on the crystallization mechanism so far.

## 2. Electron Backscatter Diffraction (EBSD)

Utilizing the effect of EBSD to analyze materials in a scanning electron microscope (SEM) is based on the evaluation of diffraction patterns obtained from backscattered electrons called “electron backscattering patterns” (EBSPs). The patterns are formed by the interference of electrons diffracted at the lattice planes of a crystal under the Bragg-angle  $\Theta_B$ . Because the physical picture of EBSD is still incomplete the ultimate limitations of EBSD are still being debated. The following text is an explanation the author’s current understanding of the basics of EBSD-pattern formation without going into mathematical details of the physics involved.

### Energy of an Electron

The voltage  $U$  (usually 20 kV for EBSD analysis in a SEM) supplied between the anode and cathode of a SEM accelerates electrons to a kinetic energy  $E$  given by:

$$E = U \cdot e$$

where  $e$  is the charge of an electron ( $1.6 \cdot 10^{-19}$  C) [35].  $E$  is usually given in electronvolts (eV). The kinetic energy of 1 eV is gained if an electron passes through a potential difference of 1 V attributing an energy of about 20 keV to an electron accelerated with a voltage of 20 kV. An accelerating voltage of 20 kV was used in all the measurements featured in this thesis.

### Wavelength of an electron

The energy  $E$  of an electron can also be described as the wavelength  $\lambda$  of an electron which is given by the de Broglie relation

$$\lambda = h / p$$

where  $h$  is Planck’s constant and  $p$  is the momentum. In classic theory this leads to

$$\lambda = \frac{h}{p} = \frac{h}{\sqrt{2 \cdot m_0 \cdot E}}$$

Taking relativistic effects into account leads to

$$\lambda = \frac{h}{p} = \frac{h}{\sqrt{2 \cdot m_0 \cdot E \left( 1 + \frac{E}{2 \cdot E_0} \right)}}$$

where  $m_0$  is the rest mass of an electron ( $9.1091 \cdot 10^{-31}$  kg) and  $E_0 = m_0 \cdot c^2$ ,  $c$  being the velocity of light. Because discrepancies between the wavelengths resulting from the classic and relativistic approaches are small at 20 keV (0.97 % relative difference) but become large for electrons with an energy over 1000 keV (4.77 % relative difference), the classic approach is an acceptable simplification when considering electrons contributing to EBSD.



## Diffraction in a crystal lattice

The diffraction of electrons in a crystal lattice is described by Bragg's law [33]:

$$n\lambda = 2d_{hkl} \cdot \sin\Theta$$

where  $n\lambda$  are  $n$  multiples of the electron wavelength  $\lambda$ ,  $d_{hkl}$  is the spacing of the respective lattice planes and  $\Theta$  is the angle under which diffraction occurs. For EBSD the Bragg angle  $\Theta_B$  is of special importance because here diffraction occurs in the form of reflection at the lattice plane, thus enabling the constructive interference of the reflected electrons. Only one Bragg-angle  $\Theta_B$  can occur for a specific lattice plane spacing  $d_{hkl}$  and a specific wavelength  $\lambda$ .  $\Theta_B$  usually assumes values in the order of  $0.5^\circ$  for EBSD [33]. For example a Bragg-angle of  $\Theta_B \approx 0.46^\circ$  occurs for electrons with  $\lambda \approx 0.0088$  nm (20 keV electron energy) and  $d_{hkl} \approx 0.543$  nm ( $d_{001}$  in silicon). Because  $\sin \Theta$  can reach a maximum value of 1, Bragg's law only makes sense for  $\lambda < 2d_{hkl}$ .

In the case of EBSD, electrons with a spectrum of energies contribute to the formation of an electron backscattering pattern (EBSP) [34] from a number of lattice planes, which means a spectrum of Bragg-angles occurs. It has been shown that the main contribution to an EBSP comes from electrons with a residual energy of 19.5 keV, if an excitation of 20 keV is used, while electrons with 16 keV (an energy loss of 20 %) still contribute to an EBSP [34]. The attributed Bragg-angles are  $0.457^\circ$  for 20 keV,  $0.463^\circ$  for 19.5 keV and  $0.511^\circ$  for 16 keV. Fig. 1 illustrates the occurring variations in the Bragg-angles by presenting the tenfold values of  $\Theta$  for the given electron energies.

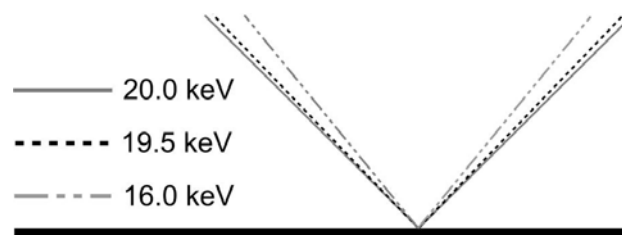


Fig. 1: Tenfold angles of Bragg-reflection at the (001) plane of Si for electrons of the given energies contributing to an EBSP

Fig. 2 illustrates how a path difference occurs between the electron beams B1 and B3 due to the longer distance traveled. While the beams B1 and B3 can constructively interfere, beam B2 leads to extinction due to the angular phase shift by  $\pi$  (which can also be described as a wave shift by  $\lambda/2$ ), if interference with B1 or B3 occurs. While the constructive interference is essential for EBSP-formation, extinction explains why certain lattice plains cannot contribute

to an EBSP. Generally extinction occurs if equivalent lattice planes are positioned half way between two lattice planes in Bragg-reflection position [33]. In the case of body centered crystal structures this is the case e.g. if  $\sum (h+k+l)$  is an odd number [33]. If the result is, however, an even number, the electrons can interfere constructively.

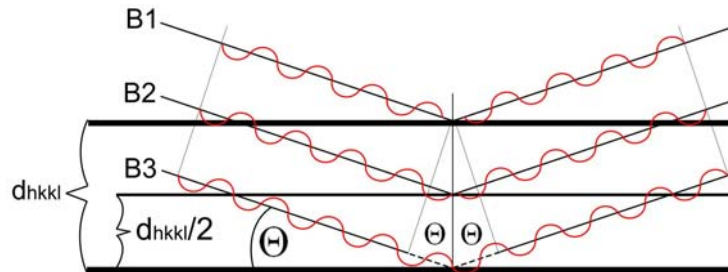


Fig. 2: Extinction and Bragg Reflection at a crystal lattice

### Distribution of Backscattered Electrons (BSEs)

The intensity of the backscatter signal emitted from an Al sample excited by electrons with an energy of 20 keV over the tilt angle is presented in Fig. 3 a) [35] and shows a maximum at  $63^\circ$ . In order to maximize the signal at the detector screen sample is tilted by  $70^\circ$  for EBSD-analysis. The intensity of the backscatter signal resulting from the sample tilt is outlined in Fig. 3 b). The diffraction signal utilized for EBSD is only an approximate 5 % signal on top of the forward scattered intensity distribution of 95 % making up the background signal [33].

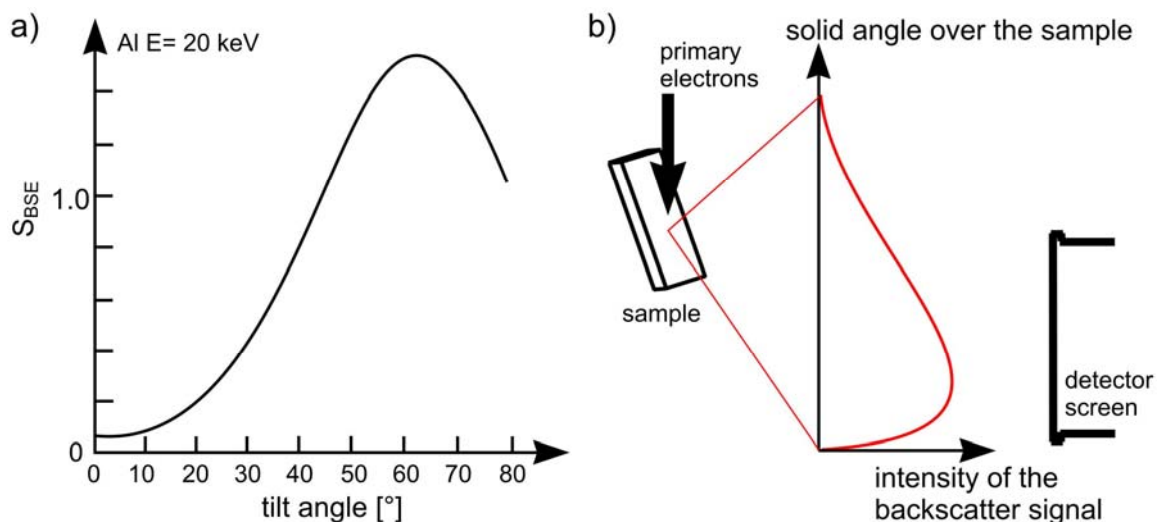


Fig. 3: a) Distribution of backscattered electrons over tilt angle [35],  
b) Intensity of the backscattered signal over a sample tilted by  $70^\circ$

## EBSP-formation

A part of the incoming primary electron beam is inelastically scattered in the solid. Because of the commonly applied sample tilt of  $70^\circ$  and the fact that most of the electrons contributing to an EBSP cannot suffer significant energy loss (the main contribution to an EBSP is from electrons with 97 % of the beam energy [34]), the main part of the electrons relevant to EBSP-formation are scattered along the original direction of the incoming beam (forward scattering).

It has been stated that the problem “diffraction from a point source inside a crystal” and the problem “diffraction of an incoming electron beam by a crystal leading to a certain electron intensity at the emitting atoms positions” are equivalent [36] due to the reciprocity principle [37]. Thus it can be assumed that localized electron sources emitting in all directions are created beneath the surface of the sample by the incoming electron beam.

Fig. 4 a) illustrates how electrons emitted from the source Q would be reflected at the (010) and (021) planes of the presented lattice due to diffraction under the Bragg angle  $\Theta_B$ . The electrons are reflected at each “side” of the lattice planes, hence producing two maxima close to each other on the detector screen.

Because reflection at the lattice planes occurs in all directions, the locus of the diffracted radiation is the surface of a cone at each side of the lattice plane with the half apex angle of  $90 - \Theta_B$  around the normal of the lattice plane as illustrated by Fig. 4 b) [33]. These cones are called Kossel-cones [33]. Due to the flatness of the Kossel-cones their area of interaction with the detector screen appears as bands, which were first detected by Kikuchi in 1929 and hence named Kikuchi Bands. The two Kossel Cones hence also contribute to the typical “Top Hat”-intensity profile of the Kikuchi Bands [33].

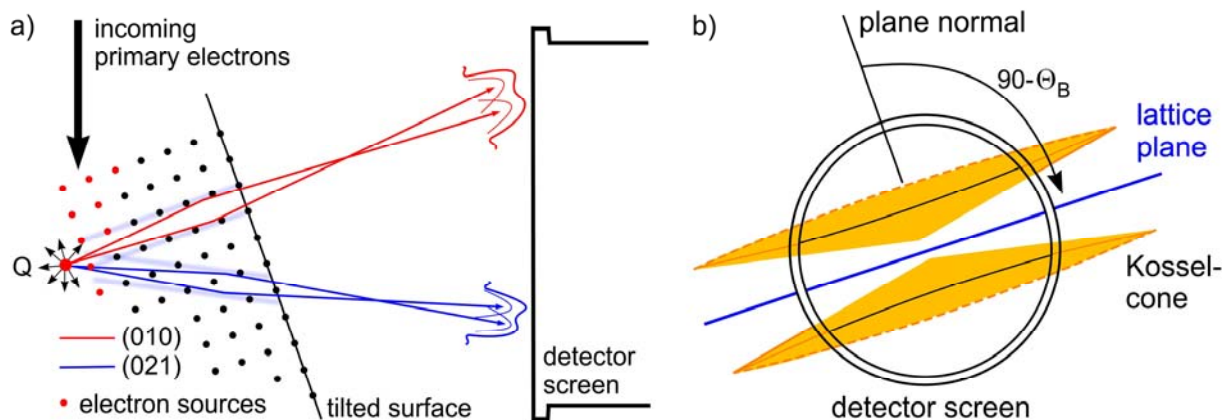


Fig. 4: a) Bragg-reflection of electrons from a local electron source Q at the (010) and (021) lattice planes leading to a signal on the detector screen  
b) Position of the Kossel cones of a lattice plane in respect to the detector

### Geometrical setup of an EBSD-system

The general principle of the geometric setup of EBSD-analysis is illustrated in Fig. 5: the incoming electron beam interacts with the tilted sample in an asymmetrically shaped interaction volume, where electron sources emitting in all directions are assumed to form. While most of the electrons are actually forward scattered and can be utilized to obtain an image through the forward scatter detector, some are diffracted at lattice planes under the Bragg angle along two Kossel cones per set of lattice planes. The thus diffracted electrons can interfere constructively and thus form a band of high intensity on the phosphor screen serving as the detector. An image of this screen is then obtained during a time of exposure defined by the user via a CCD-camera positioned behind the phosphor screen. This image is the Electron Backscattering Pattern (EBSP) later evaluated by the software.

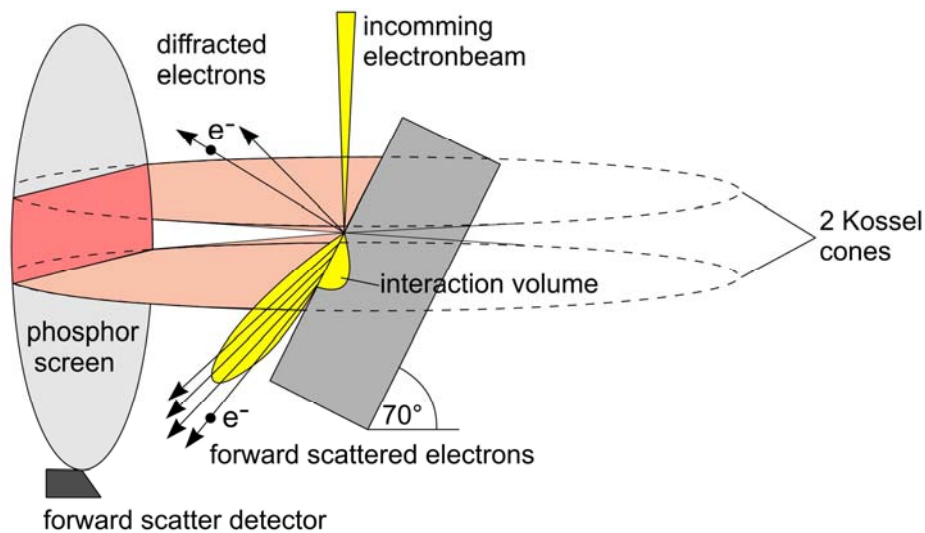


Fig. 5: Electron interaction leading to EBSP formation and arrangement of an EBSD-system

EBSD is a powerful tool for the local detection of crystal orientations and for the identification of certain crystal phases in the microstructure. The method is based on the analysis of Kikuchi bands detected in diffraction patterns obtained from a crystalline sample. The information depth of EBSD is limited to 10-50 nm [33, 38-43]. Hence EBSD is a method for the surface near characterization of materials. Using a scanning electron microscope (SEM) equipped with an EBSD-unit combines the ability of studying the morphology and crystallographic relationships of a crystalline solid simultaneously.

Although EBSD became a standard method in mineralogy [44,45], geology [46,47], ceramic materials [48-50] as well as metallographic science [51-54] during the past decade, no reports of EBSD as a method to characterize glass-ceramics could be found in the literature before 2009 apart from two papers containing work by Völksch et al. [55,56]. While the further development of technology has enabled 3D-analysis of materials via EBSD [57,58], a review on the applications of EBSD in materials science published in 2009 [59] does not mention the investigation of glass-ceramics. The first application of EBSD to glass-ceramics containing hematite/magnetite [55] and mullite [56] showed that it was possible to obtain evaluable EBSD-patterns from glass-ceramic materials and initiated further commitment to the field. Problems such as polishing procedures and building material files for phases previously not analyzed by EBSD could be identified and solved for a number of phases, making the application of EBSD to glass ceramic materials a promising field for scientific research.

### 3.1.

W. Wisniewski, M. Nagel, G. Völksch and C. Rüssel

#### **Electron Backscatter Diffraction of Fresnoite Crystals Grown from the Surface of a 2 BaO · TiO<sub>2</sub> · 2.75 SiO<sub>2</sub> Glass**

Crystal Growth & Design, 2010, **10**, 1414-1418.

<http://pubs.acs.org/doi/abs/10.1021/cg901407d?prevSearch=%2528Wisniewski%2529%2BNOT%2B%255Batype%253A%2Bad%255D%2BNOT%2B%255Batype%253A%2Bacstoc%255D&searchHistoryKey=>

## Electron Backscatter Diffraction of Fresnoite Crystals Grown from the Surface of a $2\text{BaO} \cdot \text{TiO}_2 \cdot 2.75\text{SiO}_2$ Glass

Wolfgang Wisniewski, Marcus Nagel, Günter Völksch, and Christian Rüssel\*

*Otto-Schott-Institut, Jena University, Fraunhoferstrasse 6, 07743 Jena, Germany**Received November 10, 2009; Revised Manuscript Received December 14, 2009*

**ABSTRACT:** A glass with the composition  $2\text{BaO} \cdot \text{TiO}_2 \cdot 2.75\text{SiO}_2$  was annealed at 810 °C for 20 h. This led to surface crystallization. Immediately at the surface of the sample, a layer of  $\text{Ba}_2\text{TiSi}_2\text{O}_8$ -type fresnoite crystals (layer I), with a thickness of approximately 7  $\mu\text{m}$ , oriented with the crystallographic [101]-direction perpendicular to the surface, was formed. The pole of the (001)-plane rotates randomly around the [101]-direction. It is assumed that nucleation kinetics is decisive to the direction of growth. In the next layer (layer II), the crystals are oriented with the crystallographic [001]-direction (*c*-axis) perpendicular to the surface of the sample. This layer occurs at a distance of 7–60  $\mu\text{m}$  from the surface. Here, crystals that are not oriented in that way hinder each other during crystal growth. At a distance > 60  $\mu\text{m}$ , the orientation of the fresnoite crystals is random and is the result of volume crystallization. The main characterization method is electron backscatter diffraction/orientation imaging microscopy.

### 1. Introduction

In the literature, numerous methods for the preparation of oriented glass-ceramics containing fresnoite are described. In principle, various routes have been proposed for the preparation of oriented nonmetallic inorganic materials.<sup>1</sup> In the past, the electrochemical nucleation,<sup>2–4</sup> laser-induced crystallization,<sup>5,6</sup> and surface crystallization were the most frequently used methods for the formation of a preferential orientation in barium titanium silicate<sup>7–9</sup> and the corresponding germanates.<sup>7,10–13</sup> Because of the macroscopic polar structures obtained (e.g., by surface crystallization) fresnoite glass-ceramics show an interesting combination of piezoelectric, pyroelectric, and surface acoustic wave properties.<sup>14,15</sup> In comparison to ferroelectric materials, fresnoite possesses a much smaller dielectric constant and hence is an advantageous piezoelectric material, especially for high frequency applications. Furthermore, it is also an interesting material for second harmonic generation.<sup>16–18</sup>

To enable the control and to predict the oriented growth of crystals in such a material, it is necessary to understand the growth mechanism in the respective preparation procedure. It has been speculated by Masai et al. that during surface crystallization, benitoite, a barium-rich phase, is necessary for the formation of fresnoite, oriented with its crystallographic *c*-axis perpendicular to the surface.<sup>12</sup> In a paper published by Ochi et al., oriented  $\text{Ba}_2\text{TiSi}_2\text{O}_8$  crystals with a length of up to about 500  $\mu\text{m}$  were achieved by surface crystallization using a thermal gradient and a crystallization temperature of 850 °C.<sup>19</sup> Concerning the surface crystallization of fresnoite type-crystals, there is no consensus on the crystallization mechanism so far.

This paper will present new insight into the microstructure and the orientation of fresnoite crystals in glass-ceramics prepared by surface nucleation of a glass with the composition  $2\text{BaO} \cdot \text{TiO}_2 \cdot 2.75 \text{SiO}_2$ . The predominantly used method was electron backscatter diffraction (EBSD).

### 2. Electron Backscatter Diffraction

In the past few years, EBSD became a standard method in mineralogy and metallographic science. By contrast, few reports of EBSD as a method to characterize glass-ceramics are found in the literature apart from two papers published by Völksch et al.<sup>20,21</sup> A recent review on the applications of EBSD in materials science given by Randle<sup>22</sup> also does not mention the investigation of glass-ceramics.

EBSD is a powerful tool for the identification of certain crystal phases in the microstructure and for the local detection of crystal orientations. The method is based on the analysis of Kikuchi bands detected in diffraction patterns obtained from a crystalline sample. The information depth of EBSD is limited to 10–50 nm.<sup>23,24</sup> Hence, EBSD is a method for the surface near characterization of materials.

Using a scanning electron microscope (SEM) equipped with an EBSD-unit combines the ability of studying the morphology and crystallographic relationships of a crystalline solid simultaneously.

While a single EBSD pattern provides information on the crystal at the spot where it was obtained, a grid of EBSD patterns allows the description of the crystallographic properties of a microstructure and is referred to as orientation imaging microscopy (OIM). The latter describes scanning a surface in a defined step size and collecting and indexing EBSD patterns so that each point in an OIM map represents the information of an indexed EBSD pattern. Indexing a diffraction pattern is achieved by a voting system (see e.g., Schwartz et al.<sup>23</sup>).

The orientation of a crystal is usually defined by the three Euler-angles  $\varphi_1$ ,  $\Phi$ , and  $\varphi_2$ . Other useful parameters describing an indexed pattern are the image quality value (IQ) and the confidence index (CI).

The IQ value of an EBSD-pattern is affected by numerous parameters; however, the main input from the sample is the perfection of the crystal lattice.<sup>23</sup> Since glass has no lattice to produce a diffraction pattern, points in an IQ map obtained from glass get very low IQ values, making the IQ value a very

\*Corresponding author. Tel: (0049) 03641 948501. Fax: (0049) 03641 948502. E-mail: ccr@uni-jena.de.

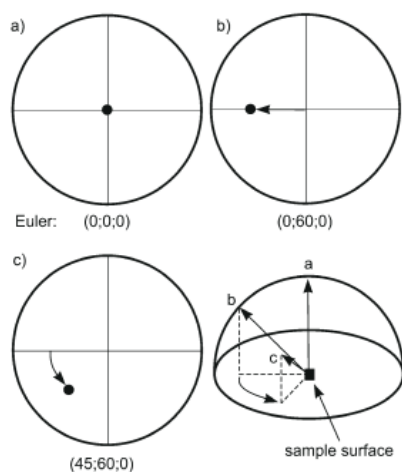


**Figure 1.** Effect of Euler angles on the (001)-pole figure of fresnoite. (a) Starting point, (b) variation of  $\Phi$ , (c) variation of  $\varphi_1$ , (d) variation of  $\varphi_2$ .

good filter to distinguish between amorphous and crystalline phases. A relatively low IQ value, in principle, should also be a result of a very thin layer of glass covering a crystal or tensions and defects within the crystal lattice.

The CI is a value calculated from the votes obtained from different orientation solutions for a phase used to index a pattern.<sup>23</sup> With respect to patterns obtained from an fcc-material, it was found that a solution was correct in 95% of the cases when the CI was 0.1 or greater and at least six Kikuchi bands were detected.

The (001) pole figure (PF) is very suitable to illustrate orientations of fresnoite, since the pole of the (001)-plane is parallel to the crystallographic  $c$ -axis of the unit cell. An example is shown in Figure 1. Here, the effects of the individual Euler angles ( $\varphi_1$ ;  $\Phi$ ;  $\varphi_2$ ) on the (001)-PF of fresnoite are presented. The Euler combination of (0;0;0) in Figure 1a describes a unit cell with the  $c$ -axis perpendicular to the surface of the sample;  $\Phi$  describes the tilt between the  $c$ -axis and the normal of the sample (Figure 1b). The rotation of the  $c$ -axis around the normal of the sample is described by  $\varphi_1$  (Figure 1c) and  $\varphi_2$  is a rotation around the  $c$ -axis and therefore has no input into the (001)-PF of fresnoite.

An inverse pole figure (IPF) is a reduction of the pole figure by symmetric operations to a unit triangle containing all orientations or their symmetric equivalents. It is therefore a useful plot for an overview of all orientations appearing in a scan.

### 3. Experimental Procedures

A glass with the composition  $2\text{BaO} \cdot \text{TiO}_2 \cdot 2.75 \text{SiO}_2$  (fresnoite +  $0.75 \text{SiO}_2$ ) was prepared from  $\text{BaCO}_3$ ,  $\text{TiO}_2$ , and  $\text{SiO}_2$  (quartz). The compounds were mixed and melted in a platinum crucible (250 mL) at  $1550^\circ\text{C}$  using an inductively heated furnace. After 1 h soaking at  $1550^\circ\text{C}$ , the melt was stirred for another 1 h and subsequently poured on a copper block. In order to avoid crystallization, the poured melt was quenched using another copper plate. The glass was analyzed by a differential thermal analyzer (DTA, Hartmann & Braun). To remove any possible nuclei at the surface which may have formed during quenching, one side of the sample was ground and polished with colloidal silica. Crystallization was carried out by a one-step annealing process at 80 K over  $T_g$  at  $810^\circ\text{C}$  for 20 h; the cooling rate was 3 K/min. After cutting the glass-ceramics perpendicular to the surface, the cut area and the surface of the samples were analyzed by X-ray diffraction (XRD, Siemens D5000) using  $\text{Cu K}\alpha$  radiation.

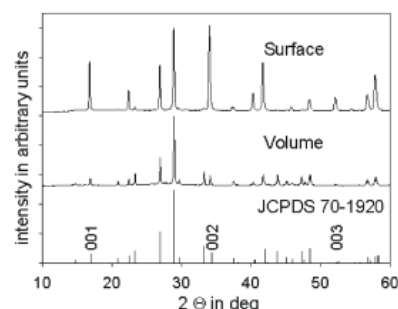


**Figure 2.** XRD patterns recorded from the volume and surface in comparison to the intensities according to the JCPDS-file 70-1920.

The samples were further characterized using a Jeol JSM-7001F FEG-SEM equipped with a TSL Digiview 1913 EBSD-Camera. OIM-scans were captured and evaluated using the programs TSL OIM Data Collection 5.31 and TSL OIM Analysis 5.

To achieve a conductive surface, the sample was mounted using Ag-paste and coated with a thin layer of carbon at about  $1 \times 10^{-5}$  mbar.

First EBSD measurements were performed on the surface of the sample after the crystallization without any polishing or further pretreatment.

The sample was then embedded in Araldite CY 212, a polymer adequate for vacuum application, to stabilize the edge during the polishing procedure necessary to reveal the crystals from the side. About 3 mm of the sample was then ground away in order to eliminate any effects of the original edges. The sample was then manually polished with diamond suspension of decreasing grain sizes (down to  $0.75 \mu\text{m}$ ). To obtain acceptable EBSD patterns, a final finish of 30 min using colloidal silica was applied.

In order to study the crystallization at the primary surface, 18 slightly overlapping scans covering all interesting parts of the sample were performed. The scans were performed using a voltage of 20 kV, resulting in a current of 12.5 nA. A binning of  $4 \times 4$  was applied and the used step size was 100 nm. Altogether, 12 Kikuchi Bands were detected during the indexing procedure.

Textures of these scans were calculated using discrete binning with a bin size of  $5^\circ$ , a Gaussian smoothing of  $5^\circ$ , and no sample symmetry. Only points with a minimum CI of 0.1 and an IQ value over 20% of the respective IQ distribution were considered in these calculations.

### 4. Results

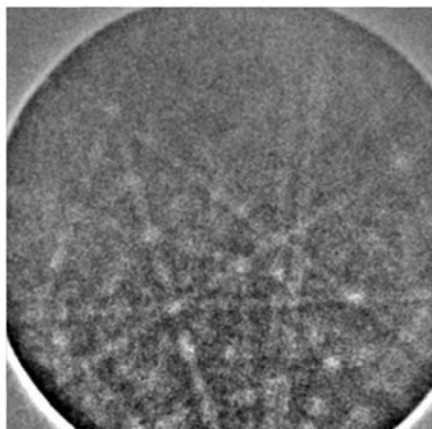
DTA measurements of the glass showed the glass transition temperature  $T_g$  to be  $730^\circ\text{C}$ , the crystallization onset temperature  $T_x$  to be  $830^\circ\text{C}$ , and the crystallization peak  $T_p$  to be at  $883^\circ\text{C}$ . After annealing the sample is fully opaque, although some transparent regions were found below the previous surface after polishing the side of the sample.

In Figure 2, an XRD pattern from the surface and the area cut perpendicular to the surface of the annealed sample is shown. The pattern shows lines all attributed to stoichiometric  $\text{Ba}_2\text{TiSi}_2\text{O}_8$  (JCPDS no.: 70-1920), while benitoite (JCPDS nos.: 76-1745 and 72-1591) was not detected. The intensities of the 001-, 002-, and 003-lines in the pattern attributed to the surface are much more intense than in that recorded from the volume.

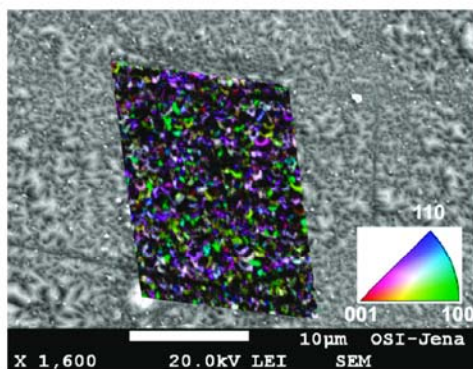
From the unpolished surface of the sample acceptable EBSD patterns (Figure 3) were obtained. Since XRD measurements proved that the sample contained only fresnoite as the crystalline phase, only this phase was used for indexing the EBSD patterns obtained from the entire sample. Nevertheless, also from the EBSD patterns, there was no hint of the occurrence of any additional crystalline phase.

Figure 4 shows the IPF map of an OIM scan performed on the unpolished surface of the annealed sample. While there is





**Figure 3.** EBSD pattern obtained from the unpolished surface of the sample.



**Figure 4.** SEM image of the untreated surface overlaid with the IPF map of the OIM scan performed in the area.

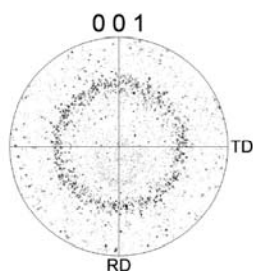


**Figure 5.** (001)-pole figure of the surface scan presented in Figure 4.

no single dominant orientation, orientations marked bluish green and purple in the IPF seem to appear more often than orientations marked red and yellow for example. The map contains only points with an IQ value  $> 20\%$ . This enables the elimination of the effect of the glass matrix as well as possible.

The (001)-pole figure (PF) of this scan (Figure 5) shows a significant ring located at a  $\Phi$ -angle of around  $58^\circ$ . The histogram of all the  $\Phi$ -angles in the PF is shown in Figure 6. Here, a well-pronounced peak between  $55^\circ$  and  $65^\circ$  is observed. To avoid two peaks representing pseudosymmetric orientations, the  $90$  to  $180^\circ$ -range of  $\Phi$  was mirrored into a  $0$  to  $90^\circ$ -histogram by transforming all  $\Phi$ -values over  $90^\circ$  by

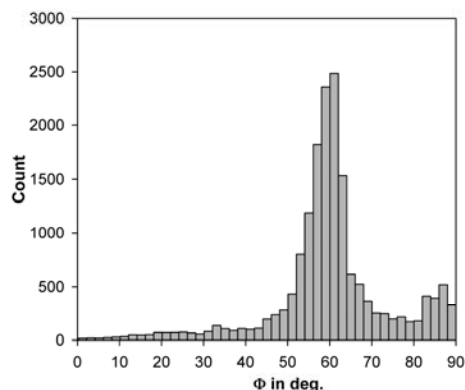


**Figure 6.** Histogram of the  $\Phi$ -angles obtained from the scan in Figure 4 and mirrored into a  $90^\circ$  range.

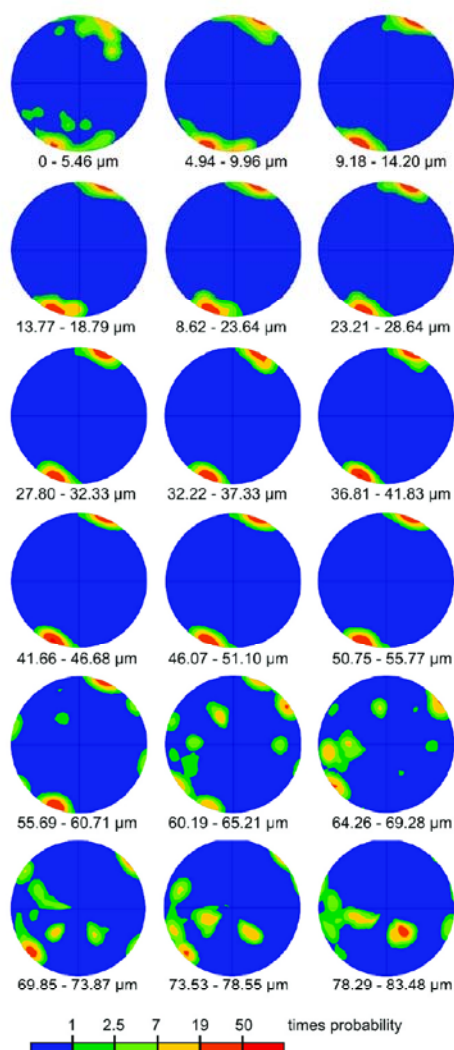
applying  $\Phi^* = 180 - \Phi$ . Here, only points with an IQ value of at least  $20\%$  of the IQ distribution were considered. This was done to exclude points attributed to the amorphous glass matrix. This surface layer is denoted in the following as layer I.

Figure 7 shows (001)-pole figures of the calculated textures of the 18 scans obtained from areas with an increasing distance from the primary surface. The legend describes the probability of finding an orientation. The values are attributed to relative probabilities; in a totally random distribution, this probability would be unity for every orientation. This means that the probability of finding a point in the respective scan belonging to an orientation marked red in Figure 7 is at least 50 times higher than in a randomly oriented material. In Figure 7, an equal area-version of the pole figure was used since the usual stereographic projection contains a distortion of the presented angles. The first two plots (distance from the surface up to around  $10\ \mu\text{m}$ ) show a rather broad distribution of orientations. From about  $10$  to  $55\ \mu\text{m}$  below the surface, the distribution narrows significantly and two pseudosymmetric orientations predominantly occur (orientations which deliver the same EBSD pattern). The plots of the oriented areas implicate the  $c$ -axes roughly parallel to the current surface and therefore practically perpendicular to the original surface. This layer is denoted in the following as layer II.

At a distance  $> 60\ \mu\text{m}$  from the surface, the distribution becomes more random, containing some crystals with their  $c$ -axes practically parallel to the original surface of the sample. All data points shown in Figure 7 have a minimum CI value of  $0.1$  and a minimum IQ value of  $20\%$  of the respective maximum value of each scan. This was done in order to exclude the glass matrix and unreliably indexed points.

To review the entire scanned area, the 18 slightly overlapping scans were merged together. In Figure 8, the IPF map of the merged scans overlaying an SEM image of the scanned area is presented. At the outer left part of Figure 8, the thickness of the oriented layer is notably smaller in comparison to other parts of the scanned area. Altogether the thickness of the oriented layer was found to vary from less than  $10$  to  $80\ \mu\text{m}$  in different parts of the sample. Most frequently, a layer thickness of  $80\ \mu\text{m}$  was found in areas where the surface crystallized layer was not in contact with areas exhibiting volume crystallization.

In the topmost  $10\ \mu\text{m}$  of the scan, a large number of small crystals are found which are not oriented with their  $c$ -axes perpendicular to the surface (layer I). Figure 9 shows the IPF map of the first three performed scans merged together. It can



**Figure 7.** Equal area (001)-pole figures of the textures calculated from the consecutive scans starting at the edge and finishing 83.48  $\mu\text{m}$  below the primary surface. The legend describes the relative probability of the orientations.

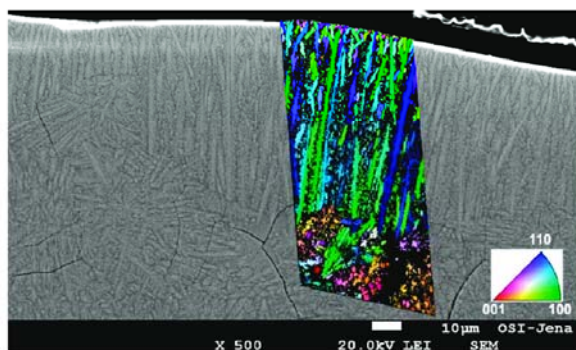


**Figure 8.** IPF map of the 18 merged OIM scans performed from the former surface into the volume of the sample overlaying the SEM image of the area.

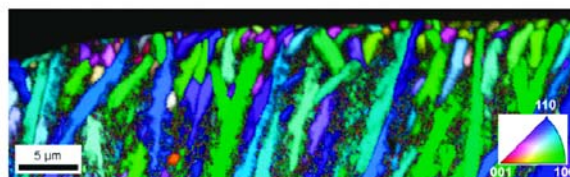


**Figure 9.** IPF map of the merger of the first three scans at the edge of the sample.

be seen that only the crystals growing more or less perpendicular to the surface continue to grow, while the crystals with a smaller angle with respect to the surface are blocked and do not grow continuously into the bulk.

## 5. Discussion

The composition  $2\text{BaO} \cdot \text{TiO}_2 \cdot 2.75 \text{SiO}_2$  was used because the glass is easier to produce with a smaller tendency toward crystallization in comparison to the stoichiometric composition.

The temperatures  $T_g$ ,  $T_x$ , and  $T_p$  obtained by DTA are higher for the prepared glass than the values published for the stoichiometric composition.<sup>8</sup> The higher  $\text{SiO}_2$  concentration in the glass leads to a higher crystallization temperature as previously reported.<sup>25</sup> The sample presented in this paper was part of a series of heat treatments performed from 790 to 850  $^\circ\text{C}$  and one of the first that lead to surface-oriented fresnoite.

As seen in the XRD patterns, the crystallized sample shows only lines attributed to stoichiometric fresnoite. No solid solutions are formed during crystallization, but the chemical composition of the residual glass phase is changed, leading to a higher  $\text{SiO}_2$  content.<sup>26</sup> Because of the fast growth in the [001]-direction, it can be assumed that the crystals will first appear as thin, isolated needles and then widen to the structures seen in Figure 8. The remaining  $\text{SiO}_2$  enriched glass is therefore not pushed ahead of the crystallization front, but remains in between the crystals, resulting in the black areas in the OIM scan presented in Figure 8. There was no hint of the occurrence of other crystal phases such as benitoite. The differences in the intensities of the respective XRD lines in the patterns recorded at the surface and the bulk are already a hint of an orientation. For example, the 002-peak which according to the JCPDS file has a relatively intensity of 20% is the most intense. By analogy, also the intensities of the 001- and the 003-peaks of the pattern recorded from the surface are much larger than those observed in the bulk and also than those of the JCPDS-file 70-1920. Hence, it can be concluded from the XRD patterns that the crystallographic  $c$ -axis of fresnoite is oriented perpendicular to the surface near the surface of the sample.

From the annealed surface of the sample, high-quality EBSD patterns were obtained (Figure 3). This proves that the crystals are not covered by a thin layer of glass (larger than a few nanometers) but are part of the surface of the sample. The fresnoite crystals occur immediately at the surface of the sample and hence should initially be formed at the surface. The pole figure of the scan on this surface shows that the topmost layer of crystals is highly oriented. A ring at a value of  $\Phi = 58 \pm 5^\circ$  indicates a preference of surface near crystals with their crystallographic  $c$ -axes in an angle of  $58^\circ$  to the surface. An angle  $\Phi = 58^\circ$  is attributed to an orientation of the crystallographic [101]-direction perpendicular to the surface (the lattice constants  $a$  and  $c$  are 8.529 and 5.211  $\text{\AA}$ ,

respectively). At this angle, the (083)-plane of the unit cell is parallel to the surface. Rotation around the [101] direction is random. This layer (layer I) has a thickness of approximately 7  $\mu\text{m}$ , as shown in Figure 9. The orientation within this layer should be caused by the nucleation kinetics since growth kinetics are unlikely to apply to the formation of an oriented nucleus surrounded by a homogeneous glass matrix or in contact to the surface. Possibly this orientation with respect to the surface is favorable in order to minimize the surface energy during nucleation.

As shown above, this layer is not seen in the XRD patterns. This can be explained as follows: the penetration depth of X-rays is much larger than that of electrons contributing to an EBSD pattern and hence in the case of XRD, the orientations of the crystals some micrometers below the surface contribute to the patterns, while in the case of EBSD the orientation more than 25 nm below the surface does not play any part. Since the volume fraction of the small crystals in layer I is much smaller than the volume fraction of the layer II, XRD measurements from the top,<sup>7–13,19</sup> which have a much greater information depth than EBSD, are likely to miss this topmost layer.

At a larger distance from the surface (layer II), the crystals are predominantly oriented with their crystallographic *c*-axes perpendicular to the surface. This means the crystals at a larger distance from the surface show a different orientation from those immediately at the surface. This orientation can be explained as follows: the initially formed crystals grow and then hinder each other. Since the crystallographic *c*-axis is the fastest growing axis in fresnoite under the conditions supplied,<sup>27</sup> those crystals oriented with their crystallographic *c*-axes perpendicular to the surface reach a greater depth faster, and can therefore continue to grow into the bulk of the sample. The crystals growing with the *c*-axis at an angle less than 90° to the surface are hindered in their growth by the other crystals. Thus, an oriented layer of crystals is formed. At an even larger distance from the surface, volume crystallization is observed. Of course, these crystals are randomly oriented.

This implicates that the orientation of the fresnoite crystals in layer II is caused by a kinetic selection.<sup>1</sup> While benitoite has been proposed to contribute to the orientation of fresnoite in the in the Ge-fresnoite system by Masai et al.,<sup>12</sup> no benitoite could be detected in the presented Ge-free sample. Benitoite could therefore not be the reason for the oriented fresnoite in the presented sample. A thermal gradient as described by Ochi et al. may enhance the oriented crystal growth; however, it is not absolutely necessary.<sup>19</sup>

The angle of orientation is rarely 90° to the surface but rather a slight deviation from 90° in different regions of the sample.

## 6. Conclusions

Thermal annealing of a glass with the composition  $\text{Ba}_2\text{Ti-Si}_{2.75}\text{O}_{9.5}$  at 810 °C for 20 h led to surface crystallization.

Immediately at the surface of the sample, a layer (layer I) of fresnoite crystals, oriented with their crystallographic [101]-direction perpendicular to the surface, is formed. This layer is approximately 7  $\mu\text{m}$  thick. It is assumed that the growth direction is due to nucleation kinetics. The *c*-axes rotate randomly around the [101]-direction.

The next layer (layer II) is approximately 50  $\mu\text{m}$  thick and the crystals are oriented with the crystallographic [001]-direction (*c*-axis) perpendicular to the surface of the sample. At this distance from the surface, crystals that are not oriented in the described manner are hindered by the oriented crystals, allowing only the latter to survive.

At a distance > 60  $\mu\text{m}$ , the orientation of the fresnoite crystals is random due to volume crystallization.

## References

- (1) Rüssel, C. *J. Non-Cryst. Solids* **1997**, *219*, 212–218.
- (2) Keding, R.; Rüssel, C. *J. Non-Cryst. Solids* **1997**, *219*, 136–141.
- (3) Keding, R.; Rüssel, C. *J. Non-Cryst. Solids* **2000**, *278*, 7–12.
- (4) Keding, R.; Rüssel, C. *J. Mater. Sci.* **2004**, *39*, 1433–1435.
- (5) Honma, T.; Ihara, R.; Benino, Y.; Sato, R.; Fujiwara, T.; Komatsu, T. *J. Non-Cryst. Solids* **2008**, *354*, 468–471.
- (6) Honma, T.; Komatsu, T.; Benino, Y. *J. Mater. Res.* **2008**, *23*, 885–888.
- (7) Halliyal, A.; Bhalla, A. S.; Newnham, R. E.; Cross, L. E. *J. Mater. Sci.* **1981**, *16*, 1023–1028.
- (8) Toyohara, N.; Benino, Y.; Fujiwara, T.; Komatsu, T. *Solid State Commun.* **2006**, *140*, 299–303.
- (9) Halliyal, A.; Bhalla, A. S.; Newnham, R. E.; Cross, L. E. *Ferroelectrics* **1981**, *38* (1981), 781–784.
- (10) Masai, H.; Fujiwara, T.; Benino, Y.; Komatsu, T. *J. Appl. Phys.* **2006**, *100*, 023526.
- (11) Masai, H.; Fujiwara, T. *J. Appl. Phys.* **2007**, *101*, 033530.
- (12) Masai, H.; Fujiwara, T.; Mori, H.; Benino, Y.; Komatsu, T. *J. Appl. Phys.* **2007**, *101*, 123505.
- (13) Takahashi, Y.; Benino, Y.; Fujiwara, T.; Komatsu, T. *J. Appl. Phys. Lett.* **2002**, *81*, 2.
- (14) Halliyal, A.; Safari, A.; Bhalla, A. S.; Newnham, R. E.; Cross, L. E. *J. Am. Ceram. Soc.* **1984**, *67*, 331–335.
- (15) Ting, R. Y.; Halliyal, A.; Bhalla, A. S. *J. Appl. Phys. Lett.* **1984**, *44*, 852–854.
- (16) Halliyal, A.; Bhalla, A. S.; Newnham, R. E.; Cross, L. E.; Gururaja, T. R. *J. Mater. Sci.* **1982**, *17*, 295–300.
- (17) Halliyal, A.; Bhalla, A. S.; Markgraf, S. A.; Cross, L. E.; Newnham, R. E. *Ferroelectrics* **1985**, *62*, 27–38.
- (18) Halliyal, A.; Bhalla, A. S.; Cross, L. E. *Ferroelectrics* **1985**, *62*, 3–9.
- (19) Ochi, Y.; Meguro, T.; Kakegawa, K. *J. Eur. Ceram. Soc.* **2006**, *26*, 627–630.
- (20) Völksch, G.; Harizanova, R.; Rüssel, C.; Mitsche, S.; Pölt, P. *Glastech. Ber. Glass. Sci. Technol.* **2004**, *77*, 438–441.
- (21) Völksch, G.; Wisniewski, W.; Rüssel, C. *J. Non-Cryst. Solids*, submitted.
- (22) Randle, V. *J. Mater. Sci.* **2009**, *44*, 4211–4218.
- (23) Schwartz, A. J.; Kumar, M.; Adams, B. L. In *Electron Backscatter Diffraction in Materials Science*; Kluwer Academic/Plenum Publishers: New York, 2000.
- (24) Baba-Kishi, K. *J. Mater. Sci.* **2002**, *37*, 1715–1746.
- (25) Keding, R.; Rüssel, C. *Ber. Bunsenges. Phys. Chem.* **1996**, *100*, 1515.
- (26) Höche, T.; Keding, R.; Rüssel, C. *J. Mater. Sci.* **1999**, *34*, 195–208.
- (27) Cabral, A. A.; Fokin, V. M.; Zanolto, E. D.; Chinaglia, C. R. *J. Non-Cryst. Solids* **2003**, *330*, 174–186.

## 3.2.

W. Wisniewski, M. Nagel, G. Völksch and C. Rüssel

**New Insights into the Microstructure of Oriented Fresnoite  
Dendrites in the System  $\text{Ba}_2\text{TiSi}_2\text{O}_8\text{-SiO}_2$  Through Electron  
Backscatter Diffraction (EBSD)**

Crystal Growth & Design, 2010, **10**, 1939-1945.

<http://pubs.acs.org/doi/abs/10.1021/cg1000304?prevSearch=%2528Wisniewski%2529%2BNOT%2B%255Batype%253A%2Bad%255D%2BNOT%2B%255Batype%253A%2Bacstoc%255D&searchHistoryKey=>

## New Insights into the Microstructure of Oriented Fresnoite Dendrites in the System $\text{Ba}_2\text{TiSi}_2\text{O}_8\text{--SiO}_2$ Through Electron Backscatter Diffraction (EBSD)

Wolfgang Wisniewski, Marcus Nagel, Günter Völksch, and Christian Rüssel\*

*Otto-Schott-Institut, Jena University, Fraunhoferstrasse 6, 07743 Jena, Germany*

*Received January 8, 2010; Revised Manuscript Received February 16, 2010*

**ABSTRACT:** A glass with the composition  $\text{Ba}_2\text{TiSi}_{2.75}\text{O}_{9.5}$  was crystallized by electrochemically induced nucleation. A *dc*-voltage (4.8 V) was attached between a platinum crucible containing the melt and a platinum wire inserted into the melt. The platinum wire was the cathode. After 2 min, crystals were formed at the cathode, which grew toward the crucible. These crystals consisted of fresnoite  $\text{Ba}_2\text{TiSi}_2\text{O}_8$ , were highly oriented, and showed dendritic growth. These structures were characterized in detail by using electron backscatter diffraction/orientation imaging microscopy. Only a few crystals deviate from the main orientation of the respective dendrite. They were located and quantified. Intermediate areas between dendrites were analyzed, and the true boundaries of areas with homogeneous orientation are presented. The orientation is not as pronounced in the first 600  $\mu\text{m}$  next to the platinum wire.

### 1. Introduction

Polar structures composed of fresnoite show interesting piezoelectric, pyroelectric, and surface acoustic wave properties.<sup>1,2</sup> Therefore, fresnoite is an interesting glass-ceramic material for piezoelectric and second harmonic generation applications.<sup>3–5</sup> Fresnoite also shows a nucleation rate of  $I = 1.4 \times 10^{16} \text{ m}^{-3} \text{ s}^{-1}$ , one of the largest nucleation rates reported for inorganic glasses.<sup>6</sup>

Randomly oriented polycrystalline fresnoite does not show macroscopic piezoelectric properties. Since fresnoite is not ferroelectric, an orientation of the permanent dipoles by applying an electric field is not possible. In order to utilize the piezoelectric properties of polycrystalline fresnoite, an orientation of the dipoles is therefore necessary. This can only be achieved by an oriented growth of the crystals. Three different routes for the preparation of oriented nonmetallic inorganic materials have been described in the literature.<sup>7</sup> One of these is the method of localized nucleation. Here, nucleation takes place only in a small part of the volume. Besides surface nucleation,<sup>8</sup> electrochemical nucleation was shown to enable the preparation of highly grain-oriented glass-ceramics. Electrochemically induced nucleation was first presented by Keding et al in 1996.<sup>9</sup> The effect of different glass compositions on the process has been described,<sup>10,11</sup> and the mechanism of the electrochemically induced crystallization has been especially discussed for the oriented growth of fresnoite from glasses in the  $2\text{BaO} \cdot \text{TiO}_2 \cdot 2.75\text{SiO}_2$  system.<sup>12</sup> This chemical composition is equivalent to stoichiometric fresnoite plus an excess of  $\text{SiO}_2$ .

It was reported that the polar axis (the crystallographic *c*-axis) is oriented parallel to the electric field and that large, rectangular crystalline structures are found in a plane perpendicular to the surface of the electrode. Höche et al.<sup>13</sup> found that grains in dendritic fresnoite are widely connected with each other and therefore are highly oriented. Kikuchi patterns

obtained in a transmission electron microscope showed that changes of crystal orientation within the respective dendrites are small and continuous but abrupt between neighboring dendrites.<sup>13</sup> A series of orientation imaging microscopy (OIM) scans presented by Völksch et al.<sup>14</sup> shows such an abrupt change between dendrites and a gradual change of orientation of  $12^\circ$  over a distance of about 3 mm within a single dendrite. Frequently, neighboring dendrites only deviate by a few degrees in their respective orientation perpendicular to the growth direction.<sup>13</sup> According to Höche et al.,<sup>13</sup> three subsequent steps of crystallization are responsible for the formation of the microstructure of fresnoite glass-ceramics.

This paper will present new results obtained by electron backscatter diffraction (EBSD)/OIM describing the orientation of crystalline phases found in glass-ceramics with the composition  $2\text{BaO} \cdot \text{TiO}_2 \cdot 2.75\text{SiO}_2$  produced by electrochemically induced nucleation.

### 2. Electron Backscatter Diffraction

EBSD became a standard method in mineralogy and metallography during the past 10 years. By contrast, only a few papers were published dealing with EBSD to characterize glass-ceramics.<sup>8,14,15</sup> A recent review on the applications of EBSD in materials science given by Randle<sup>16</sup> does not mention the investigation of glass-ceramics.

EBSD is based on the analysis of Kikuchi bands detected in diffraction patterns obtained from a crystalline sample. It is a powerful tool for the identification of certain crystal phases in the microstructure and for the local detection of crystal orientations. Using a scanning electron microscope (SEM) equipped with an EBSD-unit combines the ability of studying the morphology and crystallographic relationships of a crystalline solid simultaneously. The information depth of EBSD is around 10–50 nm<sup>17,18</sup> and hence much smaller than in the case of X-ray diffraction.

While a single EBSD-pattern provides information on the crystal from the volume where it was generated, a grid of

\*Corresponding author. Address: Fraunhoferstr. 6, 07743 Jena Otto-Schott-Institut, Jena University, Germany. Tel: (0049) 03641 948501. Fax: (0049) 03641 948502. E-mail: ccr@uni-jena.de.

EBSD-patterns allows the description of the crystallographic properties of a microstructure in the scanned area and is referred to as orientation imaging microscopy (OIM). The latter describes scanning a surface in a defined step size, collecting and indexing EBSD-patterns so that each point in an OIM-map represents the information of an indexed EBSD-pattern. Indexing a diffraction pattern is achieved by a "voting" system (see paper by Schwartz et al.<sup>17</sup>).

The orientation of a crystal is usually defined by the three Euler angles  $\varphi_1$ ,  $\Phi$ , and  $\varphi_2$ . Other useful parameters describing an indexed pattern in the used software package are the image quality value (IQ) and the confidence index (CI).

The IQ-value of an EBSD-pattern is affected by numerous parameters; however, the main input from the sample is the perfection of the crystal lattice<sup>17</sup> in the top 10–50 nm (penetration depth). Since glass has no lattice to produce a diffraction pattern, points in an IQ map obtained from glass are attributed to very low IQ-values, making the IQ-value a very good filter to distinguish between amorphous and crystalline phases. The gray scale map of the IQ-value can be used to increase the contrast in a color map describing orientations. If points of a map are not attributed to the defined orientation but show a high IQ-value, they therefore appear white. A relatively low IQ-value can also be the result of tensions, defects within the crystal lattice, or a very thin layer of glass covering a crystal.

The CI is a value calculated from the "votes" obtained from different orientation solutions for a phase used to index a pattern.<sup>17</sup> While patterns obtained from an fcc-material were indexed, it was found that a solution was correct in 95% of the cases when the CI was 0.1 or greater and at least six Kikuchi bands were detected.

In the orientation map of an OIM-scan, selected triples of Euler angles as well as corresponding tolerances are defined to describe specific orientations. A wire frame of the unit cell of fresnoite is shown in Figure 1 as a convenient method to visualize an orientation. Here, three different orientations of the tetragonal unit cell and their respective Euler angle combinations are shown. In Figure 1, the triple (0;0;0) describes a fresnoite crystal with the *c*-axis perpendicular to the surface of the sample. The  $\Phi$ -value of 90° means the *c*-axis is parallel to the sample surface. The third wire frame describes an arbitrary orientation.

An inverse pole figure (IPF) is a reduction of the pole figure by symmetric operations to a unit triangle containing all orientations or their symmetric equivalents. It is therefore a useful plot for an overview of all appearing orientations in a scan covering crystals showing varying orientations.

### 3. Experimental Procedures

A glass with the batch composition  $\text{Ba}_2\text{TiSi}_{2.75}\text{O}_{9.5}$  (or  $2\text{BaO} \cdot \text{TiO}_2 \cdot 2.75\text{SiO}_2$ ) was prepared from the raw materials  $\text{BaCO}_3$ ,  $\text{TiO}_2$ , and  $\text{SiO}_2$  (quartz). After mixing, the compounds were melted in a platinum crucible (250 mL) at 1450 °C using an inductively heated furnace. The furnace was equipped with a motor, which was able to lift a platinum wire (diameter 0.4 mm) in and out of the melt. After 2 h of soaking at 1500 °C, the platinum wire was lowered and inserted into the melt. Then the melt was cooled down to 1300 °C and soaked for another 30 min. Within that period of time, spontaneous crystallization was not observed. To induce the nucleation, a voltage of 4.8 V was applied between the wire (cathode) and the crucible (anode) using a d.c. calibrator (Knick, Germany). This resulted in a current of 100 mA. After 2 min, crystallization was observed, starting at the cathode and growing radially toward the anode. After another 4 min, the platinum with the adjacent cylindrical glass-ceramic body was

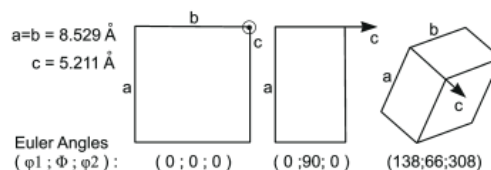


**Figure 1.** Wire frames of the unit cell of fresnoite visualizing the orientations described by the respective combination of Euler angles.

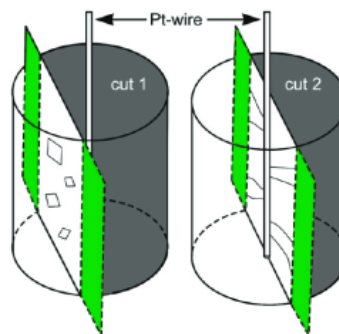


**Figure 2.** Cut planes 1 and 2 of the fresnoite block.

lifted out of the melt and cooled down to room temperature, applying a rate of 3 K/min. To stabilize the body for cutting, it was embedded in Araldite CY 212, a polymer adequate for vacuum application.

The samples were manually polished with shrinking grain sizes down to 0.75  $\mu\text{m}$  diamond suspension. To obtain acceptable EBSD-patterns, a final finish of 30 min using colloidal silica was applied. Conductivity of the surface was achieved by mounting the samples using Ag-paste and applying a thin coating of carbon at about  $10^{-3}$  Pa.

The samples were studied using a Jeol JSM-7001F FEG-SEM equipped with a TSL Digiview 1913 EBSD-camera. OIM-scans were captured and evaluated using the programs TSL OIM Data Collection 5.31 and TSL OIM Analysis 5. The OIM-scans were performed using a voltage of 20 kV and a current of about 2.40 nA. All OIM-maps presented are a combination of a gray scale IQ-map and a map describing various orientations by different colors.

### 4. Results

In a block of fresnoite grown by electrochemically induced nucleation, two cuts parallel to the Pt-wire were performed (see Figure 2). A first cut was carried out to illustrate the microstructure at a distance of about 4 mm from the wire (cut 1 in Figure 2). This sample contained a number of rectangular dendritic areas, including a dendrite cut perpendicular to the direction of growth and outlined by the black frame presented in Figure 3. The white frames superimposed on the SEM-image in Figure 3 depict areas analyzed by OIM-scans. The dendrite is in direct contact to a number of neighboring dendrites at the left and at the top of Figure 3. Cut 2 (see Figure 2) contained a part of the Pt-wire, enabling a side view of the grown crystal structures. A dendrite cut almost parallel to the direction of growth was found in this sample and is presented in Figure 4. In the SEM-images, pores in the glass-ceramic appear black if filled with polymer or white if empty. In the presented OIM-scans pores are always black due to the low IQ-values attributed to these areas.

Although the orientation within the dendrites was extremely homogeneous, a small number of crystals deviating from

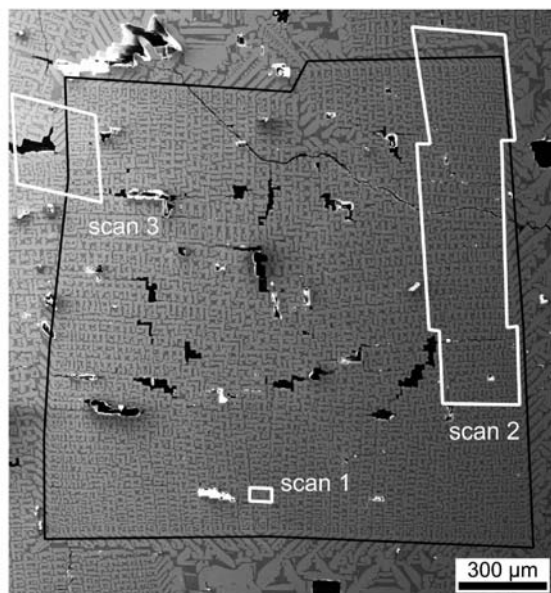


**Figure 3.** SEM-image of a fresnoite dendrite (outlined in black) cut perpendicular to the direction of growth with white frames marking performed OIM-scans superimposed on the surface.

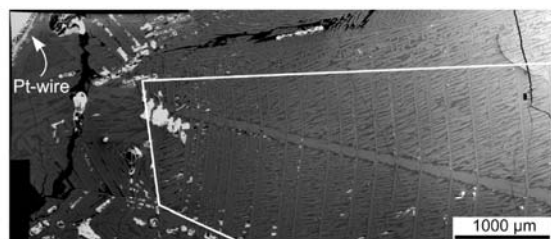


**Figure 4.** SEM-image of a fresnoite dendrite cut parallel to the direction of growth and outlined by the white frame.

the main orientation of the dendrite were found. Scan 1 in Figure 3 was performed on such a deviating crystal and the resulting orientation map is presented in Figure 5. Representative EBSD patterns obtained from the crystals showing two different orientations (a and b) are presented in Figure 5. Simulated wire frames of the unit cell describe the orientations with respect to the surface of the sample. The deviating crystal (see right EBSD pattern) is tilted by  $22^\circ$  and slightly rotated with respect to the main orientation of the dendrite. Since EBSD is very sensitive to surface defects, scratches at the surface can clearly be seen in the OIM-map. The crystals are in unusually close contact to each other at the right side of the deviating crystal.

To quantify the occurrence of deviating crystals, the area of scan 2 outlined in Figure 3 was analyzed by OIM. Figure 6 shows a combination of the grayscale IQ-map and colored orientation map of the merger of the scans performed with a step size of  $1.5\ \mu\text{m}$ . The orientation of most crystals seen in the OIM-map are in agreement within a total deviation of the Euler angles ( $\varphi_1$ ,  $\Phi$ ,  $\varphi_2$ ) of  $\pm 5^\circ$  (orange). Crystals not attributed to the defined orientation appear white due to their high IQ-values. Only a few crystals (altogether 29 crystals) are observed whose orientations deviate to a larger extent from that of the dendrite in the scanned area. From these

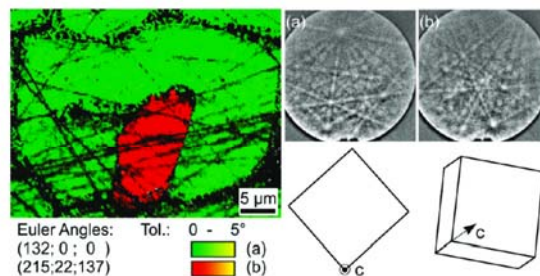


**Figure 5.** Orientation map showing a deviating crystal and representative EBSD patterns from each orientation. Orientations are described by Euler angles and wire frames of fresnoite unit cells in the respective orientations.



**Figure 6.** Deviating crystals (white) in a merger of OIM-scans within a dendrite of fresnoite cut perpendicular to the  $c$ -axis. The main orientation is marked orange.

29 crystals, 16 (55%) crystals show deviations of  $5^\circ < \Phi \leq 10^\circ$ , implying mainly rotations around the  $c$ -axis, and 6 (20%) crystals show a deviation of  $\Phi \geq 20^\circ$ , the largest deviation in  $\Phi$  being  $43^\circ$ . A histogram showing the number of deviating crystals as a function of the deviation in  $\Phi$  in comparison to the dendrite is given in Figure 7. Altogether, only 2.3% of the points depicted in the scan are attributed to crystals whose orientations deviate from that of the dendrite.

Figure 8 presents an image (cut 2 in Figure 2) in which the platinum wire is seen. The image shows a number of dendrites, one of which was cut almost parallel to the direction of

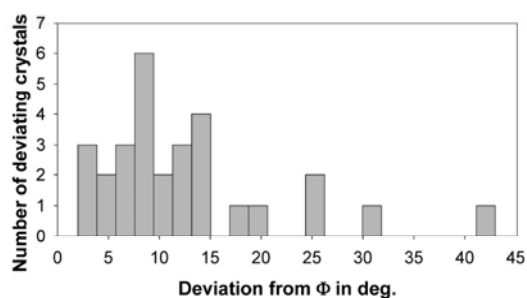


**Figure 7.** Histogram of the occurrence of deviating crystals against the degree of deviation with respect to the Euler angle  $\Phi$ .

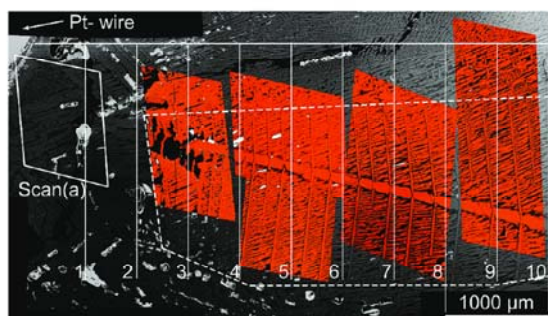


**Figure 8.** Deviating crystals marked white in a series of OIM-scans within dendrite 1 of fresnoite cut parallel to the  $c$ -axis. The main orientation is marked orange.

growth. The Pt-wire is shown in the upper left corner of Figure 8. A dendritic structure is not seen at the immediate surface of the electrode. At a distance of about 1.5 mm from the Pt wire, the dendritic structure begins to appear. Crystals deviating from the main orientation (presented in orange) are once again presented in white. Crystals outside the dotted line describing the assumed boundaries of the dendrite were not considered. Within these boundaries, the size of the scanned area and the size of the dendrite were roughly estimated. The number of deviating crystals in each section (sections 1–10) was counted and shown in Figure 9 as the number of crystals per  $\text{mm}^2$ . Relevant values for the estimation of these values are given in Table 1. Each of the sections has a width of  $500 \mu\text{m}$ . Crystals appearing in two sections were attributed to the section closer to the wire. Only crystals whose  $\Phi$ -angles deviate more than  $5^\circ$  from the main orientation were considered. As shown in Figure 9, the number of deviating crystals decreases with the distance from the Pt-wire. By analogy, the black columns in Figure 9 (dendrite 2) present the results of a second, smaller dendrite analyzed in the same fashion. A decrease in the number of deviating crystals with the distance from the platinum wire is seen here as well.

Near the Pt-wire, the structure is not oriented and the distribution is more diverse as shown by the IPF-map presented in Figure 10 (scan (a) outlined in Figure 8). The map presented in Figure 10 contains only points of the phases fresnoite and platinum with a CI of at least 0.1. The platinum (circled white) in the upper left corner of the scan is randomly oriented. The wire frames 1–6 attributed to the main orientations of fresnoite are displayed in Figure 10.

Concerning the regions 1–3, in which the fresnoite crystals are in immediate contact with Pt, the  $c$ -axes are nearly parallel to the Pt-wire. The wire frames 4–6, attributed to fresnoite

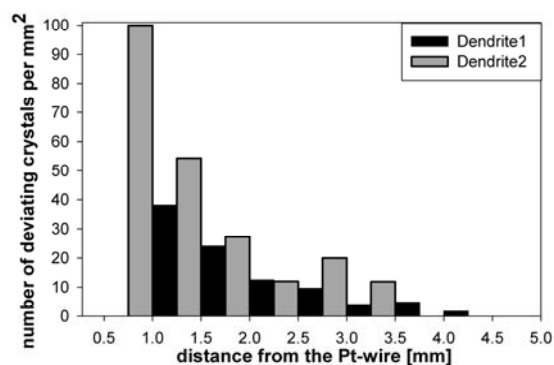


**Figure 9.** Number of deviating crystals per  $\text{mm}^2$  in reference to the distance from the Pt-wire observed in two dendrites of fresnoite.

crystals at a larger distance from the platinum wire, show  $c$ -axes fairly perpendicular to the platinum wire. While the frames 4 and 5 show a  $c$ -axis approximately parallel to the present surface of the sample, frame 6 shows a  $c$ -axis perpendicular to the present surface.

The Pt-wire itself appears to be partially dissolved. In the underlying SEM-image in Figure 11, a spongy area (a) surrounding the clearly corroded Pt-wire (b) is observed. While high quality EBSD-patterns were obtained from the spongy area, the OIM-analysis of the main wire was not possible due to the lack of acceptable EBSD-patterns. The crystals in the spongy area are randomly oriented.

Scan 3 in Figure 3 covers an area where three dendrites are in direct contact. In the orientation map of this scan (allowing a tolerance of only  $5^\circ$ ), superimposed on an SEM-image of the surrounding area in Figure 12, the homogeneous orientation of crystals within their respective domains can be seen. The  $c$ -axis of dendrite (b), the main dendrite depicted in Figure 3, is perfectly perpendicular to the surface, as shown by the  $\Phi$ -value of 0. The  $\Phi$ -values of the neighbors (a) and (c) given in Figure 12 are attributed to tilts of  $29^\circ$  and  $17^\circ$  to the surface of the sample, respectively. The crystals at the immediate border of the dendrite show an elongation outward under an angle of  $45^\circ$ . This means growth in the [100] or [010] direction is preferred at the side of the dendrite if space is available. At the upper end of the scan, a small crystal deviates from the main orientation and is not captured by the applied combination of Euler angles. It therefore appears white in the underlying IQ-map (see arrow).

Figure 13 presents an orientation map superimposed on an SEM-image. It shows the orientation of two rectangular areas (a) and (b) extending into the surrounding area. While the crystals in the intermediate zones do not show the geometric patterns of the respective crystals within the rectangular areas, their crystallographic orientations are in agreement with those of the respective dendrites. It should be noted that, also in Figure 13, crystals (1) and (2) with deviating orientations can be found in the zones between rectangular areas.

## 5. Discussion

According to the literature,<sup>1,2</sup> oriented fresnoite was first prepared by surface crystallization. EBSD-analysis of oriented fresnoite prepared by surface crystallization showed that at some distance from the surface ( $\sim 10 \mu\text{m}$ ) the crystallographic  $c$ -axis is oriented perpendicular to the surface.<sup>8</sup> By using the method of electrochemically induced nucleation,



Table 1. Relevant Values for the Histogram Presented in Figure 9

distance from Pt-wire [mm]:	1	1.5	2	2.5	3	3.5	4	4.5	5
Dendrite 1									
number of deviating crystals		12	12	10	7	3	4	1	0
number of deviating crystals/mm <sup>2</sup>		38.1	24.0	12.5	9.6	4.0	4.8	1.7	0.0
area scanned [mm <sup>2</sup> ]		0.32	0.50	0.80	0.73	0.75	0.83	0.60	0.75
% of dendrite scanned per area		69.2	66.7	94.1	85.9	85.7	94.3	66.7	83.3
Dendrite 2									
number of deviating crystals	10	11	6	3	7	4			
number of deviating crystals/mm <sup>2</sup>	100	54.3	27.2	12.0	20.0	11.9			
area scanned [mm <sup>2</sup> ]	0.10	0.20	0.22	0.50	0.35	0.34			
% of dendrite scanned per area	100	81.0	98.0	100.0	100.0	90.0			

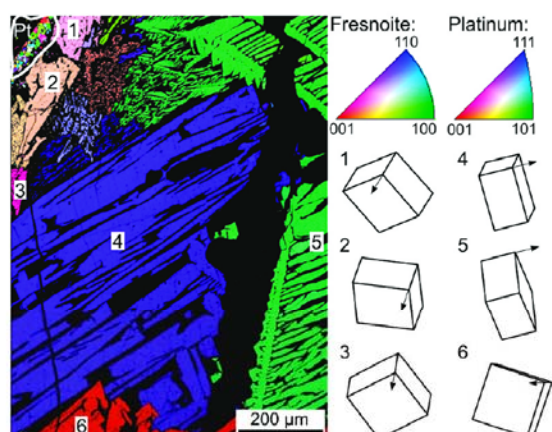


Figure 10. IPF-map of scan (a) outlined in Figure 8. The phase Pt is framed by a white line. Wire frames visualizing the orientations 1–6 of fresnoite are sketched.

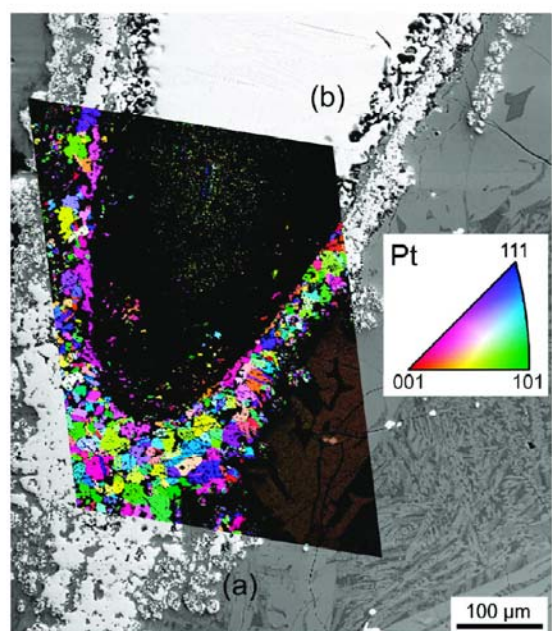


Figure 11. IPF-map of an OIM-scan performed on the Pt-wire overlaying an SEM-image of the surrounding area (a: spongy area, b: main wire).

very large, rectangular areas of highly oriented fresnoite were formed in which orientation was observed with respect to all

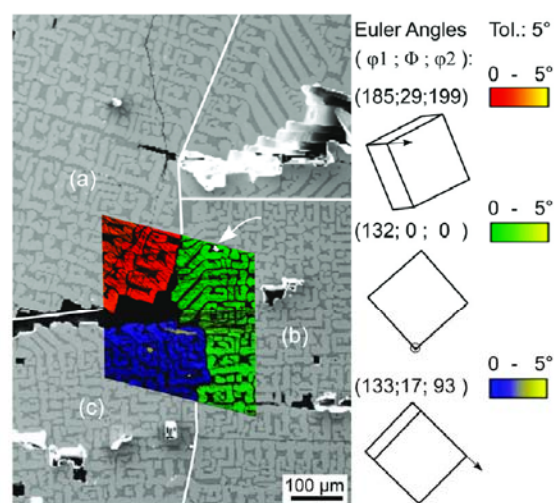


Figure 12. Orientation map of an OIM-scan performed over three dendrites superimposed on an SEM-image of the surrounding area. Orientations are described by Euler angles and wire frames of fresnoite unit cells in the respective orientations.

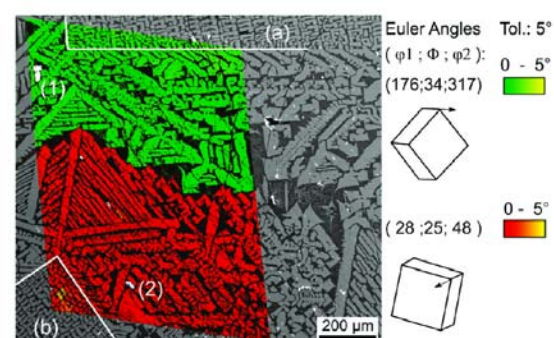


Figure 13. Orientation map of an OIM-scan covering the intermediate area between two dendrites (a) and (b). Crystals (1) and (2) deviate from the respective main orientation and therefore appear white.

crystallographic axes of the crystal. The primary direction of growth within these areas was found to be the crystallographic [001]-direction. This is in compliance with previously published results.<sup>9,13</sup> During crystallization, the chemical composition of the glass phase is changed, leading to a higher SiO<sub>2</sub> concentration in the residual glass phase. This glass phase remains in between the dendrites. A higher SiO<sub>2</sub>-content

increases the viscosity of the glass and therefore constrains the crystallization process.

The structure of crystals presented in Figure 4 implies the growth of the rectangular areas to be dendritic. Primary growth occurs parallel to the [001] direction (*c*-axis). The crystal growth velocity along the other major axes, that is, the [100] and [010] directions (*a*- and *b*-axes), is smaller. This is in agreement to growth rates published by Cabral et al.<sup>6</sup> In the present study, growth in the directions [100] and [010] is directly observed at the edges of the rectangular areas. These edges are usually formed parallel to the (110)-planes of the crystals they are composed of.

Homogeneously oriented dendrites of fresnoite do not start to grow directly from the surface of the Pt-wire. The orientation of fresnoite near the Pt-wire is diversely distributed.

The Pt-wire is corroded during the process. This can be explained by the cathodic reduction of  $\text{Si}^{4+}$  to elemental silicon during initial current flow. The elemental silicon forms an alloy with Pt<sup>19</sup> which lowers the melting point down to an eutecticum at 830 °C. Since the sample was crystallized at 1300 °C, at least 16 at % Si would be necessary to form a liquid Pt–Si-alloy.<sup>20</sup> Platinum has been shown to react with  $\text{SiO}_2$  leading to a  $\text{Pt}_3\text{Si}$ -phase at 570 °C under reducing atmosphere.<sup>21</sup> A Si-containing, spongy Pt-phase around the platinum wire should solidify upon cooling to room temperature to a significantly harder phase containing minor quantities of  $\text{Pt}_3\text{Si}$ . The difference in hardness of the Pt-phases would explain the extremely different results obtained by the applied polishing procedure: while the main wire is very soft and therefore susceptible to a high input of dislocations during polishing, the harder phase in the spongy area would not be affected in the same way. Thus EBSD-patterns could be obtained from the harder phase, while a high density of dislocations would prohibit the formation of EBSD-patterns in the soft wire.

The mechanism of the chemomechanical polish by colloidal silica is still not well understood and likely to be different for varying materials to the chemical component. A model describing the mechanism of removal for silicon has been published.<sup>22</sup> In the presented samples it is likely that the layer of crystal defects (dislocation etc.) introduced during the rougher steps of sample preparation is thicker in the area of the softer Pt-wire than in the harder Pt-phase (spongy) and fresnoite. Because the removal of material is minimal during the final step of the polishing process, this layer was probably fully removed from the harder phases and not from the softer phase, where it is thicker.

The corrosion of Pt only occurs if a voltage is applied to the system. Without the voltage, the Pt-wire does not induce nucleation during soaking for 30 min at 1300 °C. A nucleation caused by the liquid Pt–Si-alloy would therefore seem unlikely.

The deviating crystals found within the dendrites cannot be due to Pt drifting or diffusing through the melt for a number of reasons. First, Pt was never found at any relevant distance from the wire. If it were connected to the crystal deviation, it should be found in the vicinity of the deviating crystals. Pt could not be transported away by the crystallization front because the deviating, secondary arms are clearly formed after the primary arms which would trap the Pt.

Furthermore, if Pt were corroded and then drift through the viscose melt, this drift would have to be very fast, because the entire crystallization process is completed in only 6 min. It would also seem very unlikely that only very few particles

of Pt would drift through the melt, while the majority are confined to the spongy area around the wire.

The rectangular dendrites found in cuts perpendicular to the *c*-axes of the crystals are in some cases in direct contact with each other. While the orientation of a dendrite usually differs from that of a neighboring dendrite, the orientation within the dendritic regions is very homogeneous. The crystal orientation is not limited to the dendritic regions identified in the micrographs, if there is no direct contact between them. The true limit of the respective areas of crystal orientation cannot be reliably detected by SEM or optical microscopy, making EBSD/OIM a suitable method for describing these borders of orientation. Probably, the dendrites act as seed crystals for the crystallization of the volume between them. This would explain the occurrence of homogeneous orientations also in those regions which show a morphology different from that of the rectangular structures. This would be significant in order to achieve highly oriented, macroscopic samples of fresnoite.

Within the highly oriented dendrites, crystals deviating from the main orientation of the dendrite are found. The difference in the EBSD-patterns obtained from the different crystals presented in Figure 5 proves the deviation without any doubt. Deviating crystals in the dendrites, although only representing a small percentage of the number of crystals present, are not an extremely rare anomaly. The number of deviating crystals decreases with increasing distance from the Pt-wire.

Up to now, deviating crystals in direct contact with the main branch of a dendrite have not been found. This is no proof of the detachment of deviating crystals from the main body because of the relatively thin root of the crystals in comparison to their total size. However, the detachment of crystals from the main tree would be an obvious explanation for deviation. A detached crystal would be able to rotate and even tilt slowly in the viscous matrix depending on the space available considering its neighbors. The unusually close contact between the deviating crystal and its neighbor in Figure 5 could be the result of this process. Thus, it is not clear that all grains in a fresnoite dendrite are connected.<sup>13</sup>

If the deviation in the crystal orientation were caused by stacking faults, the deviation in the  $\Phi$ -values should possess discrete values and not deviations mainly in the range from 3 to 15° as shown in Figure 7, which clearly shows the degree of deviation to be fairly statistical.

As shown in Figure 9, the number of deviating crystals decreases with the growing distance from the electrode. Possibly this is due to the longer time available to achieve detachment in the region near the electrode, because here the dendrites are formed first. At a larger distance from the electrode, the time between the formation of the crystal and it being drawn from the melt is much shorter.

Since the growth of the rectangular areas is dendritic, the detachment of crystals is probably the result of dendrite fragmentation, a process mainly studied on metals and recently reviewed by Rettenmayr.<sup>23</sup>

## 6. Conclusions

Electrochemically induced nucleation leads to dendritic growth of fresnoite. The primary direction of growth in a dendrite is the [001]-direction. The rectangular shape of the dendrite corresponds to the (110)-planes of the fresnoite crystals. Within one dendrite, most crystals have the same

orientation (total deviation in the Euler angles  $\varphi_1, \Phi, \varphi_2 \leq 5^\circ$ ). Deviating crystals are found within the dendrites, probably due to dendrite fragmentation. The number of deviating crystals decreases with the increasing distance from the platinum electrode. The rectangular shape of the dendrites is not the limit of the respective crystal orientation. The Pt-wire is corroded during the process due to the reduction of  $\text{SiO}_2$  to elemental silicon and subsequent alloying with platinum. The orientation of the fresnoite crystals near the Pt-wire is diverse.

**Acknowledgment.** The authors acknowledge M. Rettenmayr et al. (Jena) for creative discussions on dendritic fragmentation and Pt-corrosion and G. Möller (Jena) for the polishing of the samples.

### References

- (1) Halliyal, A.; Safari, A.; Bhalla, A. S.; Newnham, R. E.; Cross, L. E. *J. Am. Ceram. Soc.* **1984**, *67*, 331–335.
- (2) Ting, R. Y.; Halliyal, A.; Bhalla, A. S. *Appl. Phys. Lett.* **1984**, *44*, 852–854.
- (3) Halliyal, A.; Bhalla, A. S.; Newnham, R. E.; Cross, L. E.; Gururaja, T. R. *J. Mater. Sci.* **1982**, *17*, 295–300.
- (4) Halliyal, A.; Bhalla, A. S.; Markgraf, S. A.; Cross, L. E.; Newnham, R. E. *Ferroelectrics* **1985**, *62*, 27–38.
- (5) Halliyal, A.; Bhalla, A. S.; Cross, L. E. *Ferroelectrics* **1985**, *62*, 3–9.
- (6) Cabral, A. A.; Fokin, V. M.; Zanotto, E. D.; Chinaglia, C. R. *J. Non-Cryst. Solids* **2003**, *330*, 174–186.
- (7) Rüssel, C. *J. Non-Cryst. Solids* **1997**, *219*, 212–218.
- (8) Wisniewski, W.; Nagel, M.; Völksch, G.; Rüssel, C. *Cryst. Growth Des.*, DOI: 10.1021/cg901407d.
- (9) Keding, R.; Rüssel, C. *Ber. Bunsenges. Phys. Chem.* **1996**, *100*, 1515.
- (10) Keding, R.; Rüssel, C. *J. Non-Cryst. Solids* **1997**, *219*, 136–141.
- (11) Keding, R.; Rüssel, C. *J. Non-Cryst. Solids* **2000**, *278*, 7–12.
- (12) Keding, R.; Rüssel, C. *J. Non-Cryst. Solids* **2005**, *351*, 1441–1446.
- (13) Höche, T.; Keding, R.; Rüssel, C. *J. Mater. Sci.* **1999**, *34*, 195–208.
- (14) Völksch, G.; Wisniewski, W.; Rüssel, C. *J. Non-Cryst. Solids*, submitted.
- (15) Völksch, G.; Harizanova, R.; Rüssel, C.; Mitsche, S.; Pöhl, P. *Glastech. Ber. Glass. Sci. Technol.* **2004**, *77*, 438–441.
- (16) Randle, V. *J. Mater. Sci.* **2009**, *44*, 4211–4218.
- (17) Schwartz, A. J.; Kumar, M.; Adams, B. L. In *Electron Backscatter Diffraction in Materials Science*; Kluwer Academic/Plenum Publishers: New York, 2000.
- (18) Baba-Kish, K. *Z. J. Mater. Sci.* **2002**, *37*, 1715–1746.
- (19) Wang, D.; Penner, S.; Su, D. S.; Rupprechter, G.; Hayek, K.; Schlögl, R. *J. Catal.* **2003**, *219*, 434–441.
- (20) Massaraa, R.; Feschotte, P. *J. Alloys Compd.* **1993**, *201*, 223–227.
- (21) Lamber, R.; Jaeger, N. I. *J. Appl. Phys.* **1991**, *70*, 457–461.
- (22) Pletsch, G. J.; Higashi, G. S.; Chabal, Y. J. *Appl. Phys. Lett.* **1994**, *64*, 3115–3117.
- (23) Rettenmayr, M. *Int. Mater. Rev.* **2009**, *54*, 1–17.

### 3.3.

W. Wisniewski, M. Nagel, G. Völksch and C. Rüssel

#### **Irregular Fourfold Hierarchy in Fresnoite Dendrites Grown via Electrochemically Induced Nucleation of a $\text{Ba}_2\text{TiSi}_{2.75}\text{O}_{9.5}$ Glass**

Crystal Growth & Design, 2010, **10**, 4526-4530.

<http://pubs.acs.org/doi/abs/10.1021/cg1008158?prevSearch=%2528Wisniewski%2529%2BNOT%2B%255Batype%253A%2Bac%255D%2BNOT%2B%255Batype%253A%2Bac%255D&searchHistoryKey=>

**Irregular Fourfold Hierarchy in Fresnoite Dendrites Grown via Electrochemically Induced Nucleation of a  $\text{Ba}_2\text{TiSi}_{2.75}\text{O}_{9.5}$  Glass**

Wolfgang Wisniewski,\* Marcus Nagel, Günter Völksch, and Christian Rüssel

*Otto-Schott-Institut, Jena University, Fraunhoferstrasse 6, 07743 Jena**Received June 18, 2010; Revised Manuscript Received August 31, 2010*

**ABSTRACT:** Dendritic growth of fresnoite, a barium titanium silicate, is achieved at 1200 °C from a glass with the composition  $\text{Ba}_2\text{TiSi}_{2.75}\text{O}_{9.5}$  using electrochemically induced nucleation. The highly oriented main trunk is formed with primary and secondary branches which obey this rule. In between the branches, a fourth hierarchy is built with fine, irregular honeycomb and lamellar structures. A glassy phase occurs between these structures. The crystal orientation is the same in the crystals following the main crystallographic axes as well as the irregular structures. This was proven by determining crystal orientations via electron backscatter diffraction (EBSD). The crystallization of fresnoite at high temperatures was triggered by attaching a dc-potential of a few volts between a platinum crucible containing the melt and a platinum wire inserted into the melt. After a short time crystals were formed at the cathode and grew toward the crucible in the direction of the crystallographic *c*-axis.

**1. Introduction**

Dendritic crystal growth is frequently observed during solidification of metal or polymer melts. Typically dendrites are formed with branches growing along the main crystallographic directions,<sup>1–4</sup> but atypical growth directions have also been observed.<sup>1</sup> Dendritic crystal growth was subject to numerous experimental, theoretical, and computational studies in the past few years.<sup>1,3,5–8</sup> The structures are reported to result from a morphological instability of the solid liquid interface.<sup>2,4,9–11</sup>

In oxidic glass forming melts, dendritic growth is not as often observed, mainly because nucleation requires high thermodynamic driving forces during cooling, i.e. high undercooling.<sup>12,13</sup> Those temperatures are notably below the maximum crystal growth velocity, and crystal growth is mainly governed by limited diffusion and high viscosity.<sup>12,14</sup> Hence, dendrites in crystallized glasses usually possess sizes of only some ten micrometers. By contrast, the so-called electrochemically induced nucleation<sup>15–29</sup> allows initiation of nucleation in glass forming liquids at temperatures only some 10 K below the liquidus temperature. Here, a dc-potential of a few volts is attached between a platinum crucible containing the melt and a platinum wire inserted into it. After a short time, crystals are formed near the cathode and grow away from the electrode. This is usually combined with high crystal growth velocities and the formation of large dendrites whose size may even exceed some centimeters.<sup>20</sup>

Fresnoite,  $\text{Ba}_2\text{TiSi}_2\text{O}_8$ , occurs as a natural mineral<sup>21</sup> and is a polar crystal.<sup>22</sup> It is a material with interesting properties, such as piezoelectric, pyroelectric, and second harmonic generation.<sup>23–27</sup> Fresnoite is not ferroelectric, and hence, an orientation of the permanent dipoles by an electric field is not possible. To be suitable as a piezoelectric material, an orientation of the crystalline structures must therefore be achieved during the preparation. While controlling and/or suppressing dendritic growth is usually the main interest when metallic materials are prepared,<sup>3</sup> oriented crystal growth is quite essential in

the case of piezoelectric materials.<sup>20</sup> Dendrites have also been found useful for controlling shear banding in nanocrystalline alloys.<sup>28,29</sup>

Routes for the preparation of oriented materials which are suitable to achieve polarity are mainly based on localized nucleation,<sup>30</sup> where nucleation takes place only in a small part of the volume. Among these methods, besides surface nucleation,<sup>31–33</sup> electrochemical nucleation was shown to enable the preparation of highly grain-oriented glass-ceramics.<sup>15,19,20,34–37</sup>

Electrochemically induced nucleation was first described in 1996.<sup>19</sup> The mechanism of the electrochemically induced crystallization in the  $2\text{BaO} \cdot \text{TiO}_2 \cdot 2.75\text{SiO}_2$ -system has been described as an electrochemical effect.<sup>34</sup> The first step is the reduction of the glass ( $\text{Ti}^{4+} \rightarrow \text{Ti}^{3+}$ ), which leads to a decrease in viscosity and network connectivity and finally results in a steep increase of the nucleation rate.<sup>35,36</sup> Once nucleation is achieved, the crystals grow very fast.<sup>38</sup> The growth of the crystals achieved by this method has been described as dendritic.<sup>20,37</sup> While the orientation of the crystalline phase within a dendrite is very homogeneous,<sup>20,37</sup> a small number of crystals (~1.2%) was found to deviate from the main orientation,<sup>20</sup> probably due to dendritic fragmentation.<sup>8</sup>

In between the dendritic crystals, small, lamellar structures with sizes up to a few micrometers are found.<sup>37</sup> The orientation of the structures in between the dendritic crystals as well as their origin has not been reported until now. T. Höche studied the boundary between the dendritic and lamellar fresnoite and showed the lattice planes of the dendrite extending into the lamellae.<sup>37</sup> It was proposed that the lamellar growth is initiated by protuberances in the growth front of fresnoite after it reaches the eutectic composition.<sup>37</sup>

Glass with the composition of stoichiometric fresnoite shows one of the largest nucleation rates reported for inorganic glasses.<sup>38</sup> After adding an excess of  $\text{SiO}_2$ , however, a glass with the composition  $\text{Ba}_2\text{TiSi}_{2.75}\text{O}_{9.5}$  does not spontaneously nucleate and crystallize at 1200 °C without triggering the nucleation by supplying an electric current.<sup>35,36</sup>

This paper provides a study of fresnoite grown via electrochemically induced nucleation performed by scanning electron

\*Corresponding author. Telephone: (0049) 03641 948515. Fax: (0049) 03641 948502. E-mail: wolfgang.w@uni-jena.de.

microscopy using electron backscatter diffraction (EBSD)<sup>39,40</sup> and orientation imaging microscopy (OIM). Special attention has been paid to the regions in between the dendritic crystals. Results are illustrated by using orientation maps of OIM-scans.

## 2. Experimental Procedure

The compounds BaCO<sub>3</sub>, TiO<sub>2</sub>, and SiO<sub>2</sub> (quartz) were mixed and subsequently melted in a platinum crucible (250 mL) at 1450 °C using an inductively heated furnace to produce a glass with the composition Ba<sub>2</sub>TiSi<sub>2.75</sub>O<sub>9.5</sub>. The furnace was equipped with a lifting motor, which enabled lifting of a platinum wire in and out of the melt. After 2 h of soaking at 1500 °C, the platinum wire was inserted centrally into the melt. The melt was then cooled down to 1200 °C. During soaking for another 30 min, spontaneous crystallization was not observed. To induce nucleation, a voltage (4.8 V) between the Pt wire (cathode) and the crucible (anode) was applied, using a dc calibrator (Knick, Germany). This led to a current flow of 100 mA. After 2 min, crystallization was observed, starting at the cathode and growing radially toward the anode. After another 4 min, the platinum wire with the adjacent crystals was lifted out of the melt and cooled down to room temperature, supplying a cooling rate of 3 K/min.

The samples were manually polished with shrinking grain sizes down to a 0.75 μm diamond suspension. A final finish of 30 min using colloidal silica was applied. Conductivity of the surface was achieved by mounting the sample using Ag-paste and applying a thin coating of carbon at about 10<sup>-3</sup> Pa.

The samples were characterized using a scanning electron microscope Jeol JSM-7001F FEG-SEM equipped with a TSL Digiview 1913 EBSD-camera. OIM-scans were captured and evaluated using the programs TSL OIM Data Collection 5.31 and TSL OIM Analysis 5. The OIM-scans were performed using a voltage of 20 kV and a current of about 2.40 nA. All OIM-maps presented are a combination of a gray scale image quality-map (IQ-map) and an orientation map describing various orientations by different colors. Only points with a minimum confidence index (CI) of 0.1 were considered in the maps.

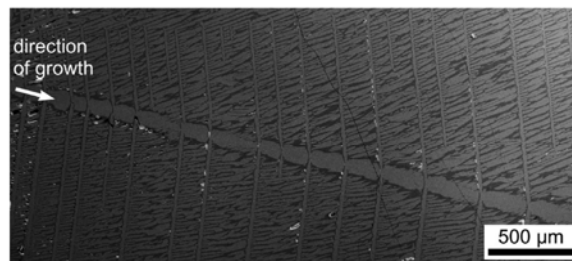
The volume ratio crystalline phase/amorphous phase was determined from SEM-micrographs using the software OPTIMAS (BioScan). Reliability was achieved by performing the evaluation ten times with varying settings. The limit of error is about ±2%.

## 3. Results

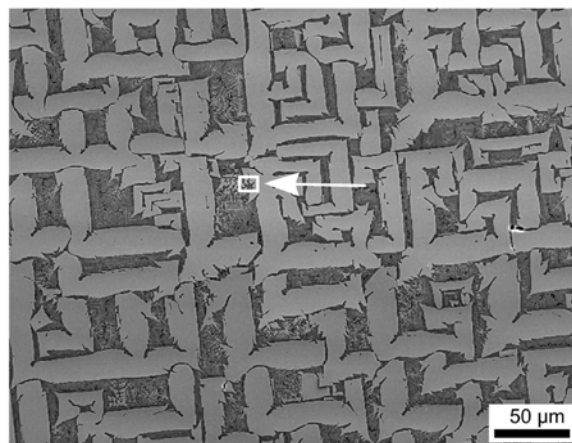
After a voltage of 4.8 V was attached between the Pt-crucible containing the melt and a platinum wire inserted into the glass melt with the composition Ba<sub>2</sub>TiSi<sub>2.75</sub>O<sub>9.5</sub>, nucleation occurred and crystals grew from the cathode toward the wall of the crucible. Within 4 min, the crystals grew about 15 mm, attributed to a crystal growth velocity of 6.25 × 10<sup>-5</sup> m/s. After this, the platinum wire with the adjacent crystals was drawn out of the melt.

Figure 1 shows part of a fresnoite dendrite cut parallel to the primary direction of crystal growth. The platinum wire at which the crystal growth was initiated is positioned to the left (not shown in the figure). The crystal phase is of light appearance. The core of the dendrite is seen with primary branches growing from it and secondary branches growing from the latter. The core grows primarily in the [001] direction, while the primary branches split off in the [100] and [010] directions. The secondary branches once again grow parallel to the core.

Figure 2 presents a SEM-micrograph of a sample cut perpendicular to the primary direction of growth. The crystallographic *c*-axis is perpendicular to the image plane in this case. Large, regular crystals are seen displaying similar morphologies. Figure 3 shows the region framed in Figure 2 in a higher magnification. Here, small crystals originating at the large fresnoite crystals are seen. The large crystals show very pronounced edges, and the small crystals seem to be more



**Figure 1.** SEM-micrograph of a sample cut parallel to the main growth direction.



**Figure 2.** SEM-micrograph of a sample cut perpendicular to the main growth direction. The framed area is presented in Figure 3.

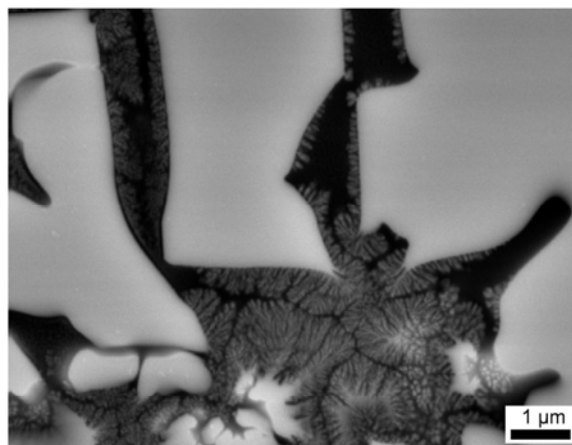
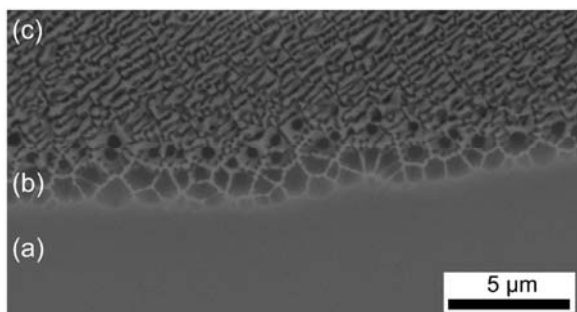


**Figure 3.** SEM-micrograph presenting the area framed in Figure 2 with a higher magnification.

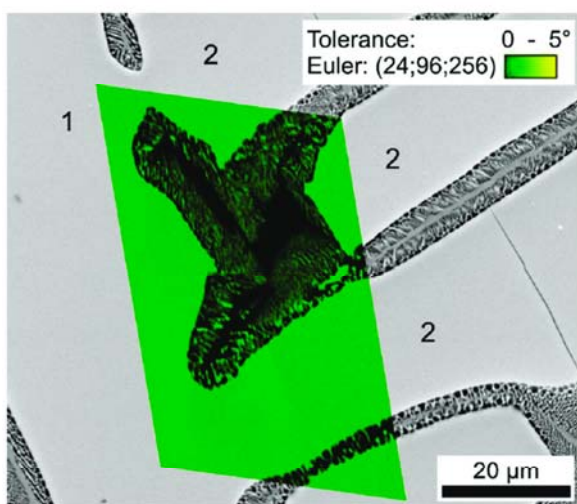
distinctive at these edges than along the straight sides of the crystal.

Figure 4 shows a region between the dendritic crystals in a cut parallel to the primary growth direction. At the bottom of Figure 4, a dendritic crystal (a) is shown. It is surrounded by a layer of honeycombs and a glassy phase (b). A lamellar structure is found in the volume between the crystals (c).

Figure 5 shows an SEM-micrograph, superimposed by an orientation map derived from an OIM-scan performed with a



**Figure 4.** SEM-micrograph of a primary crystal (a), the honeycomb area (b), and the crystallization in the volume between the dendritic crystals (c).



**Figure 5.** SEM-micrograph of dendritic fresnoite presenting primary (1) and secondary (2) dendrite branches overlaid by an orientation map of an OIM-scan.

step size of 70 nm. The micrograph shows large dendritic crystals with fine crystalline structures between them. Only EBSD-patterns attributable to crystalline fresnoite were obtained from the phases appearing brighter in the SEM-micrograph. The orientation map shows the orientation of the honeycombs and the lamellae to be exactly the same as the orientation of the primary (1) and secondary (2) branches of the dendrite. While all three secondary branches presented in the scan show the same orientation, only two of them show a visible connection to the primary branch. After eliminating unreliable points from the scan (black areas), 100% of the points are comprehended by the defined orientation. Almost all of the microstructure shown in Figure 2 shows the same behavior. Only very few crystals show a deviating orientation.

From the dark areas between the honeycombs and lamellae, EBSD-patterns could not be obtained. Analyses of the honeycomb and lamella-like areas in Figure 4 showed the lamella-like area to be 52% crystalline, while the honeycomb area is only about 26% crystalline.

In a scan covering a large area of the surface presented in Figure 1, three crystals deviating from the main orientation were found in one location. A scan with a step size of 350 nm was performed and is presented as an orientation map in

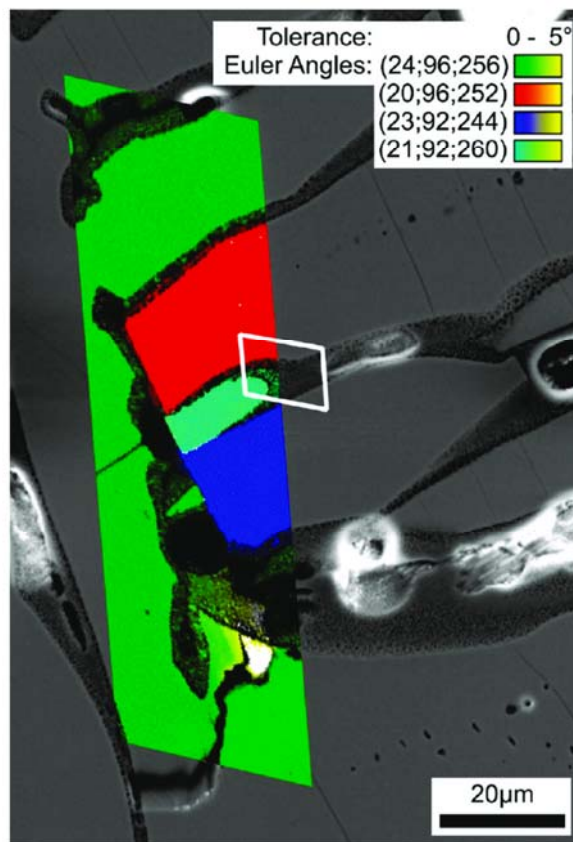


**Figure 6.** SEM-micrograph of fresnoite overlaid by an orientation map of an OIM-scan performed over the crystals of the main orientation (green) and deviating crystals (red, dark blue, and light blue). The frame outlines the area covered by the scan presented in Figure 5.

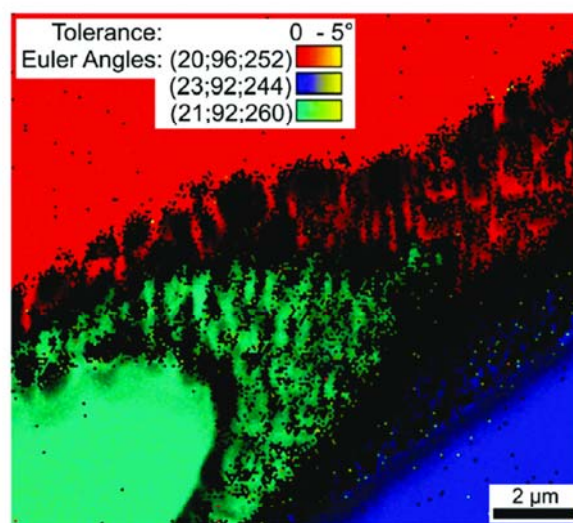


**Figure 7.** Orientation map of the high-resolution OIM-scan outlined in Figure 5 showing the orientation of the crystallization between dendritic crystals.

Figure 6 overlaying the SEM-micrograph of the area. While the large, primary crystals are clearly homogeneous in their

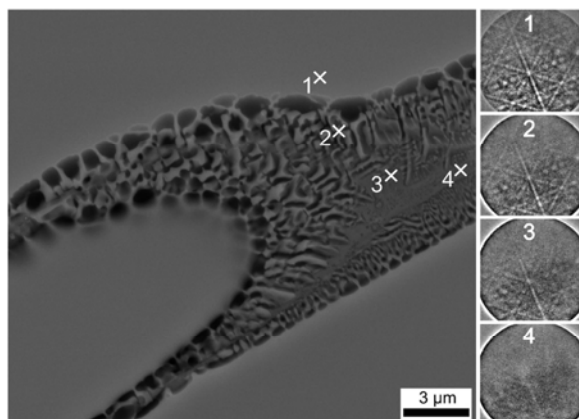


**Figure 8.** SEM-micrograph of the area scanned in Figure 7. EBSD-patterns obtained from locations 1–4 are presented.

respective orientation, the areas in between are not. A scan using a step size of 70 nm was performed over the area framed in Figure 6. The orientation map of this scan is presented in Figure 7. It shows the orientation of the honeycombs and the lamellae to be exactly the same as the orientation of the adjacent dendritic crystals. No EBSD-patterns could be obtained from the dark areas between the honeycombs and lamellae.

Figure 8 presents an SEM-micrograph of the area covered by the orientation map in Figure 7. It is clear that not every part of the sample delivering EBSD-patterns which cannot be reliably indexed is amorphous. While the honeycomb structures adjacent to the primary crystals are composed of crystalline bridges surrounding amorphous material, the area where the orientations should collide appears to be crystalline. Nevertheless, it was not possible to obtain reliable EBSD-data from this region in the scan, leaving it black in Figure 7.

The individual EBSD-patterns from this area presented in Figure 8 show the degrading image quality of patterns 1–4. While patterns 1–3 are well indexable, pattern 4 could not be indexed with acceptable reliability.

#### 4. Discussion

At a temperature of 1200 °C, the melt is below the liquidus temperature but nucleation is not observed. After the voltage is applied, crystallization is initiated at the cathode. It should be noted that nucleation solely occurs near the platinum wire, in contrast to conventional crystallization, which is the result of nucleation and crystal growth occurring throughout the sample.<sup>41</sup> The crystals form dendritic structures oriented with the *c*-axes perpendicular to the cathode.<sup>20,37</sup> In analogy to surface crystallization, this is due to kinetic selection.<sup>33</sup>

The large dendritic crystals cover about 57% of the area shown in Figure 1. The darker areas between these crystals are composed of two phases: one of them (lighter) is crystalline and in direct contact with the large crystals while the other (dark) is a residual glassy phase. These dendrites possess a very homogeneous orientation which also extends to the irregular structures between the dendritic crystals as presented in Figure 5, where they show the same orientation as the primary (marked “1” in Figure 5) and secondary (marked “2” in Figure 5) branches of the dendrite. Nearly all of the microstructure shown in Figure 1 exhibits the same behavior. Only very few crystals show a deviating orientation.<sup>20</sup>

The lamellar structures in the areas between the dendrites are significantly different from the structures observed by T. Höche et al.<sup>37</sup> While the lamellae were always perpendicular to the primary crystals, this is clearly not the case in Figures 4 and 8.

The fact that the deviating orientations of the main crystals in Figure 6 are copied by crystals in the intermediate area (see Figure 7) implies that the dendritic crystals serve as seed crystals to the honeycombs and lamellae. Concerning the orientation of the deviating dendritic crystals, this means that the deviation<sup>20</sup> must occur before the intermediate area crystallizes. If the crystallization between the large dendrites were the result of a secondary nucleation during cooling, the orientation of the crystals between the dendrites would not be exactly the same as that of the dendritic crystals. Because this is not the case, the crystals between the dendritic fresnoite are the result of epitaxial growth during a second step of crystallization at lower temperatures. A fourfold hierarchical crystalline structure is therefore observed in dendritic fresnoite: first the main trunk of the dendrite, then the primary and secondary branches, and finally the irregular structures in between the large crystals are formed.

The formation of the observed structures could be explained as follows: the melt does not have a stoichiometry identical with that of fresnoite but exhibits an excess in SiO<sub>2</sub>. Hence, the melt is depleted in barium and titanium during the course of the crystallization process. An eutectic occurs at  $x = 2.5$  in the phase diagram of the pseudobinary system Ba<sub>2</sub>TiSi<sub>2</sub>O<sub>8</sub>·*x*SiO<sub>2</sub>. The attributed liquidus temperature is 1252 °C.<sup>42</sup>

The sample composition, calculated from the stoichiometry and the respective densities, is attributed to a volume ratio Ba<sub>2</sub>TiSi<sub>2</sub>O<sub>8</sub>/SiO<sub>2</sub> = 84.87/15.13%. The observed volume ratio crystalline phase/amorphous phase as determined from the presented sample is Ba<sub>2</sub>TiSi<sub>2</sub>O<sub>8</sub>/SiO<sub>2</sub> = 79/21% and, thus, only about 5% below the theoretically achievable crystalline volume.

The eutectic composition is not supposed to crystallize at 1200 °C (the temperature where large dendrites are formed) because the crystallization of SiO<sub>2</sub> modifications such as quartz is not observed under the conditions supplied. Hence, the honeycomb- and lamellae-like structures are also not supposed to be formed at the temperature of 1200 °C.

Another indication that the observed structures are formed during cooling and not at the high temperature is the occurrence of crystals whose orientations deviate from that of the dendritic structure. These crystals are closely connected to the dendritic structure;<sup>20</sup> however, crystalline fresnoite bridges between the dendrite and the deviating crystals are not observed (compare Figures 5 and 6). According to ref<sup>20</sup>, these structures are probably formed by dendrite fragmentation.<sup>8</sup> If the honeycomb and lamellae structures were formed at high temperatures, the deviation of crystals from the orientation of the main dendrite due to dendrite fragmentation would not be possible.

During cooling, the crystallization of fresnoite continues due to the larger driving forces. It is likely that the observed structures are formed during the cooling process before nucleation in the intermediate areas occurs. The different quantities of crystals in the honeycomb area (26% crystals) and the lamellae (52% crystals) indicate that the dendritic crystals are surrounded by a zone depleted in some components necessary to form the crystals. When these ions diffuse into this area, epitaxial growth begins at the dendritic crystals forming the honeycomb layer. Once the crystallization transcends the area of depletion, the concentration of the crystal phase increases as



the lamellae are formed. This would also explain the continuation of the lattice at the planes described by T. Höche at the boundaries between dendrite and lamellae.<sup>37</sup>

Because this process would start from all surfaces at almost the same time, the resulting crystallization fronts would collide in the middle of the areas between the dendritic crystals, leading to the structures observed in Figures 5 and 8. The inability to obtain reliable EBSD-data from the area of crystal collision can be caused by very small, finely branching crystals<sup>37</sup> and/or heavily distorted crystal lattices in this region. Pattern 4 in Figure 8 shows a very weak version of patterns 1–3, allowing the speculation that the orientation of crystals within the black area in Figure 7 will probably show the orientations of the respective neighboring regions. It might also be the Ba<sub>5</sub>Si<sub>8</sub>O<sub>21</sub> found by T. Höche et al.,<sup>37</sup> but this is unlikely due to the weak pattern visible in pattern 4 in Figure 8. In any case, the very small size of Ba<sub>5</sub>Si<sub>8</sub>O<sub>21</sub> observed in the TEM would inhibit the formation of an indexable EBSD-pattern in an SEM.

### 5. Conclusions

Dendritic primary crystals serve as seed crystals for epitaxial growth, resulting in a four step hierarchy of crystallization. The homogeneity of crystal orientation thus extends from the dendritic crystals to the intermediate area. Because the honeycomb and lamellar structures copy the orientation of deviating primary crystals, the epitaxial growth must have occurred after the primary crystals grew and deviated from the main orientation of the dendrite.

### References

- Haxhimali, T.; Karma, A.; Gonzales, F.; Rappaz, M. *Nat. Mater.* **2009**, *5*, 660–664.
- Langer, J. S. *Rev. Mod. Phys.* **1980**, *52*, 1–28.
- Warren, J. *Nat. Mater.* **2006**, *5*, 595–596.
- Ben-Jacob, E.; Garik, P. *Nature* **1990**, *343*, 523–530.
- Gránásy, L.; Pusztai, T.; Warren, J. A.; Douglas, J. F.; Börzsönyi, T.; Ferréiro, V. *Nat. Mater.* **2003**, *2*, 92–96.
- Gránásy, L.; Pusztai, T.; Börzsönyi, T.; Warren, J. A.; Douglas, J. F. *Nat. Mater.* **2004**, *3*, 645–650.
- Boettinger, W. J.; Warren, J. A.; Beckermann, C.; Karma, A. *Ann. Rev. Mater. Res.* **2002**, *32*, 163–194.
- Rettenmayr, M. *Int. Mater. Rev.* **2009**, *54*, 1–17.
- Mullins, W. W.; Sekerka, R. F. *J. Appl. Phys.* **1963**, *34*, 323–329.
- Somboonsuk, K.; Mason, J. T.; Trivedi, R. *Metall. Trans.* **1984**, *15A*, 967–975.
- Sekerka, R. F. *J. Cryst. Growth* **1993**, *128*, 1–12.
- Gutzow, I.; Schmelzer, J. In *The Vitreous State: Thermodynamics, Structure, Rheology, and Crystallization*; Springer: Berlin, 1995.
- Avramov, I.; Rüssel, C.; Avramova, K. *J. Non-Cryst. Solids* **2004**, *337*, 220–225.
- Gutzow, I.; Grigorova, T.; Todorova, S. *J. Non-Cryst. Solids* **2002**, *304*, 4–18.
- Carl, R.; Rüssel, C. *Eur. J. Glass Sci. Technol. B* **2007**, *48* (4), 271–275.
- Keding, R.; Rüssel, C. *J. Mater. Sci.* **2004**, *39*, 1433–1435.
- Keding, R.; Stachel, D.; Rüssel, C. *J. Non-Cryst. Solids* **2001**, *283*, 137–143.
- Gerth, K.; Rüssel, C.; Keding, R.; Schlievoigt, P.; Dunken, H. *Phys. Chem. Glasses* **1999**, *40*, 135–139.
- Keding, R.; Rüssel, C. *Ber. Bunsen-Ges. Phys. Chem.* **1996**, *100*, 1515–1518.
- Wisniewski, W.; Nagel, M.; Völksch, G.; Rüssel, C. *J. Cryst. Growth Des.* **2010**, *10*, 1939–1945.
- Alfors, J. T.; Stinton, M. C.; Matthews, R. A.; Pabst, A. *Am. Mineral.* **1963**, *50*, 314–341.
- Moore, P. B.; Louisnathan, S. J. *Z. Kristallogr.* **1969**, *130*, 438.
- Halliyal, A.; Bhalla, A. S.; Newnham, R. E.; Cross, L. E.; Gururaja, T. R. *J. Mater. Sci.* **1982**, *17*, 295–300.
- Halliyal, A.; Bhalla, A. S.; Markgraf, S. A.; Cross, L. E.; Newnham, R. E. *Ferroelectrics* **1985**, *62*, 27–38.
- Halliyal, A.; Bhalla, A. S.; Cross, L. E. *Ferroelectrics* **1985**, *62*, 3–9.
- Halliyal, A.; Safari, A.; Bhalla, A. S.; Newnham, R. E.; Cross, L. E. *J. Am. Ceram. Soc.* **1984**, *67*, 331–335.
- Ting, R. Y.; Halliyal, A.; Bhalla, A. S. *Appl. Phys. Lett.* **1984**, *44*, 852–854.
- Ma, E. *Nat. Mater.* **2003**, *2*, 7–8.
- Hays, C. C.; Kim, C. P.; Johnson, W. L. *Phys. Rev. Lett.* **2000**, *84*, 2901–2904.
- Rüssel, C. *J. Non-Cryst. Solids* **1997**, *219*, 212–218.
- Masai, H.; Fujiwara, T.; Mori, H.; Benino, Y.; Komatsu, T. *J. Appl. Phys.* **2007**, *101*, 033530.
- Masai, H.; Fujiwara, T.; Mori, H. *J. Appl. Phys.* **2007**, *101*, 123505.
- Wisniewski, W.; Nagel, M.; Völksch, G.; Rüssel, C. *J. Cryst. Growth Des.* **2010**, *10*, 1414–1418.
- Keding, R.; Rüssel, C. *J. Non-Cryst. Solids* **2005**, *351*, 1441–1446.
- Keding, R.; Rüssel, C. *J. Non-Cryst. Solids* **1997**, *219*, 136–141.
- Keding, R.; Rüssel, C. *J. Non-Cryst. Solids* **2000**, *278*, 7–12.
- Höche, T.; Keding, R.; Rüssel, C. *J. Mater. Sci.* **1999**, *34*, 195–208.
- Cabral, A. A.; Folkin, V. M.; Zanutto, E. D.; Chinaglia, C. R. *J. Non-Cryst. Solids* **2003**, *330*, 174–186.
- Schwartz, A. J.; Kumar, M.; Adams, B. L. In *Electron Backscatter Diffraction in Materials Science*; Kluwer Academic/Plenum Publishers: New York, 2000.
- Baba-Kishi, K. Z. *J. Mater. Sci.* **2002**, *37*, 1715–1746.
- Rangarajan, B.; Shrout, T.; Lanagan, M. J. *Am. Ceram. Soc.* **2009**, *92*, 2642–2647.
- Keding, R. Ph.D. Thesis, Jena University, 1997.

### 3.4.

W. Wisniewski, T. Zschechel, G. Völksch and C. Rüssel

**Electron Backscatter Diffraction of  $\text{BaAl}_2\text{B}_2\text{O}_7$  Crystals Grown  
from the Surface of a  $\text{BaO} \cdot \text{Al}_2\text{O}_3 \cdot \text{B}_2\text{O}_3$  Glass**

CrystEngComm, 2010, **12**, 3105-3111.

<http://pubs.rsc.org/en/Content/ArticleLanding/2010/CE/C004582A>

# Electron backscatter diffraction of $\text{BaAl}_2\text{B}_2\text{O}_7$ crystals grown from the surface of a $\text{BaO} \cdot \text{Al}_2\text{O}_3 \cdot \text{B}_2\text{O}_3$ glass

Wolfgang Wisniewski, Tilman Zschechel, Günter Völksch and Christian Rüssel\*

Received 22nd March 2010, Accepted 12th May 2010

DOI: 10.1039/c004582a

A glass with the composition  $\text{BaO} \cdot \text{Al}_2\text{O}_3 \cdot \text{B}_2\text{O}_3$  was annealed at 780 °C for 8 h. The samples were investigated by electron backscatter diffraction (EBSD). At the surface of the samples a first layer composed of  $\text{BaAl}_2\text{B}_2\text{O}_7$  crystals oriented with their crystallographic *c*-axes perpendicular to the surface was formed. This layer was highly oriented and up to 20 µm thick. In a subsequent layer, the crystals were oriented with their crystallographic *c*-axes parallel to the surface. While the first layer was caused by oriented nucleation at the surface, the orientation of the secondary layer was caused by kinetic selection of spherulitically grown crystals.

## Introduction

Oriented glass-ceramics show great potential for achieving anisotropic material properties. For example, fresnoite containing glass-ceramics have been of great interest due to their piezoelectric and surface acoustic wave properties in combination with the possibility of achieving highly oriented and even polar materials by surface crystallisation<sup>1–4</sup> or by electrochemically induced nucleation.<sup>5–8</sup>

A trigonal<sup>9</sup> and a monoclinic phase<sup>10</sup> of  $\text{BaAl}_2\text{B}_2\text{O}_7$  have been reported. The trigonal phase (space group no. 155) will be the only phase of  $\text{BaAl}_2\text{B}_2\text{O}_7$  discussed in this paper. Due to the rhombohedral centering of the Bravais-lattice, the trigonal phase is commonly described as rhombohedral. In glass-ceramics containing rhombohedral  $\text{BaAl}_2\text{B}_2\text{O}_7$ -crystals, a close to zero or even negative thermal expansion has been reported.<sup>11–14</sup> Using high temperature X-ray diffraction (XRD), it has been shown that the change in the relative length of the *a*-axis of rhombohedral  $\text{BaAl}_2\text{B}_2\text{O}_7$  is approximately zero from room temperature up to 150 °C and shows slightly positive values at higher temperatures. By contrast, the relative length of the *c*-axis decreases continuously in the temperature range from 25 to 500 °C.<sup>11,13</sup> A crystal growth velocity of  $5 \times 10^{-7} \text{ m s}^{-1}$  at 780 °C has been reported in ref. 14. It has further been shown that the microstructure affects the thermal expansion coefficient. Sintered glass-ceramics or glass-ceramics containing nucleation agents such as platinum, are composed of small, randomly oriented crystals and exhibit slightly negative thermal expansion coefficients.<sup>15</sup> Bulk glass samples of stoichiometric  $\text{BaAl}_2\text{B}_2\text{O}_7$  prepared without adding nucleation agents show a surface crystallised layer after thermal annealing. Such samples show strongly negative thermal expansion coefficients. The observed surface layers were up to 700 µm thick.<sup>12,13</sup> XRD-patterns obtained from the surface of the samples showed a (003)-peak with a much higher intensity in comparison to the respective JCPDS data.<sup>11–14</sup> This is attributed to crystals oriented with their *c*-axes perpendicular to the surface of the sample. If platinum is

added to the batch the glass is melted from, bulk crystallisation of  $\text{BaAl}_2\text{B}_2\text{O}_7$  occurs. In this case the sizes of the crystals are significantly smaller.<sup>12,13</sup>

Surface crystallisation leading to crystals oriented with the *c*-axis perpendicular to the surface has also been reported from fresnoite containing glass-ceramics.<sup>2–4</sup> In this case, the reason of the orientation has been found to be kinetic selection. Directly at the surface, however, a different orientation was observed.<sup>1</sup>

Surprisingly, the crystallisation of the  $\text{BaO} \cdot \text{Al}_2\text{O}_3 \cdot \text{B}_2\text{O}_3$  glass is accompanied by a volume expansion. This is unusual for the crystallisation of glass<sup>13</sup> but for example also observed during the crystallisation of cordierite glass.<sup>15</sup> Another notable property of  $\text{BaO} \cdot \text{Al}_2\text{O}_3 \cdot \text{B}_2\text{O}_3$  glass-ceramics is their unusual high ionic conductivity which is accompanied by a very small activation energy (<0.5 eV).<sup>16</sup>

This paper provides a study on electron backscatter diffraction of layers crystallised from the surface of a glass with the composition  $\text{BaO} \cdot \text{Al}_2\text{O}_3 \cdot \text{B}_2\text{O}_3$ . The phase formation and the crystal orientation are described.

## Electron backscatter diffraction (EBSD)

In the past few years, EBSD became a standard method in mineralogy and metallography. By contrast, few reports of EBSD as a method to characterise glass-ceramics are found in the literature.<sup>1,5,17–19</sup> A recent review on the applications of EBSD in materials science given by Randle<sup>20</sup> also does not mention the investigation of glass-ceramics.

EBSD is a powerful tool for the identification of certain crystal phases in the microstructure and for the local detection of crystal orientations. The method is based on the analysis of Kikuchi bands detected in diffraction patterns obtained from a crystalline sample. The information depth of EBSD is limited to 10–50 nm.<sup>21,22</sup> Hence EBSD is a method for the surface near characterisation of materials.

Using a scanning electron microscope (SEM) equipped with an EBSD-unit combines the ability of studying the morphology and crystallographic relationships of a crystalline solid simultaneously.

Otto-Schott-Institut, Jena University, Fraunhoferstr. 6, 07743 Jena, Germany. E-mail: ccr@uni-jena.de

While a single EBSD-pattern provides information on the crystal at the spot where it was obtained, a grid of EBSD-patterns allows the description of the crystallographic properties of a microstructure and is referred to as Orientation Imaging Microscopy (OIM). The latter describes scanning a surface in a defined step size, collecting and indexing EBSD-patterns so that each point in an OIM-map represents the information of an indexed EBSD-pattern. Indexing a diffraction pattern is achieved by a voting system and characterised by a number of indexing parameters such as the image quality value (IQ), votes, the fit-factor, and the confidence index (CI) (see *e.g.* A. J. Schwartz *et al.*<sup>21</sup>). The orientation of a crystal is usually defined by the three Euler angles  $\varphi_1$ ,  $\Phi$ , and  $\varphi_2$ . The IQ-value of an EBSD-pattern is affected by numerous parameters, however, the main input from the sample is the perfection of the crystal lattice.<sup>21</sup> Since glass has no lattice to produce a diffraction pattern, points in an IQ map obtained from glass get very low IQ-values. In many cases the IQ-value enables to distinguish between amorphous and crystalline phases. A relatively low IQ-value, in principle, should also be a result of a very thin layer of glass covering a crystal or, for example, of tensions and defects within the crystal lattice.

The crystal phase  $\text{BaAl}_2\text{B}_2\text{O}_7$  has a rhombohedral symmetry; in the following the crystal lattice is indexed in analogy to a hexagonal lattice, *i.e.* the [0001]-direction is parallel to the (hexagonal)  $c$ -axis. The (0001)-pole figure (PF) is very suitable to illustrate orientations of  $\text{BaAl}_2\text{B}_2\text{O}_7$ , since the pole of the (0001)-plane is parallel to the crystallographic  $c$ -axis of the unit cell. An example is shown in Fig. 1. Here, the effects of the individual Euler angles ( $\varphi_1; \Phi; \varphi_2$ ) on the (0001)-PF of  $\text{BaAl}_2\text{B}_2\text{O}_7$  are presented. The Euler combination of (0;0;0) in Fig. 1a describes an orientation with the  $c$ -axis perpendicular to the surface of the sample.  $\Phi$  describes the tilt between the  $c$ -axis and the normal of

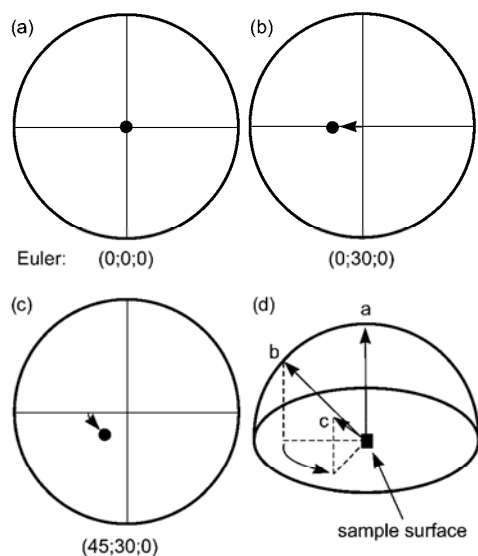


**Fig. 1** The effect of Euler angles on the (0001)-pole figure of rhombohedral  $\text{BaAl}_2\text{B}_2\text{O}_7$ : (a) starting point, (b) variation of  $\Phi$ , (c) variation of  $\varphi_1$ , (d) overview. The angle  $\varphi_2$  has no effect on this pole figure.

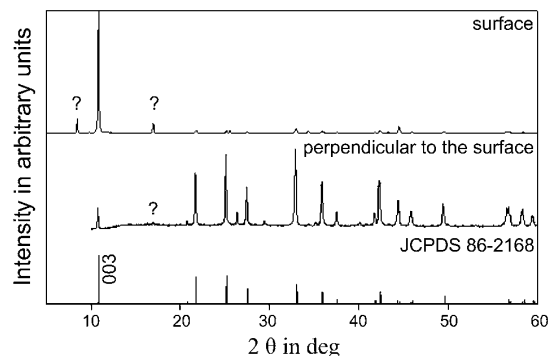


**Fig. 2** XRD-patterns recorded from the surface and the volume in comparison to the intensities according to the JCPDS-file.

the sample (Fig. 1b) while the rotation of the  $c$ -axis around the normal of the sample is described by  $\varphi_1$  (Fig. 1c). The angle  $\varphi_2$  describes the rotation around the  $c$ -axis and therefore has no input into the (0001)-PF of  $\text{BaAl}_2\text{B}_2\text{O}_7$ .

An Inverse Pole Figure (IPF) is a reduction of the pole figure by symmetric operations usually to a unit triangle containing all orientations or their symmetric equivalents. It is therefore a useful plot for an overview of all orientations appearing in a scan.

## Results and discussion

### X-Ray diffraction (XRD)

The melted glass was fully transparent and showed no signs of crystallisation. XRD-patterns of the glassy samples did not exhibit any significant peak. The patterns obtained from the surface of the crystallised sample and the same samples cut perpendicular to the surface are presented in Fig. 2 in comparison to the XRD-lines of rhombohedral  $\text{BaAl}_2\text{B}_2\text{O}_7$  according to JCPDS Nr. 86-2168. The XRD-pattern obtained from the surface shows a (003) peak of extremely high intensity. Both patterns show peaks of minor intensity marked with a question mark (?) which cannot be attributed to either rhombohedral  $\text{BaAl}_2\text{B}_2\text{O}_7$  or any other practically acceptable phase in the used database. This is in agreement with previously published results.<sup>11–13,16</sup>

### Indexing $\text{BaAl}_2\text{B}_2\text{O}_7$

A material file for indexing EBSD-patterns was created by using the data published in ref. 9.

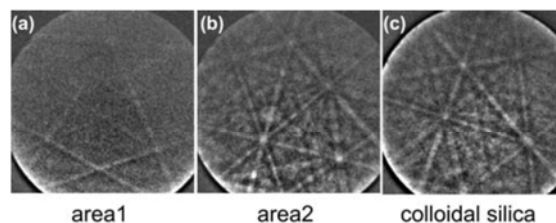


**Fig. 3** EBSD-patterns obtained from area 1 (a) and area 2 (b) of the untreated surface and a pattern obtained from a surface polished by colloidal silica (c).

Fig. 3 shows three EBSD-patterns obtained from two different points of the untreated surface (see Fig. 3(a) and (b)) and a pattern recorded from a surface polished using colloidal silica (see Fig. 2(c)). Pattern (a) is relatively weak while the patterns (b) and (c) are much more intense and show a lot more Kikuchi bands.

EBSD-patterns obtained from the unpolished surface quite often lead to the mathematical exception of two orientation solutions achieving the same number of votes, resulting in a CI-value (which is calculated from the first two orientation solutions, see ref. 21) of 0.000. Fig. 3(a) shows a pattern frequently obtained from the untreated surface of the crystallised sample. The indexing parameters for the material file without “band width ratio matching” given in Table 1 illustrate the described problem: both orientation solutions **1** (Euler angles: (246;5;229)) and **2** (Euler angles: (66;175;11)) lead to the same unit cell, the only difference is, that solution **1** is attributed to a *c*-axis pointing OUT of the sample, while the *c*-axis of solution **2** points INTO the sample. This is also indicated by the  $\Phi$ -values of each orientation deviating from 0 by only 5°. The only difference between the orientation solutions **1** and **2** in Table 1 is found in the “*d*-space fit” (which compares the detected band width to the theoretical value), but even including the band width into the indexing process by activating the “band width ratio matching” only leads to a CI-value of 0.024 as presented in the lower part of Table 1, while significantly reducing the votes attributed to each orientation solution.

Altogether, 14.0% of the points attributable to the crystalline phase in the OIM-scan presented in Fig. 5 show a CI-value of 0.000. Almost all of them indicate an orientation with the *c*-axis perpendicular to the surface.

Due to this effect, the CI-value could not be used to reliably filter the EBSD-data for scans obtained from the untreated surface of the sample. At least 14% of the points in the scan presented in Fig. 5 would falsely be excluded due to the indexing problem described in Table 1 if a minimum CI-value of 0.100 was applied as a filter. Only a very small part of the points in Fig. 5 are truly the result of very bad EBSD-patterns (e.g. from the crack), so that they only have an insignificant effect on the calculated texture.

#### Untreated surface of the crystallised sample

The surface of the crystallised samples showed many cracks. This can be explained by the volume expansion during crystallisation.<sup>11–13</sup> While a volume expansion during the crystallisation of a glass is rarely observed due to a usually denser packing of the

**Table 1** Indexing parameters of the first two orientation solutions for the pattern presented in Fig. 3(a) with and without band width ratio matching and corresponding CI values

Solution	Votes	Fit <sup>a</sup>	<i>d</i> -Space fit
Without band width ratio matching: CI = 0.000			
<b>1</b>	93	0.90	0.86
<b>2</b>	93	0.90	1.03
With band width ratio matching: CI = 0.024			
<b>1</b>	37	0.91	1.00
<b>2</b>	33	0.96	1.03

crystalline structure,<sup>23</sup> it is also found during the crystallisation of cordierite from a MgO/Al<sub>2</sub>O<sub>3</sub>/SiO<sub>2</sub> glass with the same composition.<sup>15</sup>

EBSD-patterns of varying quality were obtained from the entire surface of the sample. Scans performed on the untreated surface showed the material to be locally susceptible to damage by electron beam. This was not the case if polished surfaces were studied.

Fig. 4 presents the first  $\mu\text{m}$  of two OIM-scans performed with step sizes of 0.20  $\mu\text{m}$  (in the following denoted as scan (a)) and 1.00  $\mu\text{m}$  (scan (b)). In scan (a), a significant reduction of the IQ-value appears after the first line at the top of the scan. This is not as significant in scan (b). The reduction of image quality was quantified by comparing the average IQ-value of the first line to the average IQ-value of a subsequent line. The results given in Table 2 show the IQ-loss in scan (a) (56.6%) to be twice as large as in scan (b) (27.8%).

While a grain like structure is visible in scan (b), this morphology can hardly be observed in scan (a). In both scans, areas of higher IQ-values were identified. These areas seem to be unaffected by the reduction of the IQ-value in scan (a). To separate the area strongly affected by the electron beam (area 1) from the area relatively unaffected by the electron beam (area 2), a cutoff value (see Table 2) was defined for the IQ-values of each scan. Points with IQ-values smaller than the cutoff value are attributed to area 1 while points with IQ-values above the cutoff value are attributed to area 2. The values given in Table 2 are based on the entire OIM-scans and clearly show the average IQ-value of area 2 to be more than twice as large as the average IQ-value of area 1. Points attributed to area 2 cover 14.8% and 12.1% of the surface covered by the scans (a) and (b), respectively. Because of the damage to the sample, a significant reduction of the IQ-value was observed if step sizes of up to 0.25  $\mu\text{m}$  were used. A step size of at least 0.30  $\mu\text{m}$  was necessary



**Fig. 4** Topmost segments of the IQ-maps of two OIM-scans performed with different step sizes on the unpolished surface of crystallised samples.

**Table 2** IQ-values describing the pattern degradation due to the electron beam and the difference between area 1 and area 2. The cutoff values were set by the authors

Stepsize:	0.20 $\mu\text{m}$	1.00 $\mu\text{m}$
Average IQ (first line)	2555	1863
Average IQ (later line)	1110	1345
IQ-loss [%]	56.6	27.8
IQ cutoff value	1500	2000
% of points over cutoff	14.8	12.1
% of points under cutoff	85.2	87.9
Average IQ over cutoff	2353	2692
Average IQ under cutoff	853	1199

to obtain scans without a significant decrease in the IQ-value after the first line of a scan.

The observed pattern degradation indicates a change in the material, *e.g.* swelling of the residual glass phase on the surface of the sample. If a step size of 0.25  $\mu\text{m}$  or smaller is used, the damage at one point is close enough to the next point to significantly reduce the pattern quality there. The first line of a scan is not affected by this because the tilt of the sample transforms the spot of the focus into an ellipse.<sup>21</sup> The dimension of the affected area is therefore much larger in the *x*-direction than in the *y*-direction of a scan. If a step size larger than 0.25  $\mu\text{m}$  is used, the local damage does not influence the next point of the scan significantly. The pattern degradation is not observed on polished surfaces, indicating that the crystals themselves are not the reason of the degradation.

Due to the varying quality of EBSD-patterns obtained from the untreated surface, the OIM-scan of the untreated surface in Fig. 5 was performed with a binning of  $2 \times 2$  (exposure: 0.5 s, gain: 2.23) to enable a homogeneous detection of bands in the EBSD-patterns.

The weak EBSD-patterns observed at the surface are probably the result of a very thin layer of glass covering the crystals. Because of the very limited penetration depth of EBSD,<sup>21,22</sup> this layer of glass should not be thicker than a few nm. The glass would reduce the crystalline fraction of the information volume producing the EBSD-pattern, resulting in the weak patterns observed (see Fig. 3a). A thin layer of glass covering the surface crystallised layer has already been described in the cordierite system.<sup>24</sup>

Fig. 5 shows the combination of the colored IPF-map and the grey scale IQ-map of an OIM-scan performed on the untreated surface of a crystallised sample with a step size of 0.30  $\mu\text{m}$ . The red color is very dominant, indicating a strong (0001)-orientation of the crystals at the surface of the sample (see IPF-scale). The points attributed to area 2 appear brighter than those attributed to area 1 due to higher IQ-values indicating stronger EBSD-patterns. The equal area pole figure—in Fig. 5—of a texture calculated for the presented scan shows that the *c*-axes of the crystals are oriented perpendicular to the surface of the sample with a probability up to 72.6 times higher than in a randomly

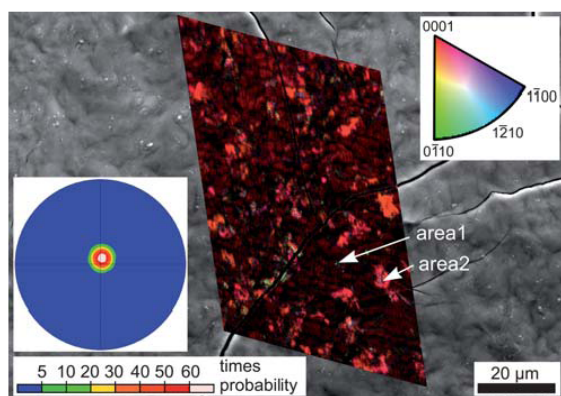


Fig. 5 IPF-map of an OIM-scan of the unpolished surface superimposed on an SEM-image of the surrounding area. The results of a texture calculated from the scan are presented in the (0001)-PF.

oriented material. The slight deviation of the orientation from the normal of the surface is probably due to a slight imperfection in the mounting of the sample, slightly tilting the surface. The grain-like structure observed in Fig. 5 indicates a varying thickness of the glassy layer.

### Polished surfaces of the sample

After the samples were cut perpendicular to the surface and subsequently polished, a crystallised layer of 680 (see Fig. 6) to about 800  $\mu\text{m}$  was clearly identified at the former surface of the sample. OIM-scans of this area (see *e.g.* the IPF-map in Fig. 7) showed the *c*-axis of  $\text{BaAl}_2\text{B}_2\text{O}_7$ -crystals to be predominantly oriented parallel to the former surface, as indicated by the orientations displayed in Fig. 7. The equal area (0001)-PF in Fig. 7 is attributed to the texture calculated from the presented

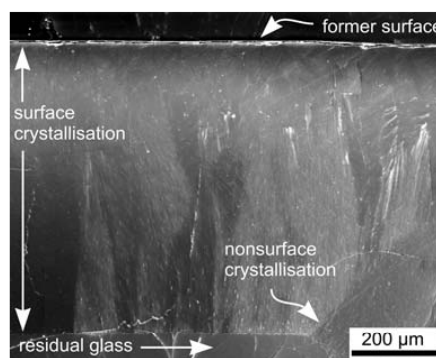


Fig. 6 SEM-image of the layer of crystallisation at the former surface of the sample.

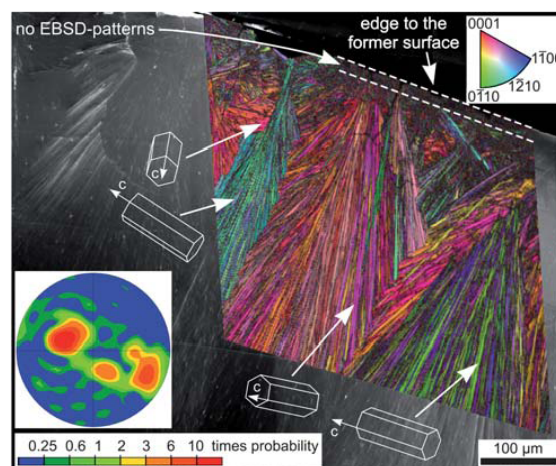


Fig. 7 IPF-map of an OIM-scan obtained from the crystallisation at the former surface superimposed on an SEM-image of the area. The sketched unit cells showcase orientations of crystals in occurring colors. An area where no acceptable EBSD-data were obtainable is indicated by the dashed lines. The (0001)-PF of a texture calculated from the scan is presented.

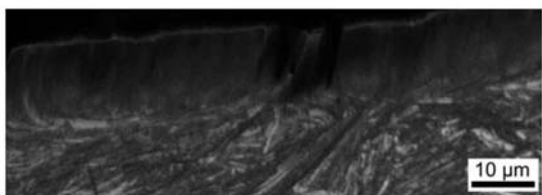


Fig. 8 IQ-map of an OIM-scan performed on the edge of a sample cut perpendicular to the former surface.

scan. It shows higher probabilities for orientations with the *c*-axes parallel to the surface. Because this orientation is only related to one axis, this second layer (layer 2) shall be described as “semi-oriented”. Only points with a CI-value over 0.100 were considered for the texture analysis.

The morphology of the similarly oriented areas in Fig. 7 indicates a point of origin near the surface from which the crystals grow into the volume of the sample. Unreliably indexed points were not excluded from the IPF-map in Fig. 7 to highlight a region of material 10–20 μm thick (dotted lines in Fig. 7) near the former surface from which acceptable EBSD-information was not obtained. These points were unreliably indexed and random orientations attributed (the step size was 1.00 μm).

The IQ-map of a scan performed with a step size of 0.20 μm at the edge to the former surface of the sample is presented in Fig. 8. There is a clearly discernible layer about 10–20 μm thick between the former surface of the sample and the area where crystalline structures are visible. In the following, this topmost layer will be denoted as layer 1, while the deeper parts of the surface crystallised layer will be denoted as layer 2. Despite extensive efforts it was not possible to prepare a sample with a polish perpendicular to the surface allowing EBSD-patterns to be obtained from layer 1.

In a further approach to analyse layer 1, another sample with a curved surface was polished from the top. The resulting surface, sketched in Fig. 9, showed an area attributable to layer 1 at the edge of the polished area.

A series of 15 slightly overlapping OIM-scans of approximately  $40 \times 5 \mu\text{m}^2$  was performed with a step size of 0.15 μm at the edge of the polished area of the sample. The first scan of this series was performed at the lowest visible edge of the tilted sample and therefore on the unpolished surface, as indicated in Fig. 9. The textures of these individual scans were calculated and are presented in equal area pole figures (see Fig. 10). A dominant orientation of the crystals with their *c*-axes perpendicular to the surface of the sample is observed only in the first 3 scans (*i.e.* up to about 15 μm from the surface). This orientation corresponds to the results from the unpolished surface presented in Fig. 5. The maximum orientation is reached in the first scan with a value about 60 times higher than in a randomly oriented material.

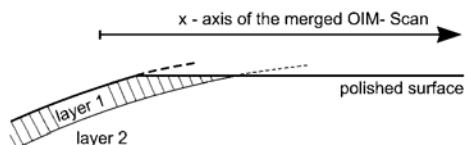


Fig. 9 Sketch of the prepared cut plane containing layers 1 and 2.

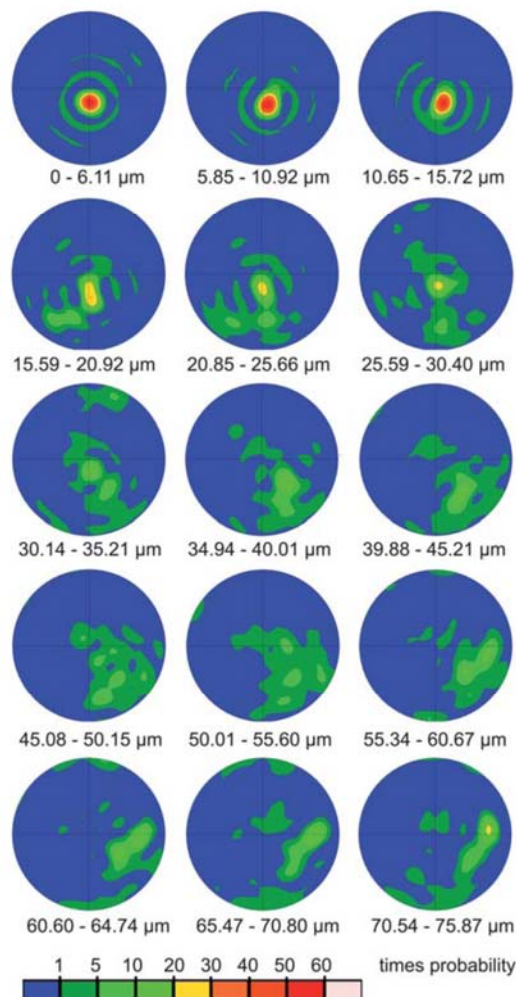


Fig. 10 Texture plots of 15 consecutive OIM-scans performed on a surface prepared as shown in Fig. 9.

After the first three scans, the predominant orientations of the crystals become more diverse leading to lower probabilities and show *c*-axes increasingly parallel to the surface. After 45 μm no orientation is more probable than 20 times higher than in a randomly oriented material, and orientations at the outer limit of the pole figures indicate an increasing probability of *c*-axes parallel to the surface. Fig. 11 shows the IPF-map of the merger of the 15 scans. Immediately at the surface, the crystals exhibit the orientation (a). The first crystal which shows an orientation with the *c*-axis parallel to the surface appears about 16 μm from the surface (orientation (b)). The last crystal showing an orientation attributable to the orientation found in layer 1 (orientation (c)) is found after about 40 μm.

#### The mechanism of crystallisation

During crystallisation, two distinct crystallised layers are formed at the surface: a topmost layer (layer 1) of highly oriented crystals

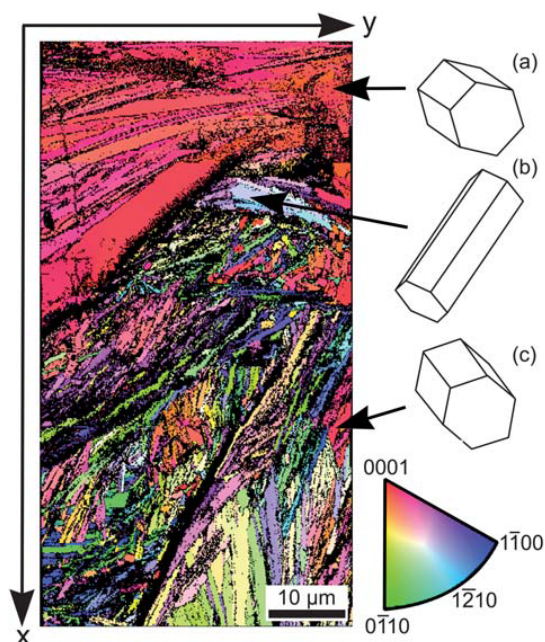


Fig. 11 IPF-map of the merger of the 15 performed OIM-scans. Local orientations are illustrated.

about 10–20  $\mu\text{m}$  thick (see Fig. 8) with their  $c$ -axes perpendicular to the surface (see Fig. 10), and a layer with a lower degree of orientation (layer 2) with the  $c$ -axes parallel to the surface (see Fig. 7). Layer 2 possesses a significantly higher thickness which is in the range from 600 to 800  $\mu\text{m}$  (see Fig. 6). Additionally, volume crystallisation occurs as an independent process under the conditions supplied.

The formed crystals possess the shape of slabs. This can be deduced from the fact that the crystals of layer 2 appear as needles in Fig. 7 (preparation from the side) and Fig. 11 (preparation from the top). If the crystals had needle-like shape, they would appear as ellipses in at least one of the perspectives. All detected orientations show  $c$ -axes perpendicular to the long axes of the crystals. It can therefore be concluded that crystal growth occurs mainly in directions perpendicular to the  $c$ -axis.

While a crystal growth velocity of  $5 \times 10^{-7} \text{ m s}^{-1}$  at 780  $^{\circ}\text{C}$  has been reported,<sup>14</sup> a description of the crystal morphology is not found in the literature. Due to the observed anisotropic growth of the crystals, the determined crystal growth velocity in ref. 14 should only apply to the growth in the preferred directions perpendicular to the  $c$ -axis. The crystal growth velocity in [0001] direction, however, is significantly smaller.

Apart from layer 1, crystal growth mainly occurs by slabs originating from a nucleus and growing outwards radially. This leads to the spherulites observed in the volume and the semi-orientation of layer 2 indicated by the (0001)-PF presented in Fig. 7. The latter is caused by spherulites originating from near the surface. The crystals hinder each other during growth. This leads to layer 2 in which the  $c$ -axes of the crystals are oriented parallel to the surface as indicated in Fig. 7.

The high intensity of the (003)-peak in the XRD-patterns obtained from the untreated surface is caused by layer 1 and is in agreement with results previously reported.<sup>11–13</sup> By contrast, the pattern recorded perpendicular to the surface of the sample does not show an intense (003)-peak.

Since nearly all EBSD-patterns obtained from the untreated surface of the crystallised sample represent orientations with the  $c$ -axes perpendicular to the surface, the nucleation at the surface does not occur in a random orientation. It should hence be assumed that the formation of nuclei with their crystallographic  $c$ -axes perpendicular to the surface is thermodynamically advantageous due to smaller surface energies. The observed orientation of rhombohedral  $\text{BaAl}_2\text{B}_2\text{O}_7$  is therefore not caused by a kinetic selection of crystals as previously proposed.<sup>11,13</sup>

If the assumption of an oriented nucleation at the surface of the sample is correct, crystallisation would occur in two steps: during step 1, the nuclei are formed and mainly grow parallel to the surface because the crystal growth velocity is largest in these directions. Within a comparably short period of time, layer 1 thus covers the entire surface. Areas of nucleation (area 2) would be indicated by immediate contact of the crystals to the surface. The crystals, however, do not grow ideally parallel to the surface (as indicated by the ring of orientations in the PF in Fig. 5), because the surface is not completely flat due to the volume expansion during crystallisation. Hence, the crystals dive beneath the surface. Crystal growth would later occur slowly in the [0001] direction and thus towards the surface and into the volume. Since the chemical composition at the surface of a previously polished sample is not exactly that of the bulk, the crystallisation front is enriched or depleted in some components, leading to layer of uncrystallised material at the surface. This should lead to an area 1 covered by a layer of glass no more than a few nm thick. About 85% of the surface is attributed to area 1 and probably covered by this thin layer of glass.

Layer 1 cannot grow into the volume significantly due to the small crystal growth velocities in the [0001] direction. Just below layer 1, nucleation of differently oriented crystals takes place. This leads to the formation of spherulites which can also grow in the preferred directions *i.e.* that of the largest crystal growth velocity. Because of the neighboring spherulites, growth is mainly possible into the volume of the sample, leading to the semi-orientation of layer 2. The straight edge of layer 2 in Fig. 6 indicates that most spherulites contributing to this layer must be formed in a relatively short period of time. In layer 2, the orientation is hence achieved by kinetic selection.

By analogy, a surface layer with a thickness of 7–10  $\mu\text{m}$  has been shown by EBSD to be highly oriented during surface crystallisation of fresnoite.<sup>1</sup> In the case of fresnoite crystallisation, however, the layer immediately at the surface is not oriented in [001] but in [101] direction, *i.e.* is not oriented in the direction of the fastest growing direction. In both fresnoite and rhombohedral  $\text{BaAl}_2\text{B}_2\text{O}_7$  the initial oriented nucleation is stopped by the kinetic preference of faster growing directions.

## Experimental

A glass with the composition  $\text{BaO} \cdot \text{Al}_2\text{O}_3 \cdot \text{B}_2\text{O}_3$  was prepared from the raw materials  $\text{BaCO}_3$ ,  $\text{Al}(\text{OH})_3$  and  $\text{B}(\text{OH})_3$ . The compounds were mixed and then melted at 1480  $^{\circ}\text{C}$  using an



inductively heated furnace. The melt was stirred for 2 h and then cast on a copper block, quenched with a copper stamp and transferred to a furnace preheated to 620 °C, which was then switched off allowing the glass to cool.

A few mm of the quenched surface of the glass samples were ground away and manually polished with shrinking grain sizes down to 0.75 µm diamond suspension to eliminate any effects at the surface resulting from the quenching procedure. Crystallisation was achieved by heating the samples to 780 °C with a rate of 10 K min<sup>-1</sup>. This temperature was kept for 8 h, then the furnace was switched off. Subsequently, samples were polished using colloidal silica.

The surfaces of the crystallised glass-ceramics were directly characterised (without powdering) by X-ray diffraction (XRD, Siemens D5000) using CuK $\alpha$ -radiation. The samples were then cut perpendicular to the surface and subsequently polished as described above. All samples were carbon coated at about 10<sup>-3</sup> Pa to achieve conductivity.

The samples were further characterised using a scanning electron microscope Jeol JSM-7001F FEG-SEM equipped with a TSL Digiview 1913 EBSD-camera. OIM-scans were captured and evaluated using the software TSL OIM Data Collection 5.31 and TSL OIM Analysis 5. The OIM-scans were performed using a voltage of 20 kV and a current of about 2.40 nA. All OIM-maps presented are a combination of a grey scale IQ-map and a map imaging various orientations by different colors. Textures were calculated by harmonic series expansion (series rank: 16, Gaussian half-width: 5°, no sample symmetry).

## Conclusion

During crystallisation of a glass with the stoichiometry BaO·Al<sub>2</sub>O<sub>3</sub>·B<sub>2</sub>O<sub>3</sub> two layers of rhombohedral BaAl<sub>2</sub>B<sub>2</sub>O<sub>7</sub> with different orientations are formed at the surface. At the surface of the sample, a highly oriented layer (layer 1) of BaAl<sub>2</sub>B<sub>2</sub>O<sub>7</sub> with a thickness of up to 20 µm is found. The crystals within this layer are highly oriented with their crystallographic *c*-axes perpendicular to the surface. In a subsequent layer (layer 2), the crystals are oriented with their crystallographic *c*-axes parallel to the surface. While the primary layer 1 is caused by oriented nucleation at the surface, the orientation of the secondary layer is

caused by kinetic selection of spherulitic growth. About 85% of the surface is likely covered by a thin layer of glass of varying thickness.

The primary directions of growth for rhombohedral BaAl<sub>2</sub>B<sub>2</sub>O<sub>7</sub> are perpendicular to the *c*-axis of the crystals. Growth in the [0001]-direction is significantly slower. Crystallisation occurs as slabs.

## References

- 1 W. Wisniewski, M. Nagel, G. Völksch and C. Rüssel, *Cryst. Growth Des.*, 2010, **10**, 1414–1418.
- 2 A. Halliyal, A. S. Bhalla, R. E. Newnham and L. E. Cross, *J. Mater. Sci.*, 1981, **16**, 1023–1028.
- 3 A. Halliyal, A. S. Bhalla, R. E. Newnham and L. E. Cross, *Ferroelectrics*, 1981, **38**, 781–784.
- 4 N. Toyohara, Y. Benino, T. Fujiwara and T. Komatsu, *Solid State Commun.*, 2006, **140**, 299–303.
- 5 W. Wisniewski, M. Nagel, G. Völksch and C. Rüssel, *Cryst. Growth Des.*, 2010, **10**, 1939–1945.
- 6 R. Keding and C. Rüssel, *J. Non-Cryst. Solids*, 1997, **219**, 136–141.
- 7 R. Keding and C. Rüssel, *J. Non-Cryst. Solids*, 2000, **278**, 7–12.
- 8 R. Keding and C. Rüssel, *J. Mater. Sci.*, 2004, **39**, 1433–1435.
- 9 N. Ye, W. R. Zeng, B. C. Wu, X. Y. Huang and C. T. Chen, *Z. Kristallogr.*, 1998, **213**, 452, NCS.
- 10 K. H. Hübener, *Neues Jahrb. Mineral. Abh.*, 1970, **112**, 150–160.
- 11 D. Tauch and C. Rüssel, *J. Non-Cryst. Solids*, 2005, **351**, 2294–2298.
- 12 D. Tauch and C. Rüssel, *J. Non-Cryst. Solids*, 2005, **351**, 3483–3489.
- 13 C. Rüssel, D. Tauch, R. Garkova, S. Woltz and G. Völksch, *Phys. Chem. Glasses: Eur. J. Glass Sci. Technol. B*, 2006, **47**, 397–404.
- 14 R. Keding, D. Tauch and C. Rüssel, *Phys. Chem. Glasses: Eur. J. Glass Sci. Technol. B*, 2008, **49**, 174–176.
- 15 R. Müller, R. Naumann and S. Reinsch, *Thermochim. Acta*, 1996, **280** and **281**, 119.
- 16 D. Tauch, R. Keding and C. Rüssel, *Phys. Chem. Glasses: Eur. J. Glass Sci. Technol. B*, 2009, **50**, 389–394.
- 17 G. Völksch, R. Harizanova, C. Rüssel, S. Mitsche and P. Pöhl, *Glass Sci. Technol.*, 2004, **77C**, 438–441.
- 18 G. Völksch, W. Wisniewski and C. Rüssel, *J. Non-Cryst. Solids*, 2009, submitted.
- 19 R. Carl, G. Völksch and C. Rüssel, *Adv. Mater. Res.*, 2008, **39–40**, 387–390.
- 20 V. Randle, *J. Mater. Sci.*, 2009, **44**, 4211–4218.
- 21 A. J. Schwartz, M. Kumar and B. L. Adams, in *Electron Backscatter Diffraction in Materials Science*, Kluwer Academic/Plenum Publishers, New York, 2000.
- 22 K. Z. Baba-Kishi, *J. Mater. Sci.*, 2002, **37**, 1715–1746.
- 23 A. Karamanov and M. Pelino, *J. Eur. Ceram. Soc.*, 1999, **19**, 649–654.
- 24 I. Avramov and G. Völksch, *J. Non-Cryst. Solids*, 2002, **304**, 25–30.

### 3.5.

R. Carl, W. Wisniewski and C. Rüssel

#### **Reactions During Electrochemically Induced Nucleation of Mullite from a MgO/Al<sub>2</sub>O<sub>3</sub>/TiO<sub>2</sub>/SiO<sub>2</sub>/B<sub>2</sub>O<sub>3</sub>/CaO Melt**

Crystal Growth & Design, 2010, **10**, 3257-3262.

<http://pubs.acs.org/doi/abs/10.1021/cg100399t?prevSearch=%2528Wisniewski%2529%2BNOT%2B%255Batype%253A%2Bad%255D%2BNOT%2B%255Batype%253A%2Bacs-toc%255D&searchHistoryKey=>

**Reactions during Electrochemically Induced Nucleation of Mullite from a MgO/Al<sub>2</sub>O<sub>3</sub>/TiO<sub>2</sub>/SiO<sub>2</sub>/B<sub>2</sub>O<sub>3</sub>/CaO Melt**

Robert Carl, Wolfgang Wisniewski, and Christian Rüssel\*

*Otto-Schott-Institut, Jena University, Fraunhoferstrasse 6, 07743 Jena, Germany**Received March 25, 2010; Revised Manuscript Received May 19, 2010*

**ABSTRACT:** Glasses with the composition 52.6 SiO<sub>2</sub>·18.7 Al<sub>2</sub>O<sub>3</sub>·14.3 MgO·7.7 TiO<sub>2</sub>·4.7 B<sub>2</sub>O<sub>3</sub>·2.0 CaO were crystallized using electrochemically induced nucleation at temperatures from 1200 to 1400 °C. The crystals grew with their fastest growing axis pointing away from the surface of the electrode. At the cathode, Ti<sup>4+</sup> is reduced to Ti<sup>3+</sup>, which was proved by EPR and UV–vis–NIR spectroscopy. The silicate network is also reduced to elemental silicon to a small extent and forms an alloy with the platinum cathode. The higher coordination number of Ti<sup>3+</sup> should lead to a drop in viscosity due to its role as a glass modifier and, hence, fully explains the nucleation. The orientations of three neighboring crystals were analyzed by electron backscatter diffraction (EBSD).

**1. Introduction**

In the literature, different methods for the preparation of oriented glass-ceramics are described. Among these are the electrochemically induced nucleation,<sup>1–7</sup> extrusion of partly crystalline glass melts,<sup>8–11</sup> and surface crystallization,<sup>12,13</sup> often supported by thermal gradients<sup>14</sup> including laser induced crystallization.<sup>15–18</sup>

Electrochemically induced nucleation has already been described for the preparation of glass-ceramics in the systems BaO/TiO<sub>2</sub>/SiO<sub>2</sub>,<sup>5,7</sup> Li<sub>2</sub>O/Nb<sub>2</sub>O<sub>5</sub>/SiO<sub>2</sub>,<sup>19</sup> and Li<sub>2</sub>O/SiO<sub>2</sub>.<sup>20</sup> It might also enable the preparation of polar polycrystalline materials.

The principle of this method is as follows: In a platinum crucible containing the melt, a platinum wire is inserted. The temperature is high enough to avoid spontaneous nucleation while still being well below the liquidus temperature. A dc-current (some mA) is then applied between the crucible and the wire so that the crucible acts as the anode while the wire acts as the cathode. The resulting voltages are in the range from 1 to 2 V. As a result of the current flow, electrochemical reactions take place at the cathode as well as at the anode.

The anodic reaction in any case should be the oxidation of oxygen anions (i.e., oxygen in the oxidation state –II) to gaseous oxygen (O<sub>2</sub>). This results in the formation of small bubbles (diameter on the order of several hundreds of micrometers) near the wall of the crucible. The reaction taking place at the cathode depends on the glass system used. As a further result of the current flow, crystals start to grow from the cathode. This means that the current flow must have initiated nucleation. Due to the high temperatures supplied, the crystal growth velocity is fairly large. The crystals originate near the platinum wire and grow from the wire toward the crucible. In some cases, this results in highly oriented materials.<sup>3–7</sup> For the MgO/Al<sub>2</sub>O<sub>3</sub>/TiO<sub>2</sub>/SiO<sub>2</sub> and the MgO/Al<sub>2</sub>O<sub>3</sub>/TiO<sub>2</sub>/SiO<sub>2</sub>/CaO/B<sub>2</sub>O<sub>3</sub> systems, this has already been reported in refs 1 and 2.

Electron backscatter diffraction is a method only recently applied to glass ceramics<sup>21,22</sup> and based on the analysis of Kikuchi bands in a diffraction pattern obtained from a

crystalline surface in a scanning electron microscope (SEM).<sup>23</sup> This enables us to determine local crystal orientations, which are usually described by the Euler angles ( $\varphi_1$ ;  $\Phi$ ;  $\varphi_2$ ).<sup>23</sup> In the case of mullite,  $\varphi_1$  describes the rotation of the *c*-axis around the normal of the sample surface,  $\Phi$  describes the tilt of the *c*-axis from the normal of the surface, and  $\varphi_2$  describes the rotation around the *c*-axis.

Mullite has advantageous mechanical properties and a melting point of 1830–1890 °C.<sup>24</sup> A stoichiometric composition does not form a glass. Hence, the glass composition was modified by adding magnesium. These compositions are suitable to prepare glasses. An even better stability, i.e. a smaller tendency toward crystallization, was achieved by additionally adding boron and calcium oxide.

This paper provides a study on the reactions taking place during electrochemical nucleation in a glass melt with the mol % composition 52.6 SiO<sub>2</sub>·18.7 Al<sub>2</sub>O<sub>3</sub>·14.3 MgO·7.7 TiO<sub>2</sub>·4.7 B<sub>2</sub>O<sub>3</sub>·2.0 CaO and the orientations of grown crystals.

**2. Experimental Section**

The glass used in this study was prepared from powdered raw materials SiO<sub>2</sub> (quartz), Al(OH)<sub>3</sub> (hydrargillite), MgCO<sub>3</sub>·xH<sub>2</sub>O, TiO<sub>2</sub> (anatase), H<sub>3</sub>BO<sub>3</sub>, and CaCO<sub>3</sub>. The powders were mixed in a polymer bottle and afterward melted at 1600 °C for 8 h in a resistance heated MoSi<sub>2</sub> furnace. Then the glass was cast into water, dried, and remelted for an additional 8 h at 1600 °C. Finally, the glass melt was cast on a copper block and crushed with an iron mortar.

The glass was remelted in the inductively heated platinum crucible. The experimental setup used for the electrochemically induced nucleation of the glass melt is schematically shown in Figure 1.

The platinum crucible (i.d. = 50 mm), contacted with a platinum wire ( $\varnothing = 0.35$  mm), acts as the anode. Another platinum wire ( $\varnothing = 0.35$  mm) is inserted 10 mm into the glass melt and acts as cathode. Two corundum plates and some layers of ceramic fiber material were placed on top of the crucible to minimize the temperature gradient at the surface. A current generator (Knick DC-Calibrator J 152) was used to achieve the current flow through the glass melt. At first, the remelted glass was placed in the platinum crucible and remelted at a temperature of around 1520 °C for 60 min in order to remove crystals and nuclei. Then the temperature was reduced to the desired value (below the liquidus temperature), at which the electrochemically induced crystallization should start. After 9 min, a constant temperature was reached and the current (usually 5 mA) was switched on.

\*Corresponding author. Telephone: (0049) 03641 948501. Fax: (0049) 03641 948502. E-mail: ccr@uni-jena.de.

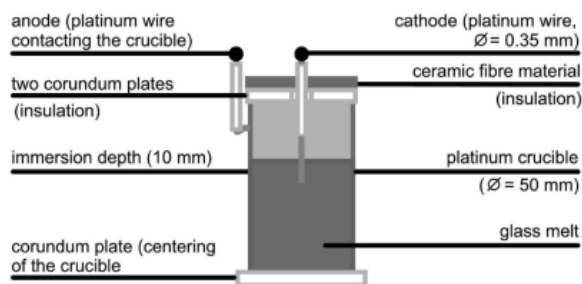


**Figure 1.** Experimental setup for electrochemically induced nucleation.

The current was applied to the melt for 5 min. After this period of time, the voltage between cathode and anode was measured (Gossen Metrawatt, Inc., Metrahit 22S CAT IV).

In most cases, the cathode remained in the melt for more than 30 min before removal (for a detailed description, see ref 2). As a result, crystals grew from the surface of the cathode toward the crucible wall. In some experiments, the platinum wire, acting as cathode, was drawn from the crucible together with the adherent crystals and the residual melt. These assemblies were put into an annealing furnace ( $T = 800\text{ }^{\circ}\text{C}$ ) to prevent cracking during cooling. As soon as the assemblies were inside the furnace, it was switched off and allowed to cool. In another series of experiments, the platinum wire was left inside the melt and the whole arrangement was cooled after a certain crystal growth time. At approximately  $1000\text{ }^{\circ}\text{C}$ , the cathode wire was cut close to the surface of the glass and the whole crucible was placed into a preheated annealing furnace ( $T = 800\text{ }^{\circ}\text{C}$ ), which was subsequently switched off and allowed to cool. After cooling, cylinders of about 20 mm in diameter were drilled out of the crucible including the cathode wire centered approximately in the middle. It should be noted that the temperature of  $800\text{ }^{\circ}\text{C}$  and the time schedule supplied do not result in noticeable further nucleation and crystal growth.

One of the assemblies described above was crushed by an iron mortar, and the glass near the platinum wire (diameter on the order of several hundreds of micrometers) was studied by EPR spectroscopy (ZWG, Inc., ERS 210, X-band: 9.44 GHz).

In order to study products formed at the cathode, a platinum wire covered with a thin layer of reduced glass (about  $50\text{ }\mu\text{m}$ ) was embedded in polymer. Then this assembly was cut, ground, and polished perpendicular to the immersion direction of the wire. This surface was investigated by scanning electron microscopy (SEM, Carl Zeiss, Inc., DSM 940A). Furthermore, thin sections of the sample (thickness =  $100 \pm 5\text{ }\mu\text{m}$ ) were investigated by photometric measurements in an optical microscope (Carl Zeiss, Inc., JENAPOL interphako in combination with Carl Zeiss, Inc., MPM 100). The measurements were performed using a filter transparent at 551 nm. The photometer measured the intensity of the transmitted light ( $I$ ) in comparison with that of the unreduced glass ( $I_0$ ). The diameter of the reduced area (dark coloration) was also measured on samples several millimeters thick via optical microscopy images (optical microscope Carl Zeiss, Inc., Technival) using the image analysis software Axio Vision 4.5 (Carl Zeiss, Inc.).

The samples were also studied using a scanning electron microscope (SEM) (Jeol JSM-7001F FEG-SEM equipped with a TSL Digiview 1913 EBSD-camera). Orientation image mapping-scans (OIM-scans) were captured and evaluated using the programs TSL OIM Data Collection 5.31 and TSL OIM Analysis 5. The OIM-scans were performed using a voltage of 20 kV and a current of about 2.40 nA.

### 3. Results

The produced glass showed a yellowish color and was transparent before crystallization. The effect of current on voltage at a temperature of  $1330\text{ }^{\circ}\text{C}$  and an immersion depth of 10 mm is shown in Figure 2. At a current of 0.5 mA, the voltage is 0.6 V and increases to a value of 0.88 V for a current

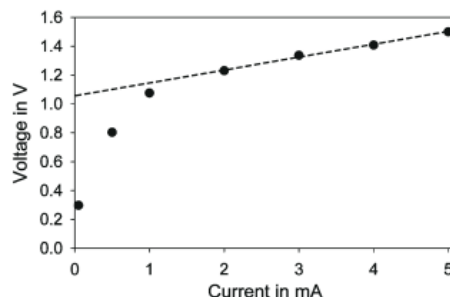


**Figure 2.** Dependency of the measured voltage with an immersion depth of 10 mm and a temperature of  $1330\text{ }^{\circ}\text{C}$  on the applied current.

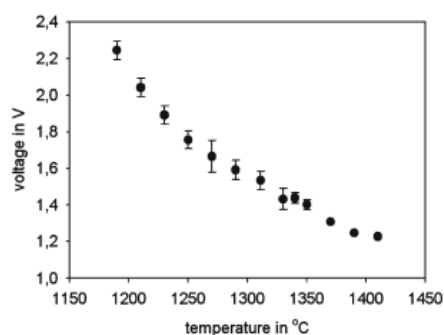


**Figure 3.** Dependency of the measured voltage with a current of 5 mA and an immersion depth (cathode) of 10 mm on the supplied temperature. The measurement was performed 5 min after attaching the current.

of 1 mA. At further increasing currents, an approximately linear increase of the voltage with current is observed until a voltage of 1.3 V is reached at 5 mA. The voltage was also affected by the immersion depth: while an increase of the immersion depth from 10 to 15 mm resulted in a decrease in voltage by 15%, a decrease of the immersion depth to 5 mm led to a voltage increase of 40%.

The effect of varying temperatures on the voltage is shown in Figure 3 (the error bar describes the mean deviations, when repeating the measurements). If both immersion depth and applied current are constant (5 mA), the voltage increases with a decreasing temperature of the melt. At  $1190\text{ }^{\circ}\text{C}$  the voltage is 2.25 V while it is 1.23 V at a temperature of  $1410\text{ }^{\circ}\text{C}$ . The voltage for 5 mA and  $1330\text{ }^{\circ}\text{C}$  in Figure 3 is 1.45 V, while it is 1.5 V in Figure 2. Regarding the different series of experiments (the temperature was kept constant in Figure 2 while the current was kept constant in Figure 3), the agreement is fairly good.

Figure 4 shows optical microscopy images of samples cut perpendicular and parallel to the inserted platinum wire (cathode). The crystals were grown at about  $1330\text{ }^{\circ}\text{C}$  and then transferred to a furnace preheated to  $800\text{ }^{\circ}\text{C}$ , which was then switched off, allowing the samples to cool. The crystal growth velocity determined from the length of the crystals and the growth time was  $280 \pm 30\text{ }\mu\text{m}/\text{min}$  at  $1330\text{ }^{\circ}\text{C}$ ; it dropped to  $100 \pm 10\text{ }\mu\text{m}/\text{min}$  at  $1430\text{ }^{\circ}\text{C}$ . A dark coloration around the platinum wire is observed. This coloration gets lighter with increasing distance from the surface of the cathode. These micrographs also show needle-like crystals which have their origin at the electrode surface. At some distance from the

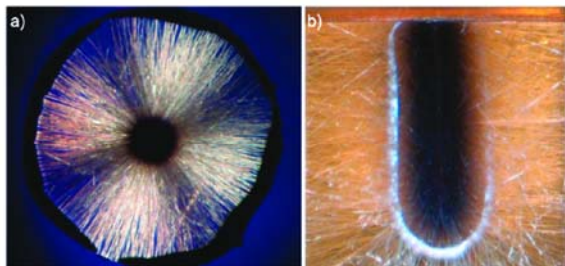


**Figure 4.** Samples cut perpendicular (a) and parallel (b) to the inserted cathode with the dark colored reduced area (cylindrical shape: diameter  $\approx 3$  mm, height  $\approx 10$  mm) surrounding the platinum wire (optical microscopy).

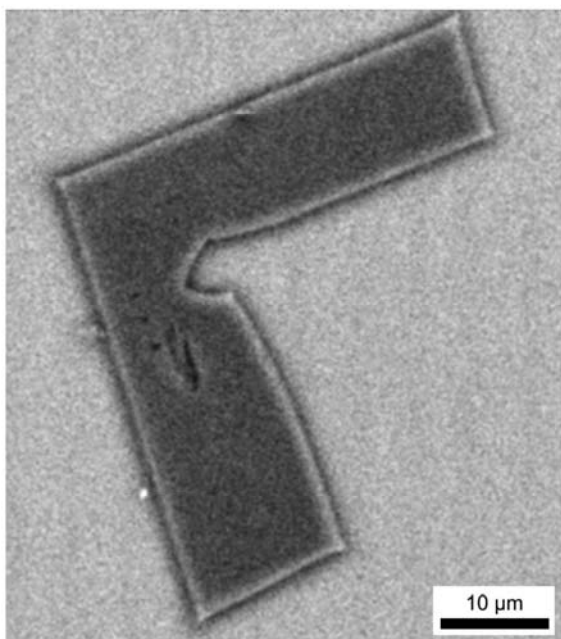


**Figure 5.** SEM micrograph of a crystal surrounded by the glassy matrix. Growth was achieved at 1330 °C, and the cut plane is parallel to the Pt-wire.

cathode, only needles that grow away from the surface of the cathode are found. The volume fraction of the crystalline phase is a few percent and decreases with increasing distance from the electrode. Without current flow, such structures are not formed.

Figure 5 shows an SEM-micrograph of a crystal surrounded by the glassy matrix in a cut plane parallel to the Pt-wire. The crystal exhibits a rectangular shape. The composition of the crystal as determined by energy dispersive X-ray spectroscopy (EDX) was  $\text{Al}_{4.65}\text{Ti}_{0.11}\text{Si}_{1.24}\text{O}_{9.675}$ . Significant changes in the chemical composition were not observed during the course of crystal growth. Figure 6 presents an EBSD pattern obtained from a crystal. Distinct Kikuchi bands are seen, proving the occurrence of lattice planes and, hence, a crystalline phase. The pattern can reliably be indexed as mullite. Figure 7 shows the orientation map of an OIM-scan performed over three neighboring crystals in the glassy matrix. The sample was cut approximately parallel to the platinum wire at a distance of about 5 mm. The patterns of all

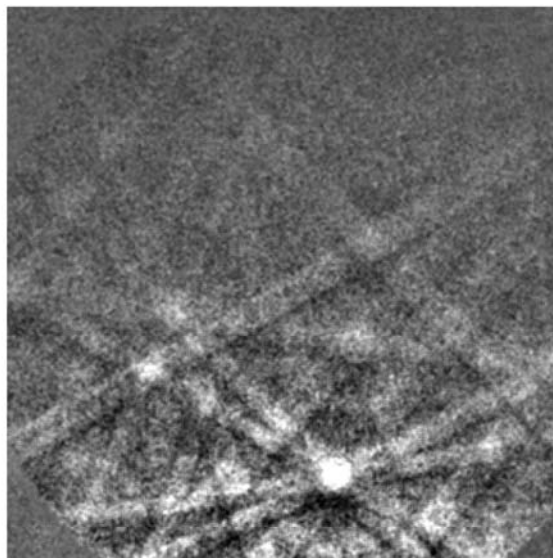


**Figure 6.** EBSD pattern obtained from crystal 1 in Figure 7.

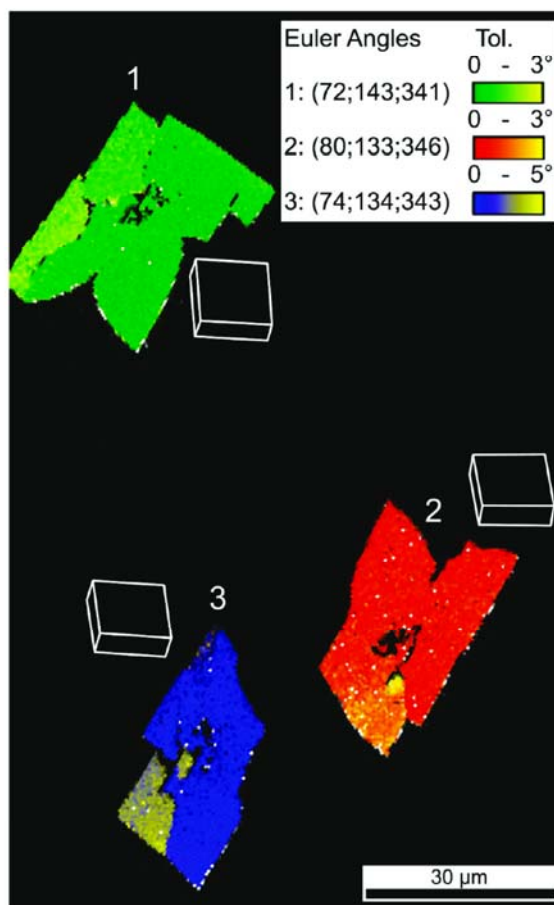


**Figure 7.** Orientation map of three mullite crystals embedded in a glassy matrix. The orientations of crystals 1–3 are described by the respective Euler angles and unit cells.

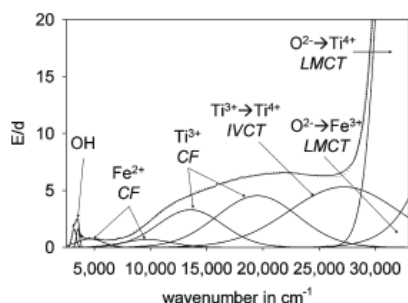


**Figure 8.** Optical absorption spectrum of the reduced glass. The spectrum is deconvoluted into seven bands of Gaussian shape. The superposition of these bands is given as the dotted line. (CF = crystal field transition band, IVCT = intervalence charge transfer, LMCT = ligand to metal charge transfer).

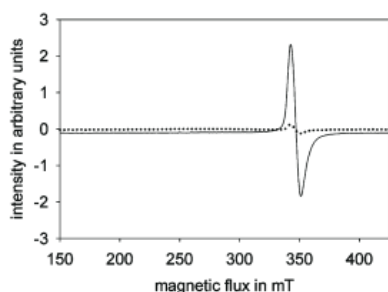


**Figure 9.** EPR spectra of the not reduced glass (dotted line) and the reduced (full line) glass-ceramic sample.

three crystals can reliably be indexed as mullite. The orientations of the crystals 1–3 differ slightly; the respective Euler angles of all three crystals are in agreement within  $\pm 7^\circ$ . The points attributed to the glass matrix have been excluded from the map and appear black.

Figure 8 shows an optical absorption spectrum of the darker section shown in Figure 4. The observed broad absorption band was deconvoluted into seven absorption bands, all attributed to crystal field ( $\text{Fe}^{2+}$ ,  $\text{Ti}^{3+}$ ) and charge transfer transitions ( $\text{Ti}^{3+} \rightarrow \text{Ti}^{4+}$ ,  $\text{O}^{2-} \rightarrow \text{Ti}^{4+}$ ,  $\text{O}^{2-} \rightarrow \text{Fe}^{3+}$ ). The absorption in the near IR range is caused by OH vibrations (at around  $3300 \text{ cm}^{-1}$ ). In summary, a broad absorption over the whole visible range ( $13000$  to  $25000 \text{ cm}^{-1}$ ) is observed until the strong absorption of the UV cut off is dominant (at around  $26500 \text{ cm}^{-1}$ ).

The EPR spectra of the dark colored (reduced) glass-ceramics and the yellowish colored raw glass are shown in Figure 9. The intensities of these two signals at around  $350 \text{ mT}$  differ significantly. The comparison of the intensities of both signals with a standard substance ( $\text{CuSO}_4 \cdot 5\text{H}_2\text{O}$ ) leads to the result that the number of the spins in the sample of the reduced glass (see full line) is 20 times larger than that in the not reduced glass (see dotted line). There is only one signal observed in each spectrum. The calculated  $g$ -value of this signal is 1.951.

In Figure 10, the radius of the colored region is shown as a function of the time the melt was held at a temperature of about  $1330^\circ\text{C}$ . It should be noted that the time of current flow and hence of electrolysis was 5 min in all cases before the wires were disconnected. Increasing radii are observed for increasing periods of time in Figure 10. The full line in Figure 10 was

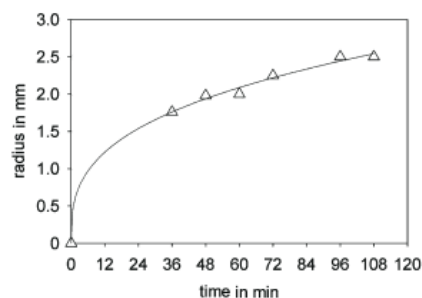


**Figure 10.** Dependency of the radius of the reduced area (dark) on the time. At  $t = 0$ , the current was supplied and at  $t = 5 \text{ min}$ , the current was switched off. The temperature was  $1330^\circ\text{C}$ ; full line  $r = (Dt)^{1/3}$  ( $D = 0.1495 \text{ mm}^3 \cdot \text{min}^{-1}$ ).

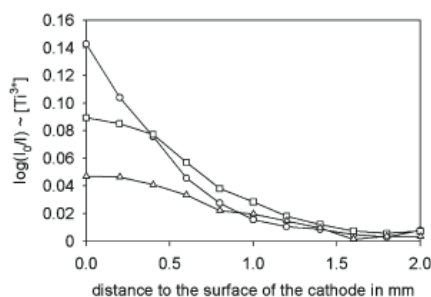


**Figure 11.**  $\text{Ti}^{3+}$  concentration profile after different periods of time at temperatures of about  $1330^\circ\text{C}$  (values result from photometric measurements of thin sections of glass surrounding the electrode).  $I_0$  = initial light intensity,  $I$  = transmitted light intensity;  $\log(I_0/I)$  stands for the extinction and is proportional to the  $\text{Ti}^{3+}$  concentration. In all cases, the current flow (5 mA) was maintained for 5 min. Time: (○) 48 min; (□) 72 min; (△) 96 min.

calculated from eq 1

$$r = \sqrt[3]{tD} \quad (1)$$

where  $r$  is the radius of the reduced region,  $t$  is the time after the current was supplied, and  $a (= 3)$  and  $D (= 0.1495 \text{ mm}^3 \cdot \text{min}^{-1})$  were fitted to the experimental data.

Using photometric measurements of thin sections ( $\sim 100 \mu\text{m}$  thick), the concentration profile of the  $\text{Ti}^{3+}$ -ions can be studied (see Figure 11). The  $\text{Ti}^{3+}$ -concentration is largest at the cathode surface after 48 min and decreases strongly with the distance from the electrode. After 72 min, the concentration at the electrode surface decreased notably, but it is larger at distances  $> 0.4 \text{ mm}$  than after 48 min. After 96 min, the concentration at the surface of the electrode is further decreased.

Figure 12 shows an SEM micrograph of a Pt-wire embedded in polymer and cut perpendicular to its length. The wire was used in an electrolysis experiment at  $1410^\circ\text{C}$  and 5 min electrolysis time (current = 5 mA). The wire remained inside the melt for approximately 36 min. After pulling the wire out of the melt, a thin glassy layer (about  $50 \mu\text{m}$ ) was adherent to the surface of the Pt-material. The outer dark regions in Figure 12 consist of the polymer the sample was embedded in. The dark gray ring is the glassy matrix, and the inner light area is the metal. Inside the light area, a dark gray ring as well as some inclusions of gray appearance is seen. Mainly Si was detected inside the inclusions using energy dispersive X-ray analysis. Other components of the glass such as  $\text{Al}_2\text{O}_3$  and CaO were not detected in the inclusions.

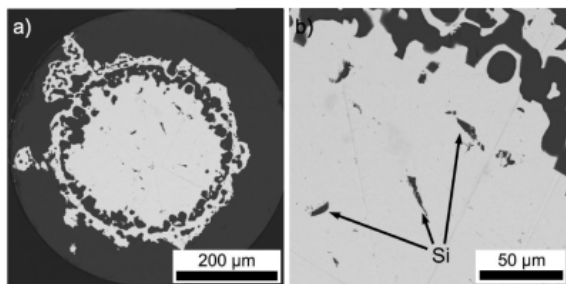


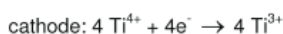
**Figure 12.** SEM micrographs of a cross section of the embedded platinum wire (a) and at higher magnification (b).

#### 4. Discussion

The transparent, yellowish glass produced without crystallization indicates that the initial ratio of  $Ti^{3+}/(Ti^{3+} + Ti^{4+})$  is negligibly small ( $\approx 0$ ). According to the results of EPR spectroscopy (see Figure 9), the black coloration of the reduced area is attributed to the formation of  $Ti^{3+}$ -ions, since the signal at around  $g = 1.951$  is typical for  $d^1$ -systems and close to other values reported in the literature for  $Ti^{3+}$ -ions containing glasses.<sup>25–27</sup> The intensity of this signal notably increases during the course of the reduction process and is much more intense than in the base glass.

The measured transmission spectrum (see Figure 8) can be simulated using nine absorption bands which are mainly dependent on the concentration of  $Ti^{3+}$ - and  $Ti^{4+}$ -ions. Besides the  $Ti^{3+}$  crystal field transitions with two absorption bands at around 13000 and 18000  $cm^{-1}$ ,<sup>25,27–31</sup> strong absorption bands in the UV region are observed. According to ref 25, they are attributed to charge transfer bands between  $Ti^{3+}$ - and  $Ti^{4+}$ -ions. The observed Fe–O bands are due to iron impurities. An ilmenite band (due to the metal to metal charge transfer band  $Fe^{2+}-Ti^{4+}$ ) with  $E/d$  of  $\approx 0.05$  is observed in the unreduced glass. Since the  $Ti^{3+}$ -bands are much more intense and occur in the same wavenumber range, they can no longer be seen in Figure 8. It should be noted that the deconvolution shown in Figure 8 is based on well-known absorption bands given in the literature.

Obviously a reduction of  $Ti^{4+}$  to  $Ti^{3+}$  takes place at the platinum wire (cathode).



Simultaneously, oxygen in the oxidation state –II is oxidized at the anode (the inner wall of the crucible) to gaseous oxygen. If the reduction of  $Ti^{4+}$  to  $Ti^{3+}$  were the only cathodic reaction, the quantity of  $Ti^{3+}$  should quantitatively be given by current and time according to Faraday's law. As shown in Figure 2, the potential increases steeply up to a current of 1 mA while larger currents lead to a further, moderate increase in voltage. Already at small currents, small quantities of  $Ti^{4+}$  are reduced until the  $[Ti^{3+}]/[Ti^{4+}]$  values at the electrode surface are in agreement with that according to the Nernst equation. At a certain fixed potential, the currents are then limited by diffusion or convection.

The linear part of the graph (at currents in the range from 2 to 5 mA) can be extrapolated to a current of 0 mA. This results in a decomposition voltage of around 0.8 V, which is in fairly good agreement with that previously reported in the literature<sup>32</sup> for other titanium containing silicate glasses. Assuming other cathodic reactions do not take place, a current of 5 mA supplied for 5 min according to Faraday's law results in a  $Ti^{3+}$  quantity of  $1.55 \times 10^{-5}$  mol. For a radius of the reduced area (see Figure 10) of 2 mm, an average of about 4% of the total  $Ti^{4+}$  should have been reduced to  $Ti^{3+}$ . Taking into account the concentration profile of  $Ti^{3+}$  as shown in Figure 9, the ratio  $[Ti^{3+}]/([Ti^{3+}] + [Ti^{4+}])$  at the electrode surface after 48 min should be around 0.3. It should be noted that  $Ti^{3+}$  is only essential for the initiation of nucleation and not for the following crystal growth presented in Figure 4.

With respect to the calculation of the line in Figure 10,  $a = 2$  is expected for linear (1-dimensional) diffusion. For a three-dimensional (radial) diffusion (toward a sphere),  $a = 3$  is expected. For the two-dimensional radial diffusion toward an infinitely long cylinder (e.g., a mullite needle), the solution of the attributed differential equation is not as simple and can only be done numerically ( $d$  is between 2.8 and 3 and depends on time). The approximation of  $a = 3$  in many cases is sufficient for a two-dimensional diffusion.

As shown in Figure 12, the platinum cathode notably changed during the electrolysis. Inside the platinum wire, inclusions are seen which possess a far smaller mean atomic weight than the platinum electrode. Inside these inclusions, mainly silicon was detected. It should hence be assumed that, at the surface of the electrode, also  $SiO_2$  is reduced to elemental silicon and forms a platinum/silicon alloy. According to the phase diagram, an eutectic is formed in the platinum-rich region, the attributed temperature is 847 °C, and the composition is  $Pt_{25}Si_7$ .<sup>33</sup> That means fairly low silicon concentrations ( $\sim 12$  mol % Si) in the binary system allow Si–Pt liquid phases to be formed at the temperatures applied during electrolysis. These Pt-phases do not contribute to the nucleation process because the metal itself is not the nucleating agent, as the metal electrode itself does not induce nucleation without current flow. The reduction of silicate melts to elemental silicon is also observed in other electrochemical investigations at platinum electrodes (see, e.g., refs 22 and 34). It can, hence, be concluded that at the temperatures and currents applied, not only  $Ti^{4+}$  is reduced to  $Ti^{3+}$ , but also the silicate network is reduced to elemental silicon, which forms a platinum/silicon alloy. This means that the  $Ti^{3+}$  concentration at the electrode surface should be smaller than that stated above.

Nevertheless, if  $Ti^{4+}$  is reduced to  $Ti^{3+}$ , the coordination number should change.  $Ti^{3+}$  is a larger cation ( $r = 0.69 \text{ \AA}$ ) than  $Ti^{4+}$  ( $r = 0.64 \text{ \AA}$ ) and, hence, should prefer a larger coordination number. Thus,  $Ti^{4+}$  can be considered as a network former, while  $Ti^{3+}$  acts as a network modifier. For example, for glasses in the  $BaO/TiO_2/TiO_3/SiO_2$  system, it has been shown that  $Ti^{3+}$  prefers the coordination numbers 5 and 6 while  $Ti^{4+}$  is incorporated in 4- and 5-fold coordination.<sup>35</sup> This also results in a decrease of the viscosity during the course of the reduction process (see, e.g., ref 9). Whenever viscosities of reduced titanium containing glasses were measured, the viscosity was smaller than that in oxidized glasses. It has also been reported in the literature that  $Ti^{3+}$  in the  $MgO/Al_2O_3/SiO_2$  system accelerates nucleation (see ref 36). Simultaneously,  $SiO_2$  is removed at the cathode by the reduction to

elemental silicon. This leads to depletion in SiO<sub>2</sub> near the cathode, which should result in a further decrease of viscosity.

According to the classical nucleation theory, decreased viscosities result in increased nucleation rates because the nucleation rate is proportional to the reciprocal viscosity. An alternative explanation is given by the percolation theory, which predicts an increase in the number of nonbridging oxygens if Ti<sup>3+</sup> (network modifier) is incorporated instead of Ti<sup>4+</sup> (network former).<sup>37–39</sup> This leads to an increase in the size of floppy regions. Nucleation then occurs if the size of a floppy region is larger than the size of a critical nucleus.<sup>39</sup>

Once the Ti<sup>3+</sup> concentration is large enough to initiate nucleation, further current flow is no longer necessary and the current can be switched off. During this time, the crystals grow to visible sizes, the [Ti<sup>3+</sup>] profile changes, and the concentration at the electrode decreases while it increases at some distance from the electrode. By analogy, the total radius of the reduced area increases also. Both are due to a simple diffusion process.

Since nucleation only takes place near the surface of the cathode, the formed structures are highly anisotropic. At some distance from the cathode, the crystals grow with their fastest growing axis, the crystallographic *c*-axis, away from the electrode. The crystals grow as needles, in contrast to the cases of other systems (e.g., the Ba<sub>2</sub>TiSi<sub>2</sub>O<sub>8</sub><sup>22</sup> or the LiNbO<sub>3</sub> system), which have been crystallized using electrochemically induced nucleation and show dendritic growth. As shown in Figure 7, neighboring crystals show approximately the same orientation; the crystals shown in this figure deviate from the orientation (75;138;344) by less than 7°. Hence, it should be assumed that neighboring crystals are not split off from the same crystals but nucleated at different sites and independent from one another.

Furthermore, the orientations within one crystal are very homogeneous despite the residual glassy phase and the cracks found in all crystals. The cracks therefore are probably not the result of tensions in the crystal but of the crystal growth or, however, of the applied cooling procedure. Orientations vary up to 5° within crystal 2 in Figure 7. In comparison to fresnoite crystals grown by electrochemically induced nucleation,<sup>22</sup> the crystal growth is not dendritic and the orientation by far not as pronounced.

### Conclusions

Glasses with the composition 52.6 SiO<sub>2</sub>·18.7 Al<sub>2</sub>O<sub>3</sub>·14.3 MgO·7.7 TiO<sub>2</sub>·4.7 B<sub>2</sub>O<sub>3</sub>·2.0 CaO were crystallized via electrochemically induced nucleation. At the cathode, Ti<sup>4+</sup> was reduced to Ti<sup>3+</sup>, while, at the anode, gaseous oxygen was formed. Simultaneously, the silicate network was reduced to elemental silicon, which formed an alloy with the platinum electrode. While increasing the current from 2 to 5 mA, the voltage increases linearly from 1.2 to 1.5 mV. The larger coordination number of Ti<sup>3+</sup> as well as the depletion of the melt with SiO<sub>2</sub> at the electrode surface should lead to decreasing viscosities. This results in nucleation and subsequent crystal growth. The formed Ti<sup>3+</sup> diffuses away from the electrode. The nucleation occurs solely near the electrode, i.e. in a small part of the volume. The mullite crystals grow away from this location along their fastest growing axis, the

crystallographic *c*-axis. Neighboring crystals show similar orientations. Orientation variations of up to 5° can occur within the cross section of a mullite crystal.

### References

- (1) von der Gönna, G.; Keding, R.; Rüssel, C. *J. Non-Cryst. Solids* **1999**, *243*, 109–115.
- (2) Carl, R.; Rüssel, C. *Phys. Chem. Glasses* **2007**, *48* (C1), 271–275.
- (3) Keding, R.; Carl, G.; Rüssel, C. *Glass Sci. Technol.* **2003**, *76*, 87–92.
- (4) Keding, R.; Rüssel, C. *J. Non-Cryst. Solids* **1997**, *219*, 136–141.
- (5) Keding, R.; Rüssel, C. *J. Non-Cryst. Solids* **2000**, *278*, 7–12.
- (6) Keding, R.; Stachel, D.; Rüssel, C. *J. Non-Cryst. Solids* **2001**, *283*, 137–143.
- (7) Keding, R.; Rüssel, C. *Ber. Bunsen-Ges. Phys. Chem.* **1997**, *100*, 1515–1518.
- (8) Habelitz, S.; Carl, G.; Rüssel, C.; Thiel, S.; Gerth, U.; Schnapp, J.-D.; Jordanov, A.; Knake, H. *J. Non-Cryst. Solids* **1997**, *220*, 291–298.
- (9) Moisesescu, C.; Jana, C.; Habelitz, S.; Carl, G.; Rüssel, C. *J. Non-Cryst. Solids* **1999**, *248*, 176–182.
- (10) Ashbee, K. H. G. *J. Mater. Sci.* **1975**, *10*, 911–917.
- (11) Atkinson, D. I. H.; McMillan, P. W. *J. Mater. Sci.* **1977**, *12*, 443–450.
- (12) Engel, K.; Frischat, G. H. *J. Non-Cryst. Solids* **1996**, *196*, 339–345.
- (13) Ding, Y.; Miura, Y.; Osaka, A. *J. Am. Ceram. Soc.* **1994**, *77*, 2905–2910.
- (14) Ochi, Y.; Meguro, T.; Kakegawa, K. *J. Eur. Ceram. Soc.* **2006**, *26*, 627–630.
- (15) Honma, T.; Benino, Y.; Fujiwara, T.; Komatsu, T. *Appl. Phys. Lett.* **2006**, *88*, 231105.
- (16) Hirose, K.; Honma, T.; Benino, Y.; Komatsu, T. *Solid State Ionics* **2007**, *178*, 801–807.
- (17) Oikawa, T.; Honma, T.; Komatsu, T. *Cryst. Res. Technol.* **2008**, *12*, 1253–1257.
- (18) Honma, T.; Komatsu, T. *Opt. Express* **2010**, *18*, 8019.
- (19) Gerth, K.; Keding, R.; Rüssel, C.; Schleevoigt, P.; Dunken, H. *Phys. Chem. Glasses* **1999**, *40*, 135–139.
- (20) Anspach, O.; Keding, R.; Rüssel, C. *J. Non-Cryst. Solids* **2005**, *351*, 656–662.
- (21) Wisniewski, W.; Nagel, M.; Völksch, G.; Rüssel, C. *Cryst. Growth Des.* **2010**, *10*, 1414–1418.
- (22) Wisniewski, W.; Nagel, M.; Völksch, G.; Rüssel, C. *Cryst. Growth Des.* **2010**, *10*, 1939–1945.
- (23) Schwartz, A. J.; Kumar, M.; Adams, B. L. In *Electron Backscatter Diffraction in Materials Science*; Kluwer Academic/Plenum Publishers: New York, 2000.
- (24) Pask, J. A. *J. Eur. Ceram. Soc.* **1996**, *15*, 101–108.
- (25) Arafa, S.; Bishay, A. *Phys. Chem. Glasses* **1970**, *11*, 75.
- (26) Bausá, L. E.; García Solé, J.; Durán, A.; Fernández Navarro, J. M. *J. Non-Cryst. Solids* **1991**, *127*, 267–272.
- (27) Schütz, A.; Ehrt, D.; Dubiel, M.; Yang, X.; Mosel, B.; Eckert, H. *Glass Sci. Technol.* **2004**, *77*, 295–305.
- (28) Burns, R. G. *Annu. Rev. Earth. Planet. Sci.* **1981**, *9*, 345–383.
- (29) Parkin, K. M.; Loeffler, B. M.; Burns, R. G. *Phys. Chem. Miner.* **1977**, *1*, 301–311.
- (30) Nolet, D. A. *J. Non-Cryst. Solids* **1980**, *37*, 99–110.
- (31) Rawal, B. S.; MacCrone, R. K. *J. Non-Cryst. Solids* **1978**, *28*, 337–345.
- (32) Keding, R.; Rüssel, C. *J. Non-Cryst. Solids* **2005**, *351*, 1441–1446.
- (33) Massara, R.; Fechotte, P. *J. Alloys Compd.* **1993**, *201*, 225–227.
- (34) Claussen, O.; Rüssel, C. *Glastech. Ber. Glass Sci. Technol.* **1996**, *69*, 95–100.
- (35) Schneider, M.; Richter, W.; Keding, R.; Rüssel, C. *J. Non-Cryst. Solids* **1998**, *226*, 273–280.
- (36) Vogel, W. In *Glas Chemie*, 3rd ed.; Springer Verlag: Berlin, 1992; p 360.
- (37) Thorpe, M. F. *J. Non-Cryst. Solids* **1983**, *57*, 355–370.
- (38) Phillips, J. C.; Thorpe, M. F. *Solid State Commun.* **1985**, *53*, 699–702.
- (39) Avramov, I.; Keding, R.; Rüssel, C. *J. Non-Cryst. Solids* **2000**, *272*, 147–153.



### 3.6.

W. Wisniewski, R. Carl, G. Völksch and C. Rüssel

#### **Mullite Needles Grown from a MgO/Al<sub>2</sub>O<sub>3</sub>/TiO<sub>2</sub>/SiO<sub>2</sub>/B<sub>2</sub>O<sub>3</sub>/CaO Glass Melt: Orientation and Diffusion Barriers**

Crystal Growth & Design, 2010, DOI: 10.1021/cg101402r.

<http://pubs.acs.org/doi/abs/10.1021/cg101402r?prevSearch=%2528W.%2BWisniewski%252C%2BR.%2BCarl%252C%2529%2BNOT%2B%255Batype%253A%2B%255D%2BNOT%2B%255Batype%253A%2Bacs-toc%255D&searchHistoryKey=>

**Mullite Needles Grown from a MgO/Al<sub>2</sub>O<sub>3</sub>/TiO<sub>2</sub>/SiO<sub>2</sub>/B<sub>2</sub>O<sub>3</sub>/CaO Glass Melt: Orientation and Diffusion Barriers**

Wolfgang Wisniewski,\* Robert Carl, Günter Völksch, and Christian Rüssel

*Otto-Schott-Institut, Jena University, Fraunhoferstr. 6, 07743 Jena**Received October 20, 2010; Revised Manuscript Received December 1, 2010*

**ABSTRACT:** Mullite crystals were grown from a MgO/Al<sub>2</sub>O<sub>3</sub>/TiO<sub>2</sub>/SiO<sub>2</sub>/B<sub>2</sub>O<sub>3</sub>/CaO glass melt via the method of electrochemically induced nucleation. Nucleation occurs near the cathode; the initially formed crystals are not oriented with their polar axes parallel to the electric field. The crystals showed needle-like shape. The crystal growth velocity shows a maximum at about 1260 °C and does not depend on time. The orientation distribution of the crystals in the resulting glass-ceramics was analyzed using electron backscatter diffraction (EBSD). During crystal growth, diffusion zones around the crystals are formed as shown by energy dispersive X-ray spectroscopy (EDX). These diffusion zones act as barriers which control the morphology of the formed mullite crystals.

**1. Introduction**

Mullite is the only thermodynamically stable phase solely consisting of Al<sub>2</sub>O<sub>3</sub> and SiO<sub>2</sub>. The chemical composition is not stoichiometric (Al<sub>(4+2x)</sub>Si<sub>(2-2x)</sub>O<sub>(10-x)</sub>) and is attributed to solid solutions with a composition between Al<sub>2</sub>SiO<sub>5</sub> ( $x = 0$ ) and *t*-Al<sub>2</sub>O<sub>3</sub> ( $x = 1$ ).<sup>1–7</sup> Furthermore, other metal oxides may be incorporated into the crystal lattice.<sup>8–14</sup> The mean chemical composition of the crystal phase in the samples studied in this paper was reported to be Al<sub>4.65</sub>Ti<sub>0.11</sub>Si<sub>1.24</sub>O<sub>9.675</sub><sup>14,15</sup> and did not depend on the temperature at which the crystals were grown, within the limits of error.<sup>14</sup>

The preparation of mullite crystals through a melting procedure is difficult due to the high melting temperature of mullite (1830–1890 °C).<sup>17</sup> Glass-ceramics containing mullite as a crystalline phase have frequently been described in the literature.<sup>13–16</sup> The system MgO/Al<sub>2</sub>O<sub>3</sub>/SiO<sub>2</sub> seems to be the most favorable for mullite crystallization and, depending on the composition, glass-ceramics with high mechanical strength, high hardness and high Young's modulus can be produced. This glass system tends to surface crystallization, however, after adding nucleating agents such as TiO<sub>2</sub> or ZrO<sub>2</sub>,<sup>18,19</sup> volume crystallization is observed. This leads to the initial precipitation of phases such as TiO<sub>2</sub> (rutile), ZrO<sub>2</sub>, or ZrTiO<sub>4</sub> during annealing.<sup>19</sup> In a subsequent step, other phases such as mullite, quartz or spinel are formed.<sup>16</sup>

Recently, electrochemically induced nucleation, a technique for the preparation of oriented glass-ceramics, has been applied to the preparation of mullite glass-ceramics.<sup>13–16</sup> During this process a platinum crucible with a melt of the respective composition is heated to a temperature above the liquidus temperature. A platinum wire is then inserted into the melt and the temperature is decreased below the liquidus temperature.<sup>13</sup> At this temperature, the nucleation rate is negligible while the crystal growth velocity is fairly high.<sup>16</sup> Then a dc-current is attached between the wire and the crucible resulting in a nucleation near the cathode and a subsequent growth of mullite crystals. The technique of

electrochemically induced nucleation has already been applied to a number of systems and enables the preparation of oriented glass-ceramics in many cases.<sup>13–16,20–24</sup> The mechanism of electrochemically induced nucleation involves a reduction process as a first step. As previously reported, in the case of the studied TiO<sub>2</sub>-containing melt this process is the reduction of Ti<sup>4+</sup> to Ti<sup>3+</sup>.<sup>13–16,20</sup> This leads to a drop in the viscosity and to a decrease in the network connectivity. Both effects lead to higher nucleation rates.<sup>25</sup>

The incorporation of TiO<sub>2</sub> into mullite crystals has been discussed<sup>14,26</sup> and the volume of the unit cell was found to increase with increasing Ti-concentration. Growth of mullite crystals is fastest parallel to the crystallographic *c*-axis, i. e. the [001]-direction of the unit cell,<sup>26</sup> as recently confirmed by electron backscatter diffraction (EBSD).<sup>14,15</sup> Short introductions to the method EBSD have been given in recent publications.<sup>27–30</sup>

This paper provides a study on the structures formed during electrochemically induced crystallization of mullite and focuses on diffusion profiles formed around the crystals during crystal growth.

**2. Experimental Procedure**

A glass with the mol % composition 52.6 SiO<sub>2</sub>/18.7 Al<sub>2</sub>O<sub>3</sub>/14.3 MgO/7.7 TiO<sub>2</sub>/4.7 B<sub>2</sub>O<sub>3</sub>/2.0 CaO was prepared from powdered raw materials SiO<sub>2</sub> (quartz), Al(OH)<sub>3</sub>, MgCO<sub>3</sub>·*x*H<sub>2</sub>O, TiO<sub>2</sub> (anatase), H<sub>3</sub>BO<sub>3</sub>, and CaCO<sub>3</sub>. The powders were mixed in a polymer bottle and melted in a resistance heated MoSi<sub>2</sub>-furnace at 1600 °C for 8 h. The resulting melt was cast into water, dried and remelted for additional 8 h at 1600 °C after which the melt was cast on a copper block and crushed by an iron mortar.

For the electrochemical nucleation the glass was remelted in the inductively heated platinum crucible ( $\varnothing = 50$  mm, depth 50 mm) which was contacted with a platinum wire ( $\varnothing = 0.35$  mm) to act as the anode. Another platinum wire ( $\varnothing = 0.35$  mm) was inserted about 10 mm into the glass melt to act as the cathode. To minimize the temperature gradient at the surface two corundum plates and some layers of a refractory insulating blanket of ceramic fibers were placed on top of the crucible. A current generator (Knick DC-Calibrator J 152) was used to achieve the current flow through the glass melt.

The melt was soaked at a temperature of 1520 °C for 60 min in order to remove crystals and nuclei. The temperature was then reduced below the liquidus temperature (around 1470 °C) to the

\*To whom correspondence should be addressed. Tel: (0049) 03641 948515. Fax: (0049) 03641 948502. E-mail: wolfgang.w@uni-jena.de.

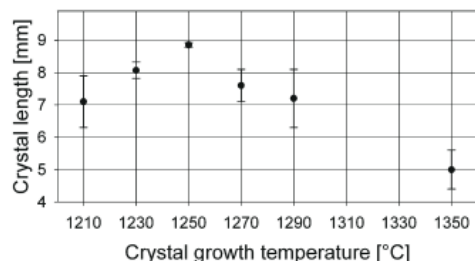


**Figure 1.** Lengths of the crystals after a crystal growth time of 36 min at varying temperatures.

desired value at which the electrochemically induced crystallization would begin. Various temperatures were applied to study crystal growth velocity at different temperatures. After 9 min, a constant temperature was reached respectively and the current (usually 5 mA) was switched on. The current was applied to the melt for 5 min after which it was turned off while the temperature remained constant for the respectively applied duration of crystal growth.

In most cases the cathode remained in the melt for more than 30 min at the respective temperatures before the furnace was switched off. As a result, crystals grew from the surface of the cathode toward the crucible wall. After switching the furnace off, the melt began to cool and the cathode wire was cut close to the surface of the glass at approximately 1000 °C. Then the whole crucible was placed into a preheated annealing furnace ( $T = 800$  °C) which was subsequently switched off and allowed to cool. After cooling, cylinders of about 20 mm in diameter were drilled out of the crucible including the cathode wire. Crystal lengths were obtained from polished surfaces of these cylindrical samples using optical microscopy (TECHNIVAL, Carl Zeiss Jena) and the image evaluation software Axio Vision 4.5 which was also utilized to determine the margin of error. The error bars are attributed to the standard deviation on the crystal lengths. For each sample at least 40 different crystals were measured.

The surfaces of samples analyzed by electron microscopy were ground and polished with shrinking grain sizes down to  $0.75 \mu\text{m}$  diamond suspension before analysis. A final finish of 30 min using colloidal silica was applied. The samples were characterized using a Jeol JSM-7001F Field Emission Gun–Scanning Electron Microscope (FEG-SEM) equipped with an analyzing system “EDAX Trident”. Because the raw EDX-data is rather diffuse, it was smoothed using the program SigmaPlot 11.0. (running average method: sampling proportion: 0.3, polynomial degree: 1). EBSD-scans were captured and evaluated using a TSL Digiview 1913 EBSD- Camera and the software TSL OIM Data Collection 5.31 and TSL OIM Analysis 5. In order to achieve a conductive surface, the samples were mounted using an Ag-paste and coated with a thin layer of carbon at about  $10^{-3}$  Pa. EDX-analyses were performed using an acceleration voltage of 15 kV.

### 3. Results

A current flow in titanium containing melts leads to the reduction of  $\text{Ti}^{4+}$  to  $\text{Ti}^{3+}$  as previously described.<sup>13–16,20</sup> Nucleation near the cathode occurs if a certain current density is supplied for a certain period of time until a sufficient concentration of  $\text{Ti}^{3+}$  has been formed during the reduction process. Crystal growth is strongly anisotropic and fastest in the direction of the crystallographic  $c$ -axis. The crystal growth velocities in this direction at different temperatures are presented in Figure 1. The length of a crystal in relation to the crystallization time at 1350 °C in the given experimental setup is plotted in Figure 2. It must be noted that the dotted line in Figure 2 represents a speculation on how the crystal length might develop during the first couple of minutes. Within the limits of error, the crystal growth velocity is not time-dependent in the measured duration of crystallization and amounts

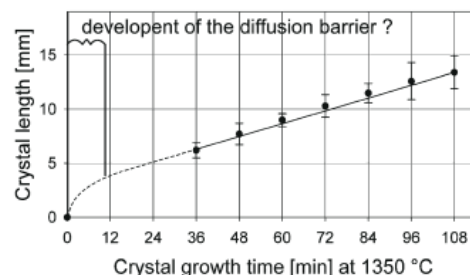


**Figure 2.** Lengths of the crystal after varying crystal growth times at 1350 °C. It must be noted that the dotted line is not according to a physical model but rather a reasonable and qualitative speculation of a possible development of crystal lengths immediately after nucleation.

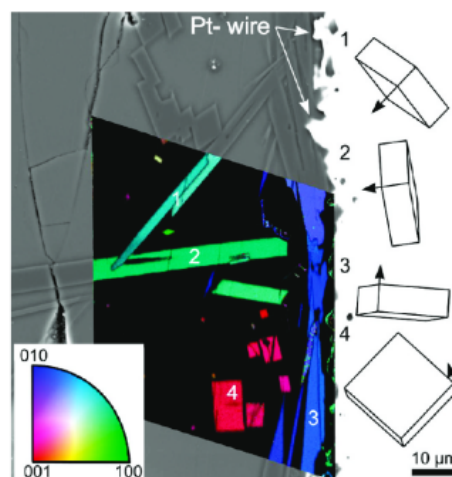
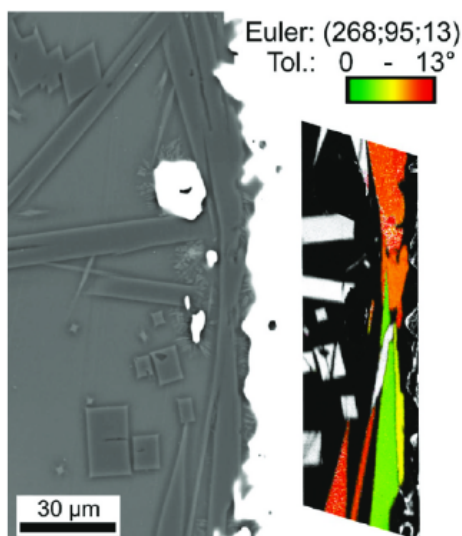


**Figure 3.** IPF-map of an EBSD-scan superimposed on an SEM-micrograph of the area. The orientations of the crystals 1–4 are indicated by the wire frames 1–4.

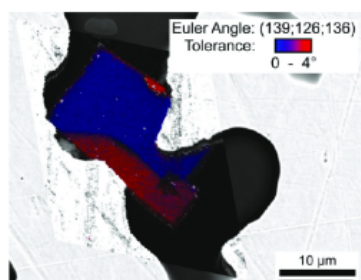
to about  $(2.44 \pm 0.12) \cdot 10^{-6} \text{ m} \cdot \text{s}^{-1}$  along the main growth direction at this temperature.

Figure 3 presents an inverse pole figure map (IPF-map)<sup>28–30</sup> of an EBSD-scan performed near the cathode and superimposed on an SEM-micrograph of the surrounding area. Crystal orientations are indicated by wire frames of the unit cells where the  $c$ -axes are marked by arrows. The orientations of the mullite crystals near the Pt-wire vary notably and range from perpendicular to the wire (crystal 2) over an angle of about  $45^\circ$  to the wire (crystal 1) to parallel to the wire (crystals 3 and 4). While crystal 3 is oriented parallel to the prepared sample surface, crystal 4 is aligned almost perpendicular. Figure 3 further shows the collision of the crystals 1 and 2. Only points with a confidence index (CI-value<sup>29</sup>) larger than 0.1 are presented in Figure 3, excluding the glass matrix (black). In order to homogenize the image, a neighbor CI-correlation cleanup was applied to the scan.

In the SEM-micrograph shown in Figure 4 the crystal denoted as crystal 3 in Figure 3 appears to be curved. A higher resolution of the orientations featured in an orientation map of the EBSD-scan in Figure 4 shows that the structure, which appears to be homogeneous in the SEM-micrograph, is in fact composed of various crystals with slightly varying orientations.



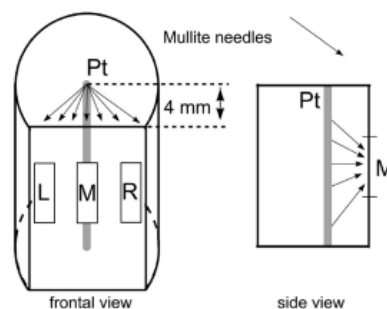
**Figure 4.** SEM-micrograph of crystals next to the Pt-wire (white) and part of an orientation map of a performed EBSD-scan.



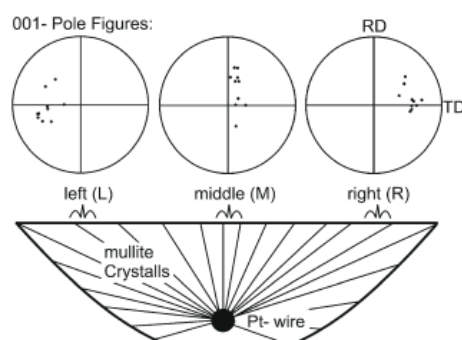
**Figure 5.** Orientation map of an EBSD-scan superimposed on an SEM-micrograph of the area where Pt appears bright white.

Figure 5 presents the orientation map of an EBSD-scan performed on a crystal grown within the corroded Pt-wire superimposed on an SEM-micrograph of the surrounding area. With respect to the orientation of the mullite crystal, two different parts can be distinguished: within the inner part of the crystal, the orientation is fairly homogeneous, while the orientations deviate up to  $4^\circ$  in the outer parts of the crystal. A slight deviation from the main orientation occurs at the upper edges of the crystal while the main area of deviation is in contact to the outcrop of left-hand side of the platinum phase (bright).

A sample was cut parallel to the cathode at a distance of about 4 mm from the Pt-wire (see Figure 6) and analyzed by EBSD. Because of the low volume fraction of mullite crystals, single EBSD-patterns were recorded from 10 crystals from different parts of the sample, schematically shown in Figure 6. Areas (about  $300 \times 900 \mu\text{m}^2$ ) at the left (L), middle (M) and right (R) parts of the sample, as outlined in Figure 6, were considered. The resulting orientations are presented in the 001-pole figures of Figure 7. While the middle area M shows a fairly broad distribution of orientations in the horizontal direction (usually called rolling direction RD) (about  $15 \pm 15^\circ$ ) and a less broad distribution in the vertical direction (usually called traverse direction TD) (about  $10 \pm 5^\circ$ ), both distributions are fairly broad in the areas L and R. To visualize



**Figure 6.** Sketch of the cut plane and the analyzed areas to the left (L), middle (M) and right (R) parts of the sample. The broad option of crystal orientations occurring in each area is indicated in the side view.



**Figure 7.** 001-Pole figures containing 10 points of 10 individual crystals found in the areas described by the presented scheme.

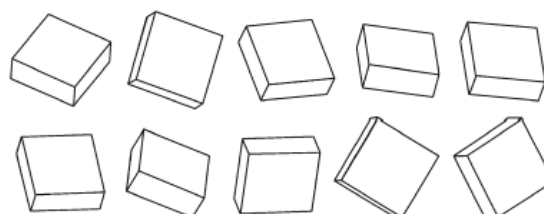
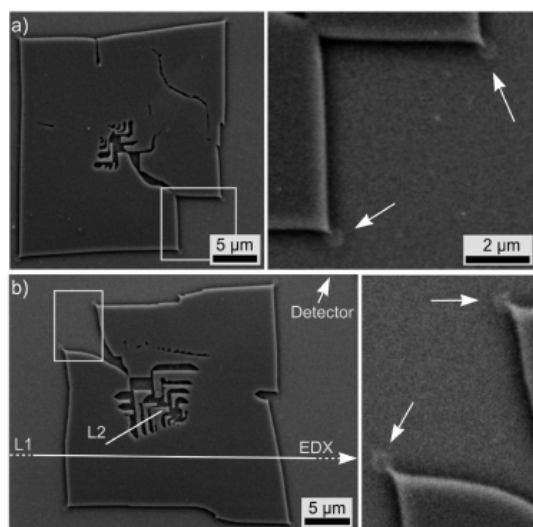


**Figure 8.** Wire frames of the mullite unit cell describing the orientations of the crystals represented by the 001-PF of the area M in Figure 7.

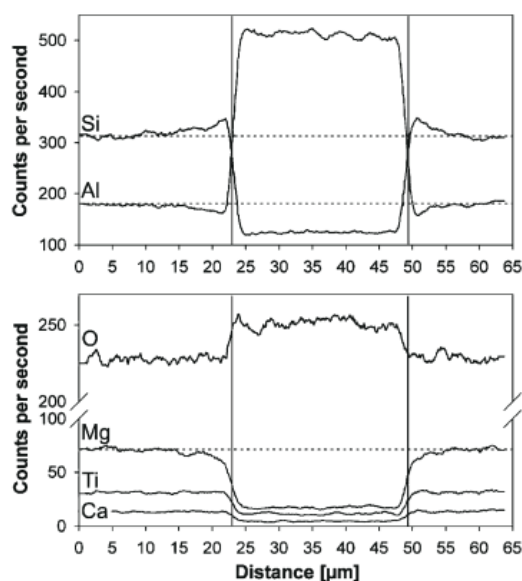
the rotation around the  $c$ -axes, wire frames of all the crystals analyzed in area M are presented in Figure 8. The diversity of the respective orientations is apparent.

Figure 9 shows two typical mullite crystals cut almost perpendicular to their  $c$ -axes. The inner parts of both crystals show irregularities. The tips of the crystals show very pronounced points with diffuse structures around them (see arrows in the enlarged areas of Figure 9). The data obtained from the EDX-linescans performed along the lines L1 and L2 displayed in Figure 9 are presented in Figure 10 and Figure 11. Analysis along the line L1 covers the solid crystal and large areas of glass matrix on either side. Figure 11 presents an EDX-line scan attributed to the Si and Al concentrations along the line L2 covering the irregularities within the crystal (see Figure 9).

In the SEM-micrographs of Figure 9a and b, a dark frame can clearly be discerned at the glass side of the glass/crystal



**Figure 9.** Two representative mullite crystals cut perpendicular to their main growth directions. The lines L1 and L2 indicate where EDX-linescans were performed.



**Figure 10.** Data of the EDX-linescan along L1 in Figure 9b featuring the elements Al and Si as well as O, Mg, Ca, and Ti.

interface while a bright frame is found at the crystal side of the interface. The widths of these frames were measured along the lines shown in Figure 12 (for Figure 9b) and are presented in Table 1. The AFM-scan presented in Figure 13 was performed on a crystal near those presented in Figure 9 to analyze the topography of the glass/crystal interface. While profile 1 describes the topography of the interface at the exterior of the crystal, profile 2 covers glass irregularities within the crystal.

#### 4. Discussion

As previously reported, the initial step of the crystallization process is the reduction of  $Ti^{4+}$  to  $Ti^{3+}$ . The oxidized species

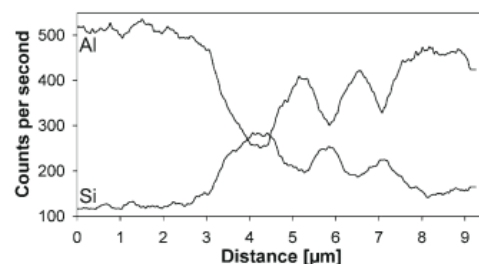


**Figure 11.** Data of the EDX-linescan along L2 in Figure 9b featuring the elements Al and Si. The line L2 crosses three inclusions within the crystal.

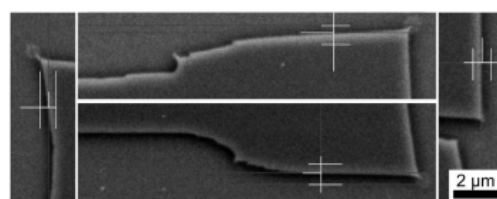


**Figure 12.** Dark and bright rings surrounding the crystal featured in Figure 9b. White lines have been inserted to indicate where widths presented in Table 1 were determined.

**Table 1.** Widths of the Dark and Bright Rings Surrounding the Crystals Presented in Figure 9a and b (For Higher Magnification of Figure 9b see Figure 12)

	edge	widths in nm		
		dark	bright	difference
Figure 9a	right	341	384	43
	left	384	384	0
	top	341	511	170
	bottom	384	469	85
Figure 9b	right	367	367	0
	left	326	367	41
	top	326	489	163
	bottom	489	367	122

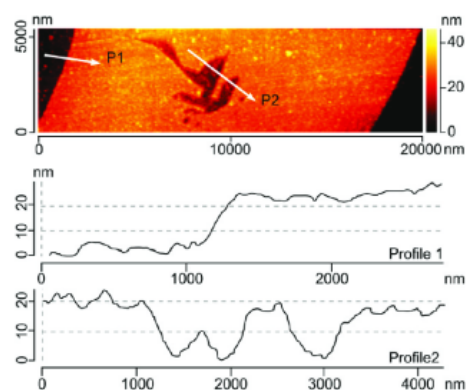


**Figure 13.** AFM-micrographs and topographical profiles along lines P1 and P2 performed on a crystal near those presented in Figure 9.

( $Ti^{4+}$ ) acts as network former and the reduced species ( $Ti^{3+}$ ) acts as network modifier. Thus the reduction process results in a decrease in viscosity and in the network connectivity.

This leads to higher nucleation rates and finally the crystallization is initiated.<sup>13–16,20</sup> The growth of the mullite crystals is anisotropic with growth predominantly occurring in the crystallographic [001]-direction parallel to the *c*-axis.<sup>14,15</sup> The maximum of the crystal growth velocity in Figure 1 indicates a normal type of temperature dependence for isothermal crystallization.<sup>31</sup> This means heating of the sample due to the crystallization enthalpy is not decisive for the crystallization process.

The time independent crystal growth velocity of about  $(2.44 \pm 0.12) 10^{-6} \text{ m} \cdot \text{s}^{-1}$  along the main growth direction at 1350 °C is fairly small in comparison e. g. to the crystal growth velocity of other crystal phases such as fresnoite in glasses.<sup>32</sup> If heating by the crystallization process were a significant factor, a saturation plateau would occur and the crystal growth velocity would be constant within a certain temperature range.<sup>31</sup>

It should be noted that the temperature in the given experimental arrangement is not perfectly constant. However, the crystal growth velocity as shown in Figure 2 does not depend on time throughout the duration of crystallization where experimental results were obtained and hence the effect of a temperature inhomogeneity should not affect the results notably. The speculation that a larger crystal growth velocity occurs during the early stage in Figure 2 is plausible for the following reasons: (i) the glass near the platinum wire is reduced ( $\text{Ti}^{4+}$  to  $\text{Ti}^{3+}$ ) and hence the viscosity is reduced near the cathode which should accelerate crystal growth and (ii) the diffusion barrier, described in Figure 10 and discussed later on, is not yet as pronounced as in a later state of crystal growth. After constant diffusion rates of the respective elements are reached at the glass/crystal interface, the velocity of crystal growth would become constant.

The initial step of the crystallization process, the reduction of  $\text{Ti}^{4+}$  to  $\text{Ti}^{3+}$ , was already described<sup>13–16,20</sup> and leads to nucleation near the electrode. There might be a tendency to the formation of a crystalline layer at the surface of the Pt-wire with the main growth direction parallel to the wire surface as indicated by crystal 3 in Figure 3. This was also observed during the electrochemically induced nucleation of fresnoite.<sup>28</sup> In any case, the range of crystal orientation in the immediate vicinity of the cathode presented in Figure 3 leads to the conclusion that the nuclei formed immediately after the current is attached are not oriented with their polar axes perpendicular to the surface of the platinum wire or parallel to the direction of current flow or the electric field. The two colliding crystals in Figure 3 possess notably different orientations and grew in different directions. Obviously, crystal 1 could not continue to grow and is stopped by crystal 2. The latter crystal is split and seems to have encased a notable amount of glassy phase. As the crystal needles were thinner at the time of collision, subsequent radial growth led to the immersion of the tip of crystal 1 within crystal 2. This is an example that needle shaped crystals may hinder each other during crystal growth if they are not oriented in the same direction. This phenomenon contributes to crystal selection and hence to the survival of mainly those crystals with a growth direction perpendicular to the electrode surface.

The crystal appearing to be curved in the SEM-micrograph of Figure 4 would be in contradiction to the needle shaped growth reported in previous papers<sup>13,14</sup> and raise questions toward the growth model presented in ref 13. The high resolution of orientations in the orientation map (see Figure 4) however shows that the “curved” structure is

actually composed of a number of adjacent, straight crystals. The straight, needlelike growth of mullite crystals<sup>13,14</sup> is thus still valid.

The mullite crystal in Figure 5 shows areas of changed crystal lattice. The main part of the changed lattice seems to radiate around the area of contact to the platinum phase (left). Possibly this deviation is a result of local stresses, caused e.g. by cooling the Pt-wire, or locally disturbed crystal growth. Deviations up to 5° have also been reported within the cross sections of mullite crystals surrounded only by the glass matrix.<sup>15</sup> In those cases, the orientational deviation should, however, be the result of a crystal collision or parts of the crystals breaking from the main body during cooling. Compressive stresses exerted on the crystals by the glass matrix cannot be the reason for the deviating areas of the crystals featured in ref 15 because then the orientational deviation would have to be homogeneous around the entire crystal and lead to images similar to the upper edges of the crystal in Figure 5. This, however, was not observed.<sup>15</sup> It can be concluded that the reason for crystal deviation presented here is different from the reason of crystal deviation in ref 15.

Figure 7 shows that an orientation of mullite crystals is observed at some distance from the platinum wire, although this orientation is not as pronounced as in the fresnoite system previously studied.<sup>27,28</sup> The orientation is only observed with respect to the *c*-axis of the crystals in a rather general way: the crystals show quite a broad distribution of angles toward the cathode as presented in Figures 7 and Figure 8. This is also illustrated in the side view displayed in Figure 6.

In comparison to the fresnoite system, mullite does not show classic dendritic growth and the volume fraction of mullite in the samples is much smaller. Subsequent to the nucleation process, the crystals grow mainly in the direction of the crystallographic *c*-axis. Since all nuclei are formed near the Pt-wire, the crystals grow away from the wire. This results in a certain degree of orientation. Since the volume fraction of the mullite crystals is fairly small, the mechanism that crystals hinder each other during further crystal growth is not as significant as in other studied systems.<sup>27–30</sup> Hence, not only those crystals will survive which are oriented exactly with their crystallographic *c*-axes perpendicular to the surface of the wire, but a fairly broad orientation distribution is observed.

The transversal sections of the crystals in Figure 9 show a rather square shape, which is in analogy to ref.<sup>16</sup> while in another previous study the majority of crystals showed an L-shaped morphology.<sup>14</sup> The results of the EDX-linescans of these crystals in Figure 10 and Figure 11 show that high concentrations of Al and O and low concentrations of Si, Mg, Ti and Ca are clearly observed inside the crystal when compared to the glass matrix. While the concentrations of the elements O, Mg, Ca, and Ti change continuously, Al and Si clearly show a counter movement before the respective major changes in concentration occur. This proves an enrichment of Si and an Al-deficiency at the glass side of the glass-crystal-interface. No comparable counter movement is observed at the crystal side of the interface. Hence, the chemical composition of the crystal does not change as a function of the distance from the glass/crystal interface. It should be noted that the latter, in principle, would be possible, because a solid solution with variable chemical composition is formed. The change in the Si and Al concentrations starts at a distance of about 7.5 μm from the crystal, while the changes in the O, Ca, and Ti concentrations are only apparent in the immediate vicinity of the interface. The change of the Mg concentration

begins at a larger distance from the interface than those of O, Ca, and Ti, but does not show a counter movement like those observed in Al and Si. The solid lines inserted in Figure 10 indicate the true glass-crystal-interface, while the dotted lines represent the mean values of Si, Al, and Mg in the glass matrix. It can be concluded from Figure 11 that the irregularities, also visible in refs 3–6, are residual glassy phase enclosed within the crystals.

Because of the diffusion barrier formed at the glass/crystal interface, a defect occurring during crystal growth cannot be compensated. While the defect can be surrounded by the growing crystal as it circumvents the diffusion barrier, the barrier itself cannot crystallize as it is depleted of the necessary elements, which cannot be supplied through diffusion once the irregularity is enclosed by the crystal. It can be suspected that crystal growth perpendicular to the main growth direction is dendritic-like, but significantly hindered by the diffusion barrier.

The dark frame observed in the SEM-micrographs in Figure 9 cannot be caused by the Al-deficiency around the crystal. If higher aluminum concentrations had such a significant impact on the SEM-signal, the bulk of the crystal would have to be much brighter than the glass matrix. The opposite is observed in Figure 9, confirming that the mean atomic number of the matrix (11.03) is slightly higher than that of the mullite crystal (10.84). Also, the area of deficiency extends about 7.5  $\mu\text{m}$  from the crystal while the dark frame is only 0.3  $\mu\text{m}$  wide.

Topographical contrast could lead to the frames, but if edge effects in the SEM were the reason for the frames they would have to appear asymmetrical due to the location of the Everhart-Thornley detector in the SEM, which is indicated in Figure 9 b). A closer look at these edges enables to detect a slight asymmetry of the frames as presented in Tab. 1: the difference between the widths of the dark and bright frames is significantly larger when comparing the top and bottom edges of the crystals than when comparing the right and left edges. A comparison of the edges of the crystal in Figure 9 b) is presented in Figure 12 where the difference between the top and bottom edge is apparent. The AFM-measurements performed on crystals near those in Figure 9 showed that the crystals are elevated from the matrix by about 20 nm (see Figure 13). This is also the case for the inclusions within the crystals (see profile 2 in Figure 13). Due to the existence of a physical edge and the detected asymmetry of the dark and bright frames in correlation with the positioning of the detector in the SEM it can be concluded that an edge effect in the SEM likely contributes to the bright frames. The dark ring however is not conclusively explained by the presented data.

Because of the size of the information volume contributing to EDX analyses, the change in the chemical composition at the glass/crystal interface does not appear discrete in the line scans displayed in Figures 10 and 11. In reality there is a discrete border glass/crystal and the Si-concentration is maximum at the interface and then decreases with increasing distance from the interface until the bulk concentration of the glass matrix is approached. The Al-concentration is minimum at the interface and then increases until the bulk concentration is reached. These concentration profiles can easily be explained assuming the diffusion of Al and Si as the rate determining steps of the crystal growth process. The fact that the diffusion profiles can be detected proves that they are fairly stable and do not rapidly disappear by further diffusion

processes in the glass melt. It should be noted that crystal growth in highly viscous media may generally be affected by the formation of barrier layers that hinder crystal growth. As recently shown, this also explains the formation of nano crystals, which do not notably grow with time.<sup>33–36</sup>

The reason for the occurrence of the diffusion profile is that the Si/Al-ratio is smaller in the crystal than in the glassy phase. Furthermore, the increased Si-concentration around the crystal should lead to an increase in viscosity, which further hinders the diffusion of Al toward the crystallization front of the growing crystal. Diffusion of Al toward the crystal would also be significantly faster at the tip of the crystal than along the side of a needle due to the much larger surface to crystal volume ratio per unit at the tip. It must be remembered that the crystallization occurs in a liquid with much higher viscosity, especially in comparison to metallic melts or aqueous or organic solutions. Hence transport by means of convection plays a far less important part.

If the needle-like growth of mullite had thermodynamic reasons, the surface energies in different crystallographic directions would have to be drastically different. Since surface energies of crystals in glassy melts are always within a very narrow range (maximum deviations: factor 2),<sup>37</sup> thermodynamic reasons (as supposed, e.g., in ref 26) are unlikely to lead to the observed needles. Hence the anisotropic growth should have kinetic reasons. The anisotropic growth of mullite should be the result of screw dislocations in the direction of the crystallographic *c*-axis and the described diffusion phenomena are likely to contribute to the needle like growth of the mullite crystals. The anisotropic growth of mullite is also reported to be enhanced by Ti-doping.<sup>26</sup>

## 5. Conclusions

Mullite needles grow subsequent to the electrochemically induced nucleation of mullite in a MgO/Al<sub>2</sub>O<sub>3</sub>/TiO<sub>2</sub>/SiO<sub>2</sub>/B<sub>2</sub>O<sub>3</sub>/CaO glass melt with a maximum growth rate at 1250 °C. After nucleation near the cathode, the crystals are not oriented with their polar axes parallel to the electric field. However, they grow away from the electrode and hence, in some distance, they are all oriented with their crystallographic *c*-axes in the direction toward the cathode. The growth velocity is relatively small, does not depend on time after an initial time span has elapsed, increases with temperature and, after a maximum is reached, decreases again. The observed mullite crystals form straight needles and may exhibit slight changes in the crystal orientation if stresses occur during growth or cooling.

The mullite needles encase residual glass phase and are surrounded by a diffusion zone about 7.5  $\mu\text{m}$  in thickness, which is depleted in Al and Mg and enriched in Si. This diffusion zone probably acts as diffusion barrier and significantly contributes to the extremely anisotropic crystal growth. An edge effect in the SEM likely contributes to the bright and dark frames observed around the crystals in the SEM-micrographs, however especially the dark ring remains to be fully explained.

## References

- (1) Cameron, W. E. *Am. Mineral.* **1977**, *62*, 747–755.
- (2) Subasri, R.; Roy, S.; Matusch, D.; Nafe, H.; Aldinger, F. *J. Am. Ceram. Soc.* **2005**, *88*, 1740–1746.
- (3) Angel, R. J.; McMullan, R. K.; Prewitt, C. T. *Am. Mineral.* **1991**, *76*, 332–342.

- (4) Rehak, P.; Kumath-Fandrei, G.; Losso, P.; Hildmann, B.; Schneider, H.; Jaeger, C. *Am. Mineral.* **1998**, *83*, 1266–1276.
- (5) Ruescher, C. H.; Schrader, G.; Goette, M. *J. Eur. Ceram. Soc.* **1996**, *16*, 169–175.
- (6) Merwin, L. H. *Phys. Chem. Min.* **1991**, *18*, 47–52.
- (7) Paulmann, C.; Ralunan, S. H.; Strothenk, S. *Phys. Chem. Miner.* **1994**, *21*, 546–554.
- (8) Rodriguez-Navarro, C.; Cultrone, G.; Sanchez-Navas, A.; Sebastian, E. *Am. Mineral.* **2003**, *88*, 713–724.
- (9) Wood, M. I.; Hess, P. C. *Contrib. Mineral. Petrol.* **1980**, *72*, 319.
- (10) Fischer, R. X.; Schneider, H.; Voll, D. *J. Eur. Ceram. Soc.* **1996**, *16*, 109–113.
- (11) Hwang, S. P.; Wu, J. M. *J. Am. Ceram. Soc.* **2001**, *84*, 1108–1112.
- (12) Torres, F. J.; Sola, E. R.; Alarcón, J. *J. Eur. Ceram. Soc.* **2006**, *26*, 2285–2292.
- (13) Carl, R.; Rüssel, C. *Eur. J. Glass Sci. Technol. B* **2007**, *48*, 271–275.
- (14) Carl, R.; Völksch, G.; Rüssel, C. *Adv. Mater. Res.* **2008**, *39–40*, 387–390.
- (15) Carl, R.; Wisniewski, W.; Rüssel, C. *Cryst. Growth Des.* **2010**, *10*, 3257–3262.
- (16) von der Gönna, G.; Keding, R.; Rüssel, C. *J. Non-Cryst. Solids* **1999**, *243*, 109–115.
- (17) Pask, J. A. *J. Eur. Ceram. Soc.* **1996**, *16*, 101–108.
- (18) Beall, G. H. *Annu. Rev. Mater. Sci.* **1992**, *22*, 91–119.
- (19) Höland, W.; Rheinberger, V.; Schweiger, M. *Phil. Trans. R. Soc. Lond. A* **2003**, *361*, 575–589.
- (20) Keding, R.; Rüssel, C. *Ber. Bunsenges. Phys. Chem.* **1997**, *100*, 1515–1518.
- (21) Keding, R.; Rüssel, C. *J. Mater. Sci.* **2004**, *39*, 1433–1435.
- (22) Keding, R.; Stachel, D.; Rüssel, C. *J. Non-Cryst. Solids* **2001**, *283*, 137–143.
- (23) Gerth, K.; Rüssel, C.; Keding, R.; Schleevoigt, P.; Dunken, H. *Phys. Chem. Glasses* **1999**, *40*, 135–139.
- (24) Anspach, O.; Keding, R.; Rüssel, C. *J. Non-Cryst. Solids* **2005**, *351*, 656–662.
- (25) Avramov, I.; Keding, R.; Rüssel, C. *J. Non-Cryst. Solids* **2000**, *272*, 147–153.
- (26) Hong, S. H.; Messing, G. I. *J. Am. Ceram. Soc.* **1998**, *81*, 1269–1277.
- (27) Wisniewski, W.; Nagel, M.; Völksch, G.; Rüssel, C. *Cryst. Growth Des.* **2010**, *10*, 4526–4530.
- (28) Wisniewski, W.; Nagel, M.; Völksch, G.; Rüssel, C. *Cryst. Growth Des.* **2010**, *10*, 1939–1945.
- (29) Wisniewski, W.; Nagel, M.; Völksch, G.; Rüssel, C. *Cryst. Growth Des.* **2010**, *10*, 1414–1418.
- (30) Wisniewski, W.; Zscheckel, T.; Völksch, G.; Rüssel, C. *CrystEngComm* **2010**, *12*, 3105–3111.
- (31) Gutzow, I.; Schmelzer, J. *The Vitreous State*; Springer: Berlin, 1995; p 350.
- (32) Cabral, A. A.; Fokin, V. M.; Zanutto, E. D.; Chinaglia, C. R. *J. Non-Cryst. Solids* **2003**, *330*, 174–186.
- (33) Rüssel, C. *Chem. Mater.* **2005**, *17*, 5843–5847.
- (34) Bocker, C.; Rüssel, C. *J. Europ. Ceram. Soc.* **2009**, *29*, 1221–1225.
- (35) Bhattacharya, S.; Bocker, C.; Heil, T.; Jinschek, J. R.; Höche, T.; Rüssel, C.; Kohl, H. *Nano Lett.* **2009**, *9*, 2493–2496.
- (36) Bhattachaya, S.; Höche, T.; Linschek, I.; Avramov, I.; Wurth, R.; Müller, M.; Rüssel, C. *Cryst. Growth Des.* **2010**, *10*, 379–385.
- (37) Scholze, H. *Glas—Natur, Struktur, Eigenschaften*, 3rd ed.; Springer: Berlin, 1988; p 56.



### 3.7.

W. Wisniewski, Ruzha Harizanova, Günter Völksch and Christian Rüssel

#### **Crystallisation of Iron Containing Glass-Ceramics and the Transformation of Hematite to Magnetite**

CrystEngComm, 2010, DOI:10.1039/C0CE00629G

<http://pubs.rsc.org/en/Content/ArticleLanding/2011/CE/C0CE00629G>

Cite this: DOI: 10.1039/c0ce00629g

www.rsc.org/crystengcomm

PAPER

## Crystallisation of iron containing glass–ceramics and the transformation of hematite to magnetite

Wolfgang Wisniewski,<sup>a\*</sup> Ruzha Harizanova,<sup>b</sup> Günter Völksch<sup>a</sup> and Christian Rüssel<sup>a</sup>

Received 10th September 2010, Accepted 8th December 2010

DOI: 10.1039/c0ce00629g

Crystallisation of a glass with the composition  $16\text{Na}_2\text{O} \cdot 10\text{CaO} \cdot 49\text{SiO}_2 \cdot 25\text{Fe}_2\text{O}_3$  led to the formation of hematite and magnetite crystals with various morphologies. Crystals containing both the hematite and the magnetite phases were detected and a strict orientation relationship between the phases is described. It is argued that hematite ( $\text{Fe}_2\text{O}_3$ ) is the phase primarily crystallised and magnetite ( $\text{Fe}_3\text{O}_4$ ) is the result of a phase transformation after the primary crystal growth. The main method of characterization was scanning electron microscopy (SEM) combined with electron backscatter diffraction (EBSD).

### Introduction

Glasses with a high concentration of polyvalent transition metal ions exhibit semiconducting electrical properties.<sup>1–5</sup> For example, glasses based on soda-lime glasses with  $\text{Fe}_2\text{O}_3$ -concentrations in the range from 5 to 30 mol% show an increase in the electric conductivity with increasing transition metal concentration. The crystallisation of semiconducting phases from these glasses may further increase the electrical conductivity.<sup>5–8</sup> In glasses with more than 20 mol%  $\text{Fe}_2\text{O}_3$  a notable increase in conductivity is observed<sup>5</sup> during crystallisation which has mainly been attributed to the formation of magnetite. The latter is *e.g.* observed in natural glasses (*e.g.* as dendrites)<sup>9</sup> as well as in various synthetic materials such as in coatings on glass substrates.<sup>10</sup> The crystallisation of magnetite may lead to the formation of interconnected semiconducting crystals which leads to a strong increase in the electric conductivity.<sup>5</sup> It was further reported that electrons are the main charge carriers and the conduction mechanism was described as a non-adiabatic, thermally activated hopping of small polarons.<sup>5</sup>

The occurrence of both magnetite and hematite within the same crystals in glass–ceramics was previously reported in one of the first publications applying electron backscatter diffraction (EBSD) to glass–ceramics.<sup>11</sup> In that case, however, magnetite did not occur in dendritic form. The crystal morphology was described as needles in which the [101]-direction of the cubic magnetite phase is oriented parallel to the needle axis.<sup>11</sup> The morphologies of hematite crystals may vary in a wide range as previously reported. Depending on the growth conditions, hematite crystals may possess dendritic shape, but snowflake-like

structures were observed as well, *e.g.* if hematite was grown via a hydrothermal method controlled by surfactants.<sup>12</sup>

The type and morphology of the crystals in iron containing glass–ceramics have been found to depend strongly on the thermal history of the samples rather than on the  $\text{Fe}_2\text{O}_3$ -concentration.<sup>13</sup> The thermal history also has a significant effect on the electrical conductivity as the crystals increase in size when cooled slowly. An increase of the Fe-concentration mainly results in a higher fraction of crystals.<sup>13</sup> Applying reducing conditions to the melt, *i.e.* increasing the  $\text{Fe}^{2+}/\text{Fe}^{3+}$  ratio, leads to higher viscosities, and thus reduces the tendency towards crystallisation. This might even enable the drawing of glass fibers, which would then also exhibit a certain electric conductivity.<sup>13</sup> In other systems, *e.g.* in highly iron doped borosilicate glasses, phase separation occurs during cooling. In the formed boron oxide- and iron oxide enriched droplets, nanoscale magnetite crystals could be identified.<sup>14</sup>

Pure magnetite shows a melting point of 1594 °C and can be synthesized *e.g.* by oxidizing metallic iron at high temperatures or by heating hematite in a reducing atmosphere.<sup>15</sup> According to the phase diagram, at a temperature of 1452 °C, magnetite may contain 30%  $\text{Fe}_2\text{O}_3$  which was reported to precipitate as hematite along the {111}-planes of the cubic magnetite during cooling.<sup>15</sup> This may also explain the occurrence of magnetite and hematite within the same minerals.

This paper provides a study on the morphology and phase composition of a soda-lime–silica glass containing 25 mol%  $\text{Fe}_2\text{O}_3$ . The main method used is scanning electron microscopy (SEM) combined with electron backscatter diffraction (EBSD).

### EBSD

Using an SEM equipped with an EBSD-unit combines the ability of studying the morphology and crystallographic relationships of a crystalline solid simultaneously.<sup>16–18</sup> Recent work on

<sup>a</sup>Otto-Schott-Institut, Jena University, Fraunhoferstr. 6, 07743 Jena, Germany. E-mail: wolfgang.w@uni-jena.de

<sup>b</sup>Physics Dept., University of Chemical Technology and Metallurgy, 8 Kl. Ohridski Blvd., 1756 Sofia, Bulgaria

automated phase and orientation mapping in transmission electron microscopy (TEM)<sup>19</sup> has enabled the analysis of structures too small to be characterised in an SEM. While a single EBSD-pattern provides information on the crystal at the spot where it was obtained, a grid of EBSD-patterns allows the description of the crystallographic properties of a microstructure and is referred to as Orientation Imaging Microscopy (OIM). The latter describes scanning a surface in a defined step size, collecting and indexing EBSD-patterns so that each point in an OIM-map represents the information of an indexed EBSD-pattern. Indexing a diffraction pattern is achieved by a voting system and characterized by a number of indexing parameters such as the image quality value (IQ), votes, the fit-factor, and the confidence index (CI) (see *e.g.* Schwartz *et al.*<sup>20</sup>).

The orientation of a crystal is usually defined by the three Euler angles  $\varphi_1$ ,  $\Phi$ , and  $\varphi_2$ . In the case of hematite for example,  $\varphi_1$  describes the rotation of the *c*-axis around the normal of the sample surface,  $\Phi$  describes the tilt of the *c*-axis from the normal of the surface, and  $\varphi_2$  describes the rotation around the *c*-axis.

The Inverse Pole Figure (IPF) is a reduction of the pole figure by symmetric operations usually to a unit triangle containing all orientations or their symmetric equivalents. The IPF-map is therefore a useful plot for an overview of all orientations appearing in a scan. Specific orientations in an OIM-scan can be visualized in an orientation map where individual orientations are defined by their Euler angles and a chosen tolerance for deviating orientations is permitted. The phase map of an OIM-scan simply attributes each occurring phase to a certain colour and does not provide information on the orientation of the crystals. More detailed introductions to EBSD and the effect of individual Euler angles of pole figures have previously been given.<sup>21,22</sup> A more detailed description of the method has been given in ref. 23. It must be noted that phase identification based solely on the comparison of indexed orientation solutions of an assortment of phases is rather questionable and very sensitive to the material files of the respective phases.

## Results and discussion

The glass transition temperature,  $T_g$ , of the melted glass was 510 °C as determined using differential thermo analysis (DTA). Two samples of this glass were annealed at 480 °C for 10 min (sample 1) and at 580 °C for 1 h (sample 2) resulting in crystal formation which was analyzed by XRD. The XRD-patterns of the unpowdered samples 1 and 2 in Fig. 1 show that both samples contain hematite (hematite a (JCPDS no. 01-089-0599) in sample 1 and hematite b (JCPDS no. 01-088-2359) in sample 2) as well as magnetite (JCPDS no. 01-087-0246). Slightly different lattice parameters are given for the files hematite a ( $a = 5.032 \text{ \AA}$ ,  $c = 13.733 \text{ \AA}$ ) and hematite b ( $a = 5.112 \text{ \AA}$ ,  $c = 13.820 \text{ \AA}$ ). Some peaks (of minor intensity) marked by “?” could not be identified. Sample 1 contains significantly more residual glass than sample 2 as indicated by the increased background signal in the first part of the pattern attributed to sample 1. In the SEM-micrograph of sample 1 (see Fig. 2), crystalline structures with different morphologies as well as a residual glassy phase are observed. Two fairly broad channels of a meandering structure with a thickness of about 50–70  $\mu\text{m}$  are visible. These structures are composed of numerous small crystals. Possibly these structures

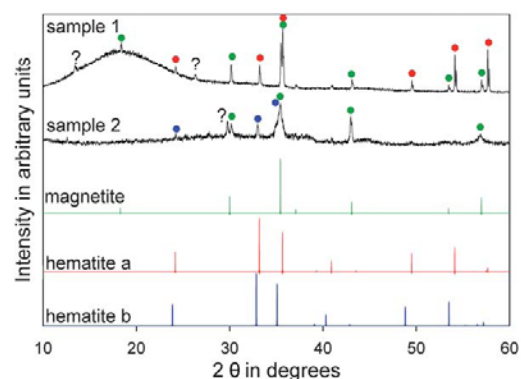


Fig. 1 XRD-patterns of samples 1 and 2. Both samples contain hematite as well as magnetite.

are formed by crystallisation around a stria, *i.e.* within a region with a chemical composition slightly different from that of other regions within sample 1. Long, thin crystals are observed in the vicinity of the meandering structure while most of the sample shows very small crystals resembling snowflake-like structures.

Using EBSD and XRD, both magnetite and hematite were identified in the sample: the core of the channel solely consists of hematite which is surrounded by a mantle of magnetite. This is indicated by the phase map of an OIM-scan superimposed on an SEM-micrograph of a part of the channel in Fig. 2. Magnetite crystals large enough to be analyzed by EBSD can only be found in this mantle while hematite occurs inside the channel and also in the form of larger crystals surrounding the channel outside the magnetite mantle.

Fig. 3 presents pole figures derived from the OIM-scan shown in Fig. 2: the (0001)-pole figure of the hematite phase and the (001)-pole figure of the magnetite phase comprehended in the scan. The hematite crystals are predominantly oriented with their *c*-axes perpendicular to the length of the channel while no preferential orientation could be described for the magnetite phase in the scan. The degree of orientation apparent in the channel is comparable to that observed in extruded glass-ceramics containing crystals of needle-like morphology.<sup>24,25</sup> Hence it is possible that mechanical stresses contributed to the formation of the crystals within the channel.

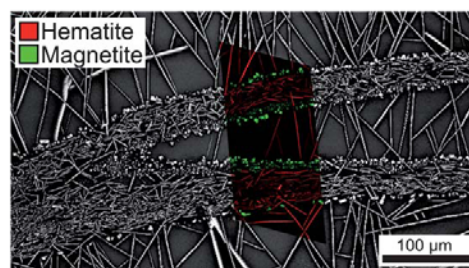


Fig. 2 SEM-micrograph of a channel of crystals overlaid by the phase map of an OIM-scan showing the locations of the hematite and magnetite phases.

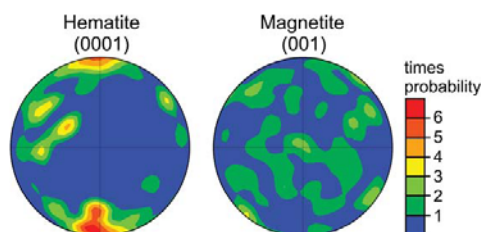


Fig. 3 Equal area pole figures of the hematite and magnetite phases comprehended by the OIM-scan presented in Fig. 2.

A closer look at the morphologies in Fig. 4 shows that magnetite usually occurs as block-like crystals near the channel. This is in contrast to the dendritic morphology of magnetite<sup>9,10</sup> observed in ref. 5. Hematite appears mainly as elongated crystals, however, hexagonal shapes can sometimes be found within the hematite region of the sample (see circle at the bottom left in Fig. 4).

The SEM-micrograph shown in Fig. 5 shows such a crystal with hexagonal shape surrounded by the crystals of elongated appearance, many of which show forked edges. The SEM-micrograph shown in Fig. 6 shows the same crystal in the context of the channel and outlines the area where an OIM-scan was performed. All crystals in the scan are attributed to the hematite phase. The orientations of the crystals 1–10 in the IPF-map of the OIM-scan shown in Fig. 6 are indicated by the wire frames 1–10 and clearly show that the *c*-axis of the large crystal (no. 1 in

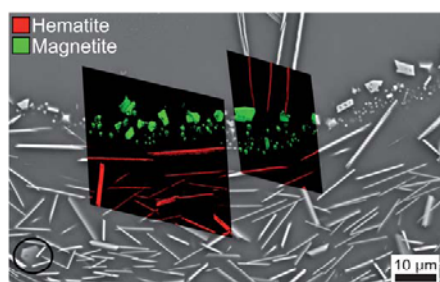


Fig. 4 Phase maps of two OIM-scans superimposed on an SEM-micrograph of a part of the channel illustrating the morphology of the hematite and magnetite phases.

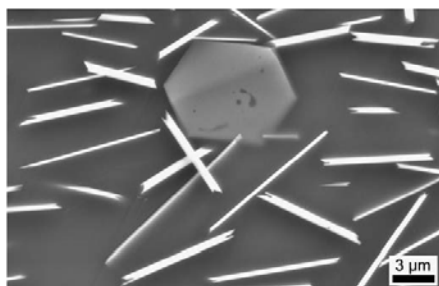


Fig. 5 SEM-micrograph showing crystals from the hematite region of the channel.

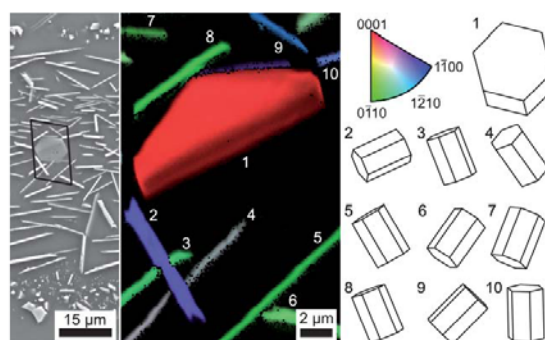


Fig. 6 SEM-micrograph outlining the area of a performed OIM-scan. The IPF-map of the scan is presented along with wire frames indicating the orientations of the crystals 1–10.

Fig. 6) is nearly perpendicular to the surface of the sample. The Euler angle triple attributed to crystal no. 1 is (287; 8; 328), indicating the *c*-axis is tilted by 8° from the surface normal. The orientation is very homogeneous throughout the entire visible part of the crystal as no point attributed to this crystal deviates more than 1° from the given orientation. The crystals whose *c*-axes are not oriented approximately perpendicular to the surface appear as crystals with the elongated shape.

It can thus be concluded that hematite preferably crystallises in a plate-like morphology under the given circumstances, as also described in ref. 13 and not in needle-like morphology (see ref. 11). Thus the crystal growth velocity is larger in the directions perpendicular to the *c*-axis than parallel to the *c*-axis. The dominant appearance of the hematite crystals as elongated shapes in the presented figures is thus only the result of the probability of cut planes through the plate-like crystals.

In the IPF-map shown in Fig. 6, the crystals no. 2–4 cross each other without any effect on their respective orientations. Constrictions due to crystals competing for chemical elements from the matrix or any other sign of interaction between the crystals comprehended in the scan are not visible in Fig. 5.

The hexagonally shaped crystal no. 1, cut almost perpendicular to the *c*-axis, is partially covered by a layer of glass. Only the uncovered part is visible in the OIM-scan due to the smaller information depth contributing to EBSD-patterns in comparison to the SEM-micrographs.<sup>20,24</sup> The SEM-micrograph was obtained using a voltage of 20 kV which was also applied for the OIM-scan.

Sample 2 was prepared by annealing at a higher temperature (580 °C) and for a longer period of time (1 h). In comparison to sample 1, it contains larger crystal structures throughout the volume composed of both hematite and magnetite as displayed in the phase maps presented in Fig. 7, 9 and 11. The main crystal covered by the OIM-scan in Fig. 7 is composed of both magnetite and hematite (see green and red areas, respectively). The two phases are adjacent to each other and the plane the crystal was cut in is almost perpendicular to the *c*-axis of the hematite phase, which means the [0001] direction of the hematite crystals is almost perpendicular to the presented micrograph (see also the wire frame in Fig. 8). Fig. 8 also shows an orientation map attributing colours to three defined orientations and the

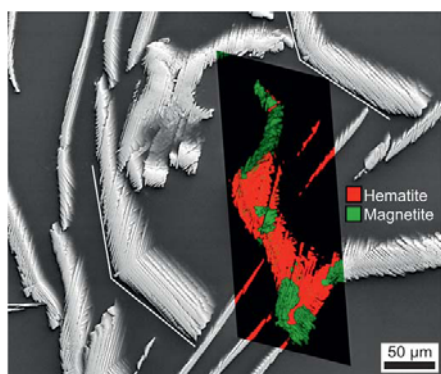


Fig. 7 Phase-map of an OIM-scan performed on a crystal containing both hematite and magnetite superimposed on an SEM-micrograph of the area.

(0001)-pole figures of the hematite phase as well as the (111)-pole figure of the magnetite phase comprehended in the scan.

In the orientation map of Fig. 8 the green areas are attributed to hematite, while blue and red areas represent orientations of the magnetite phase. A well pronounced maximum is observed at the centre of the (0001)-pole figure of the hematite phase, verifying the previously described orientation. It should be noted that all parts of the main crystal which are composed of hematite show the same orientation with a maximum deviation of  $\pm 15^\circ$ . The cubic magnetite phase is oriented with its [111] direction perpendicular to the sample surface. Altogether seven maxima are observed in the attributed (111)-pole figure. Besides the maximum in the centre, six further significant maxima occur with an angle between two neighbouring maxima of about  $60^\circ$ . In the (111)-pole figure of magnetite, oriented with the [111] direction perpendicular to the sample surface, three maxima are expected with an angle of  $120^\circ$  between them; additionally a maximum at the centre should be observed. It can thus be concluded that the observed maxima belong to two different magnetite orientations which are rotated by  $60^\circ$  around the [111] direction with respect

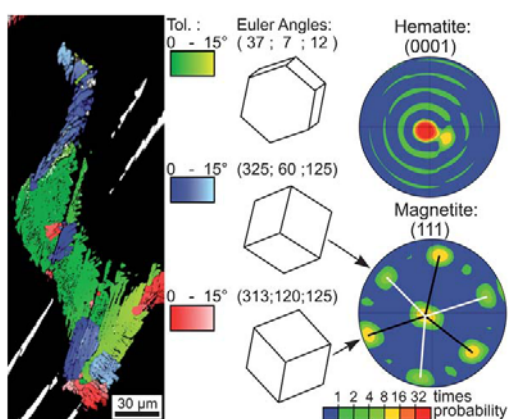


Fig. 8 Orientation map of the OIM-scan featured in Fig. 7. The defined orientations are visualized in the corresponding wire frames and the pole figures of the respective phases.

to each other (indicated by the black and white lines inserted into the (111)-pole figure in Fig. 8). These orientations are attributed to the red and blue regions in the orientation map shown in Fig. 8. Other orientations of magnetite do not occur in comparable probabilities.

The  $\Phi$ -values of the attributed Euler angle triples are  $60^\circ$  and  $120^\circ$  while the values for  $\varphi_1$  and  $\varphi_2$  are almost identical. The orientations of both phases deviate up to about  $15^\circ$  from the defined orientations within the crystal. By comparison, the smaller crystals observed in sample 1 do not deviate more than  $1^\circ$  (which is approximately the error limit for EBSD<sup>26</sup>) within the respective crystals.

By comparison, deviations up to  $\pm 5^\circ$  within one crystalline structure have recently been reported for the crystallisation of mullite.<sup>26</sup> For oriented fresnoite glass-ceramics, an extremely homogeneous orientation within large dendritic areas was observed.<sup>22,27</sup>

In the present case, the deviation of up to  $\pm 15^\circ$  indicates that the deviating orientations are the result of the phase transformation or, perhaps, stresses within the crystals, probably during cooling, contributed to the phase transformation. Although the small hematite crystals seem to grow around each other without significant interaction in Fig. 5 and 6, the much larger size of the crystals in sample 2 may lead to stresses during cooling due to a mismatch in the thermal expansion coefficients of hematite in different crystal directions, e.g. parallel or perpendicular to the *c*-axis.

In summary, the main hematite crystal in Fig. 7 is oriented with the [0001]-direction almost perpendicular to the surface of the sample and both magnetite orientations show the [111]-direction to be almost perpendicular to the surface of the sample as well. The [111]-direction in both magnetite orientations is thus parallel to the [0001]-direction of the hematite phase. These orientations in both the hematite and the magnetite lattices are perpendicular to the densely packed atomic layers which build the cubic and the hexagonal lattices.

The  $120^\circ$  angle observed in sample 1 at the edges of a solid hematite crystal grown without disturbance (see Fig. 5) can also be found in sample 2 if it is remembered that the hexagonal structures are not ideally parallel to the surface (see Fig. 7, white lines). This indicates that the primary crystal growth is similar in sample 1 and sample 2, allowing the conclusion that hematite crystals should have been formed first in sample 2 because of the  $120^\circ$  angles observed. This is further indicated by the plate-like morphology of the crystals in sample 2 and the hematite crystals in sample 1. Because the hexagonally shaped crystals in sample 1 were attributed to hematite, it can be concluded that hematite was the phase formed during the primary crystal formation and was partially transformed to magnetite later on. Furthermore magnetite occurs in only two different orientations which are rotated by  $60^\circ$  to each other. This cannot be explained if the magnetite phase would have formed first.

Then *a priori*, two mechanisms of phase transformation might occur: in the first possibility the magnetite crystals might grow epitaxially on the hematite crystals. Here two variations are possible in which the A-B layers of the hexagonal system continue to grow as A-B-C or, however, as A-C-B layers. This leads to two different orientations, both of which keep the [111]-direction constant while the structure is rotated by  $60^\circ$  around

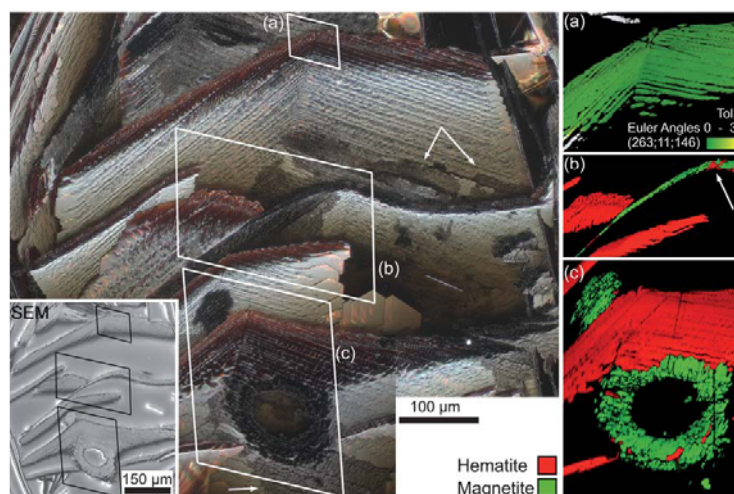


**Fig. 9** Optical micrograph (dark field) presenting crystals containing both hematite (red) and magnetite (black) in a glass matrix. The SEM-micrograph (bottom left) outlines which parts of the crystals constitute the surface of the sample. Frames where OIM-scans were performed are outlined in both images. OIM-map (a) is an orientation map while the maps (b) and (c) are phase maps identifying hematite and magnetite in the scanned areas.

the [111]-direction for the individual stacking orders. These are exactly the orientations observed in the pole figures shown in Fig. 9. It should be noted that parts of the lattice (those which are hematite) are enriched in oxygen.

The second possible mechanism is the subsequent transformation of hematite into magnetite. Here, the basic lattice composed of oxygen atoms must be rearranged from the hexagonal A-B stacking order into cubic A-B-C or A-C-B layers. This should also result in a [111]-direction of magnetite running parallel to the [0001]-direction of hematite. The morphology of the crystals should not change during this phase transformation.

Taking into account that magnetite occurs in two different orientations, the second mechanism seems to be more probable because otherwise hematite should occur in different orientations attributed to the four equivalent [111]-directions in the cubic lattice.

The annealing temperature of sample 2 is 100 K higher than that of sample 1. Since both annealing temperatures are not far above the glass transition temperature, the crystal growth velocity in sample 2 should be much larger. If the nucleation rate does not increase accordingly, this should favour the growth of larger crystals. In the case of lower annealing temperatures, a separate nucleation for hematite and magnetite crystals would be more likely.

The phase-map presented in Fig. 7 clearly shows that the transformation from hematite to magnetite does not follow a clear pattern, *e.g.* along crystal planes<sup>15</sup> or is initiated at the crystal/glass interface. At the bottom end of the main crystal, an inclusion of residual hematite is observed almost completely surrounded by magnetite. While the crystals in sample 1 show very compact features, the crystals in sample 2 show a secondary structure, visible for example in Fig. 7.

Fig. 9 shows a number of figures visualizing the morphology of crystals in sample 2 which are positioned almost parallel to the

sample surface. The main image is an optical reflection micrograph obtained in the dark field modus, which enables to see the crystal morphology under the glass surface due to the (limited) transparency of the glass. An SEM-micrograph of the displayed area is presented in the bottom left corner. Frames where OIM-scans were performed are outlined in both images. The distortion of the frames is a result of the geometrical arrangement of the EBSD-camera in the SEM. The SEM-micrograph (see bottom left) shows which fraction of the crystals is a part of the immediate surface of the sample. Crystalline areas which are part of the surface appear in a reddish colour and black, which according to literature<sup>15</sup> should correspond to hematite and magnetite, respectively. Under the surface, the crystals appear brighter, but darkened areas can be discerned (see arrows in the optical micrograph of Fig. 9).

At the edges of the crystals solid, hexagonal plates are observed, especially near the bottom right corner of frame (b) in Fig. 9. These are again comparable with the large crystal presented in Fig. 5, further ratifying the statement that initial crystallisation occurred as hematite. These hexagonal formations near frame (b) are about 9 µm below the surface of the sample (measured with the focus location of the optical microscope) and thus not visible in the SEM-micrograph.

The results of the OIM-scans are presented at the right side of Fig. 9: (a) is the orientation map of the hematite phase in the scan performed in the area of frame (a) which covers an area with a 120° angle of a crystalline formation. The crystal orientation, which indicates an angle of  $\Phi = 11^\circ$  between the *c*-axis of the crystal and the normal of the sample surface, is very homogeneous throughout the tip as the maximum deviation from the described orientation is less than 3° and twinning does not occur. This homogeneity is comparable to that observed in the compact crystals of sample 1 presented in Fig. 6, allowing the conclusion that the deviations of hematite in the vicinity of magnetite areas observed in Fig. 8 are caused by the phase transformation. While

the crystal is crystallographically homogeneous, however, the morphology of the crystals is not.

Scan (b) covers an area where red and black crystals appear in the optical micrograph. The corresponding phase map (b) verifies the correlation between the colour of the crystals and the phase, as even small pockets of hematite (see arrow in the phase map) appear reddish in the corresponding area of the optical micrograph.

The OIM-scan (c) (see Fig. 9, right) covers a hole in the featured crystal filled with amorphous material. As indicated by the corresponding phase map (c) the main crystal is composed of hematite while the crystals surrounding the hole mainly consist of magnetite. In the optical micrograph a part of the magnetite crystal is visible which cannot be observed in the SEM-micrograph, indicating that the magnetite area extends into the crystal below the polished surface. The fact that magnetite is observed under the surface of the sample proves that the occurrence of magnetite is not just an artefact of the polishing procedure (e.g. reduction of the surface). The enlarged segment of the optical micrograph in Fig. 10 clearly shows that the fish scale structure composed of stacked, hexagonal plates of hematite (left in Fig. 10) shows slightly changed morphology by the transformation to magnetite (dark area in Fig. 10).

The observed morphology might be interpreted as a compacted version of the snowflake-like growth of hematite reported in ref. 12 and would be composed of stacked hexagonal plates. This might indicate the dendritic growth of hematite instead of the individual smooth plates observed in sample 1.

Fig. 11 shows an area of sample 2 where most of the crystals were not cut perpendicular to the *c*-axis of the hematite phase. The morphology of the crystals is comparable to those observed in hematite in sample 1, again cementing the conclusion that hematite was the primary phase to crystallise. After the formation of the crystals hematite was again partially transformed to magnetite.

Looking at the (0001)-pole figure of hematite displayed in Fig. 11, it becomes clear that all hematite crystals in the scan show similar orientations except for the crystal at the bottom right corner which is oriented with the *c*-axis perpendicular to the surface as indicated by the wire frame in Fig. 11. The majority of the crystals can thus be assumed to consist of parallel plates.

The (001)-pole figure of the magnetite phase, which in this case gives clearer information than the (111)-pole figure, can again be

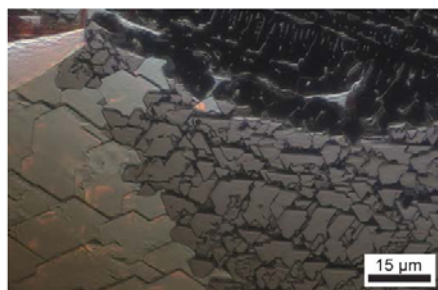


Fig. 10 Optical micrograph (dark field) of a part of the image given in Fig. 9 obtained with a higher magnification showing hematite (left) and magnetite (right).

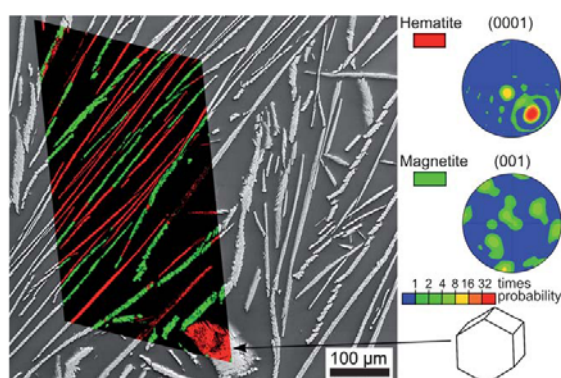


Fig. 11 Phase-map of an OIM-scan performed on a larger area containing many crystals composed of both hematite and magnetite superimposed on an SEM-micrograph of the area. The pole figures of the respective phases describe the orientation relationship between the existing phases.

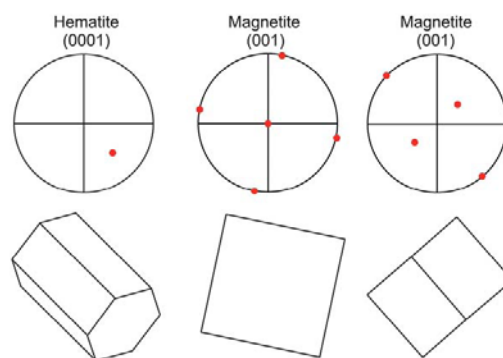


Fig. 12 Theoretical pole figures of the orientations featured in Fig. 11 and wire frames illustrating the respective orientations.

attributed to two orientations as indicated in Fig. 12. The (0001)-pole figure of the hematite phase in Fig. 12 also shows the main orientation assumed by the hematite crystals. This indicates that the orientation relation between hematite and magnetite as previously described in Fig. 8 is valid for all the crystals in the sample.

## Experimental

A glass with the composition  $16\text{Na}_2\text{O}\cdot 10\text{CaO}\cdot 49\text{SiO}_2\cdot 25\text{Fe}_2\text{O}_3$  was melted from a mixture of the reagent grade raw materials  $\text{Na}_2\text{CO}_3$ ,  $\text{CaCO}_3$ ,  $\text{SiO}_2$  and  $\text{Fe}_2\text{O}_3$  in a Pt-crucible at  $1400^\circ\text{C}$  and kept at this temperature for 5 h. The glass was then poured on a brass block and quenched with a brass stamp. Samples 1 and 2 were annealed at  $480^\circ\text{C}$  for 10 min and at  $580^\circ\text{C}$  for 1 h, respectively.

All sample surfaces were ground and polished with shrinking grain sizes down to  $0.75\ \mu\text{m}$  diamond suspension. A final finish of 30 min using colloidal silica was applied. The polished surfaces of the solid samples were directly analysed (without powdering) by X-ray diffraction (XRD, Siemens D5000) using  $\text{CuK}\alpha$ -radiation.

The samples were characterised using a scanning electron microscope Jeol JSM-7001F FEG-SEM equipped with an analysing system EDAX Trident. OIM-scans were captured and evaluated using a TSL Digiview 1913 EBSD-Camera and the software TSL OIM Data Collection 5.31 and TSL OIM Analysis 5. In order to achieve a conductive surface, the samples were mounted using an Ag-paste and coated with a thin layer of carbon at about  $10^{-3}$  Pa.

All data points in any presented map of an OIM-scan are attributed to a confidence index value larger than 0.100 to achieve reliability and exclude the glass matrix. All maps presented are a combination of a map describing phases or orientations through colours and the respective grayscale image quality map to further exclude residual glassy phase and enhance the visual image. All presented pole figures are equal area pole figures to avoid the distortion of a standard pole figure. Optical microscopy was performed using an Axio Imager Z1M with the software LSM5 Pascal.

## Conclusion

Two samples of the glass composition  $16\text{Na}_2\text{O} \cdot 10\text{CaO} \cdot 49\text{SiO}_2 \cdot 25\text{Fe}_2\text{O}_3$  were crystallised and investigated for phase evolution by the SEM-based methods EBSD and OIM-mapping as well as by XRD. In sample 1, crystallised at a lower temperature, hematite and magnetite crystals occur as separate phases with different morphologies. Hematite crystals show a plate-like shape while magnetite crystals show rather block-like shapes.

In sample 2, crystallised at a higher temperature, the crystal growth velocity is larger and hematite and magnetite both occur within one crystal. The crystallographic [0001]-direction of hematite is parallel to the [111]-direction of magnetite which occurs in only two orientations. The orientations differ only by a rotation around the [111]-direction of  $60^\circ$ . This orientation relationship occurs in all the crystals found in the sample. Both directions are perpendicular to the A–B–C and A–B layers forming the cubic and hexagonal lattice, respectively. Hematite crystallizes first and is then partially transformed to magnetite. The large crystals containing both hematite and magnetite incorporate deviations of the crystal orientation up to  $15^\circ$  while hematite areas without magnetite in the near vicinity only show deviations of up to  $3^\circ$  which is closer to the homogeneity observed in sample 1. The deviations of hematite are thus likely a result of the occurred phase transformation.

## References

- 1 M. H. Cohen, H. Fritzsche and S. R. Ovshinsky, *Phys. Rev. Lett.*, 1969, **22**, 1065–1068.
- 2 D. Adler, *J. Non-Cryst. Solids*, 1985, **73**, 205–214.
- 3 A. Mogus-Milankovic, D. E. Day, G. J. Long and G. K. Marasinghe, *Phys. Chem. Glasses*, 1996, **37**, 57–61.
- 4 H. H. Qiu, M. Kudo and H. Sakata, *Mater. Chem. Phys.*, 1997, **51**, 233–238.
- 5 R. Harizanova, R. Keding and C. Rüssel, *J. Non-Cryst. Solids*, 2008, **354**, 65–71.
- 6 A. C. M. Rodrigues, G. T. Niitsu, E. D. Zanotto, M. O. Prado and V. Fokin, *J. Non-Cryst. Solids*, 2007, **353**, 2237–2243.
- 7 M. M. El-Desoky, H. S. S. Zayed, F. A. Ibrahim and H. S. Ragab, *Phys. B*, 2009, **404**, 4125–4131.
- 8 H. Takahashi, T. Karasawa, T. Sakuma and J. E. Garbarczyk, *Solid State Ionics*, 2010, **181**, 27–32.
- 9 L. Szramek, J. E. Gardner and M. Hort, *Am. Mineral.*, 2010, **95**, 503–509.
- 10 W. Dong, X. Li, L. Shang, Y. Zheng, G. Wang and C. Li, *Nanotechnology*, 2009, **20**, 035601.
- 11 G. Völksch, R. Harizanova, C. Rüssel, S. Mitsche and P. Pölt, *Glass Sci. Technol.*, 2004, **77C**, 438–441.
- 12 S. Bharathi, D. Nataraj, M. Seetha, D. Mangalaraj, N. Ponpandian, Y. Masuda, K. Senthile and K. Yong, *CrystEngComm*, 2010, **12**, 373–382.
- 13 R. Harizanova, R. Keding, G. Völksch and C. Rüssel, *Phys. Chem. Glasses: Eur. J. Glass Sci. Technol., Part B*, 2008, **49**, 177–181.
- 14 R. Harizanova, G. Völksch and C. Rüssel, *J. Mater. Sci.*, 2010, **45**, 1350–1353.
- 15 W. A. Deer, R. A. Howie and J. Zussman, in *An Introduction to the Rock Forming Minerals*, Addison Wesley Longman Ltd., Harlow, UK, 1996.
- 16 J. A. Venables and C. J. Harland, *Philos. Mag.*, 1973, **27**, 1193–1200.
- 17 D. Dingley and V. Randle, *J. Mater. Sci.*, 1992, **27**, 4545–4566.
- 18 K. Z. Baba-Kishi, *J. Mater. Sci.*, 2002, **37**, 1715–1746.
- 19 E. F. Rauch, J. Portillo, S. Nicolopoulos, D. Bultreys, S. Rouvimov and P. Moeck, *Z. Kristallogr.*, 2010, **225**, 103–109.
- 20 A. J. Schwartz, M. Kumar and B. L. Adams, in *Electron Backscatter Diffraction in Materials Science*, Springer, New York, 2nd edn, 2009.
- 21 W. Wisniewski, T. Zschechel, G. Völksch and C. Rüssel, *CrystEngComm*, 2010, **12**, 3105–3111.
- 22 W. Wisniewski, M. Nagel, G. Völksch and C. Rüssel, *Cryst. Growth Des.*, 2010, **10**, 1939–1945.
- 23 L. Peruzzo, F. Fenzi and P. A. Vigato, *Archaeometry*, 2010, **53**, 178–193.
- 24 D. I. H. Atkinson and P. W. McMillan, *J. Mater. Sci.*, 1977, **12**, 443–450.
- 25 C. Moiescu, C. Jana, S. Habelitz, G. Carl and C. Rüssel, *J. Non-Cryst. Solids*, 1999, **248**, 176–182.
- 26 R. Carl, W. Wisniewski and C. Rüssel, *Cryst. Growth Des.*, 2010, **10**, 3257–3262.
- 27 W. Wisniewski, M. Nagel, G. Völksch and C. Rüssel, *Cryst. Growth Des.*, 2010, **10**, 4526–4530.



## 4. Summary

Structural investigations of glass-ceramic materials have been successfully performed using EBSD. Material files have been built and optimized for phases not contained in any accessible EBSD-database at the time (TSL and AMCS). It has been shown that the ability to measure crystal orientations locally can lead to new insights into crystal nucleation as well as crystal growth.

### 4.1 Surface crystallization

Analyzing surface crystallized samples of glass ceramic materials containing  $\text{Ba}_2\text{TiSi}_2\text{O}_8$ -type fresnoite and rhombohedral  $\text{BaAl}_2\text{B}_2\text{O}_7$ -crystals with EBSD lead to results contradicting the previously published views on surface nucleation and crystallization of glass. It was commonly assumed that oriented crystallized layers are the result of random nucleation occurring at or near the surface of the glass. The oriented crystal layers previously detected were assumed to be a result of the combination of asymmetric crystal growth and the kinetic selection of favorably oriented crystals. Generally the respectively described orientation was detected by the occurrence of enlarged peaks in the XRD-patterns (e. g. the (001) peak in fresnoite or the (003)-peak in glass-ceramics with  $\text{BaAl}_2\text{B}_2\text{O}_7$  -crystals), which also seemed to fit the appearance of the crystal morphology in SEM-micrographs.

In the case of  $\text{Ba}_2\text{TiSi}_2\text{O}_8$ -type fresnoite EBSD-scans of the only conductively coated surface showed that the preferred orientation of crystals at the immediate surface of the samples is with the [101]-direction perpendicular to the surface allowing the conclusion that oriented nucleation occurred instead of random nucleation as previously perceived.

The side view of these samples showed that the previously described orientation with the [001]-direction perpendicular to the surface occurs in a layer from about 7  $\mu\text{m}$  beneath the surface until further growth is hindered by crystals resulting from volume crystallization. This second layer of surface crystallization is the result of a kinetic selection of the oriented surface nucleation due to the preferred crystal growth of fresnoite in the [001]-direction.

In the case of glass-ceramics containing rhombohedral  $\text{BaAl}_2\text{B}_2\text{O}_7$ -crystals, a thick layer of over 500  $\mu\text{m}$  of oriented surface crystallization is visible in both optical and SEM-micrographs. A strong [001] orientation of surface crystallized materials was observed in both XRD and EBSD meaning the c-axis is oriented perpendicular to the sample surface. While the previous conception was that this [001] orientation occurs within the entire 500  $\mu\text{m}$  thick

layer visible in micrographs, EBSD-analysis showed that most of this layer is actually composed of crystals oriented with their c-axes more or less parallel to the surface while the [001] orientation is limited to a layer only about 20  $\mu\text{m}$  thick at the immediate surface. It could also be deduced that the crystal growth velocity of rhombohedral  $\text{BaAl}_2\text{B}_2\text{O}_7$ -crystals is larger in directions perpendicular to the c-axis than parallel to the c-axis.

Thus a two layer structure of the surface crystallization was again detected in which oriented nucleation occurs at the immediate surface and forms a thin layer of crystals, while a second layer of oriented crystals following the fastest direction of crystal growth forms the main part of the surface crystallized layer visible in cross sectional micrographs.

Due to the localized degradation of EBSD-patterns occurring during EBSD-scans of the untreated surface but not on polished surfaces, it was concluded that only part of the crystals are exposed at the surface while most of the surface crystals are covered by a very thin layer of glass. A detailed study of this effect has been submitted recently [60].

This was explained by nucleation occurring immediately at the surface. The direction of largest crystal growth velocity is the direction parallel to the surface. Since the surface is not ideally flat, the crystallization front dives beneath the surface due to the fastest direction of growth deviating from the surface at some point. The uneven surface is a result of the occurring crystallization which is accompanied by a volume expansion. The degree of surface coverage was quantified.

Oriented nucleation at the surface, itself an example of thermodynamically controlled orientation of crystals in glass-ceramics, was thus proven to exist and described in the cases of both surface crystallized  $\text{Ba}_2\text{TiSi}_2\text{O}_8$ -type fresnoite and rhombohedral  $\text{BaAl}_2\text{B}_2\text{O}_7$ . Previous models of the crystal orientation and the formation of the orientation of these phases were found to be incorrect and alternatives were described. In both cases, the orientation of the thermodynamically controlled, topmost crystal layers resulting from the oriented nucleation at the surface is changed to kinetically preferred orientations within a couple of micrometers from the surface.

It can thus be concluded that kinetic selection is more important for achieving oriented crystal structures of significant thickness than oriented nucleation due to thermodynamic reasons as the kinetically preferred orientation will always prevail over the latter as crystal growth proceeds and the crystals have contact to one another and thus hinder each other during crystal growth.

## 4.2. Electrochemically Induced Nucleation/ Crystallization

The EBSD-analysis of dendritic  $\text{Ba}_2\text{TiSi}_2\text{O}_8$ -type fresnoite grown via electrochemically induced nucleation led to the detection of a small number of slightly deviating crystals within the otherwise extremely homogeneously oriented dendrites. These deviating crystals are probably the result of dendritic fragmentation. The number of deviating crystals decreases with increasing distance from the area of nucleation near the Pt-wire where crystal orientation was found to be diverse, indicating randomly oriented nucleation. It was also found that the rectangular shape of dendrites cut perpendicular to their main direction of growth is not the limit of the crystal orientation of the dendrite but can also be present in the surrounding crystals of diverse morphology.

It was also shown that the crystal structures located between the dendritic crystals are the result of a second step of crystallization as they copy the orientation of their respective parent crystals through epitaxial growth, even when the latter deviate from the main orientation of the dendrite. A Ti-free high temperature phase of barium disilicate ( $\text{Ba}_2\text{Si}_4\text{O}_{10}$ ), chemically not distinguishable from the low temperature phase sanbornite, could also be identified by EBSD through its crystal symmetry. This work has recently been published [61].

The contribution of EBSD to the analysis of mullite glass-ceramics grown via electrochemically induced nucleation began with the information that crystal orientation within a cross section of a needle can vary up to  $5^\circ$  and that the c-axis is usually oriented toward the area of nucleation, e.g. the platinum wire. In contrast to the previous understanding of oriented nucleation near the cathode, random nucleation was shown to occur. The orientation of the mullite crystals is only a result of the experimental setup. The needle like growth of mullite under the given settings was confirmed, even when the visual impression from SEM-micrographs would suggest that curved crystal growth would be possible. It was also shown that the orientation of a crystal can change due to interactions with an obstacle (e.g. the Pt-wire).

### 4.3. Bulk Crystallization

The EBSD-analysis of glass-ceramics with high iron content showed the peculiar formation of a mantle of magnetite crystals around a core of hematite in what was probably a stria in the glass. While the hematite core showed an orientation similar to that of glass-ceramics oriented through extrusion, no specific orientation could be described for the magnetite mantle. Application of the crystallization morphology observed in the sample 1 of publication 2.7 to the sample 2 of the same publication lead to the deduction that hematite was the primary phase formed during the crystallization of this sample. This was further cemented by the findings of EBSD-analysis which enabled the formulation of a strict orientation relation between the hematite and magnetite areas of crystals in the sample: it was shown that the [0001]-direction of the hematite phase is parallel to the [111]-direction of the magnetite phase occurring in the same crystal. Two magnetite orientations, rotated by  $60^\circ$  to one another, occur and can be explained by the transformation of the A-B stacking order of hexagonal hematite into A-B-C or A-C-B layers of magnetite, respectively. This orientation relationship was shown to be valid for a number of independent crystals allowing the conclusion that this orientation relationship is valid for all the crystals in the sample. It was further shown that the phase transformation is accompanied by a morphological restructuring of the crystals.

## 5. References

- [1] G.H. Beall: Design and properties of glass ceramics, *Ann. Rev. Mater. Sci.* **1992**, *22*, 91-119.
- [2] R.P.F. de Almeida, C. Bocker, C. Rüssel: Size of CaF<sub>2</sub> crystals precipitated from glasses in the Na<sub>2</sub>O/K<sub>2</sub>O/CaO/CaF<sub>2</sub>/Al<sub>2</sub>O<sub>3</sub>/SiO<sub>2</sub> system and percolation theory, *Chem. Mater.* **2008**, *20*, 5916-5921.
- [3] C. Bocker, S. Bhattacharyya, T. Höche, C. Rüssel: Size distribution of BaF<sub>2</sub> nanocrystallites in transparent glass ceramics, *Acta Mater.* **2009**, *57*, 5956–5963.
- [4] S. Bhattacharyya, C. Bocker, T. Heil, J.R. Jinschek, T. Höche, C. Rüssel, H. Kohl: Experimental Evidence of Self-Limited Growth of Nanocrystals in Glass, *Nano Lett.* **2009**, *9*, 2493-2496.
- [5] S. Tanabe, H. Hayashi, T. Hanada, N. Onodera: Fluorescence properties of Er<sup>3+</sup> ions in glass ceramics containing LaF<sub>3</sub> nanocrystals, *Opt. Mater.* **2002**, *19*, 343–349.
- [6] M.J. Dejneka: The luminescence and structure of novel transparent oxyfluoride glass-ceramics, *J. Non-Cryst. Solids* **1998**, *239*, 149–155.
- [7] A.C. Yanes, J. Del-Castillo, J. Mendez-Ramos, V.D. Rodriguez, M.E. Torres, J. Arbiol: Luminescence and structural characterization of transparent nanostructured Eu<sup>3+</sup>-doped LaF<sub>3</sub>-SiO<sub>2</sub> glass-ceramics prepared by sol-gel method, *Opt. Mater.* **2007**, *29*, 999–1003.
- [8] A. Biswas, G.S. Marciel, R. Kapoor, G.S. Friend, P.N. Prasad: Upconversion properties of a transparent Er<sup>3+</sup>-Yb<sup>3+</sup> co-doped LaF<sub>3</sub>-SiO<sub>2</sub> glass-ceramics prepared by sol-gel method, *J. Non-Cryst. Solids* **2003**, *316*, 393–397.
- [9] Z.J. Hu, Y.S. Wang, F. Bao, W.Q. Luo: Crystallization behavior and micro structure investigations on LaF<sub>3</sub> containing oxyfluoride glass ceramics, *J. Non-Cryst. Solids* **2005**, *351*, 722–728.
- [10] A. Halliyal, A. Safari, A.S. Bhalla, R.E. Newnham, L.E. Cross: Grain-Oriented Glass-Ceramics for Piezoelectric Devices, *J. Am. Ceram. Soc.* **1984**, *67*, 331–335.
- [11] R.Y. Ting, A. Halliyal, A.S. Bhalla: Polar glass ceramics for sonar transducers, *Appl. Phys. Lett.* **1984**, *44*, 852–854.
- [12] C. Rüssel: Oriented crystallization of glass. A review, *J. Non-Cryst. Solids* **1997**, *219*, 212–218.
- [13] H. Masai, T.J. Fujiwara: Dual layered surface crystallization of 30BaO–15TiO<sub>2</sub>–55GeO<sub>2</sub> glass by stepwise heat treatment, *Appl. Phys.* **2007**, *101*, 033530.
- [14] Y. Hane, T. Komatsu, Y. Benino, T. Fujiwara: Transparent nonlinear optical crystallized glass fibers with highly oriented Ba<sub>2</sub>TiGe<sub>2</sub>O<sub>8</sub> crystals *Appl. Phys.* **2008**, *103*, 063512.
- [15] D. Tauch, C. Rüssel: Glass–ceramics with zero thermal expansion in the system BaO/Al<sub>2</sub>O<sub>3</sub>/B<sub>2</sub>O<sub>3</sub>, *J. Non-Cryst. Solids* **2005**, *351*, 2294-2298.
- [16] I. Szabó: Crystallization of magnesium aluminosilicate glasses *J. Non-Cryst. Solids* **1997**, *219*, 128-135.
- [17] R. Keding, C. Rüssel: Oriented Crystallisation of Fresnoite in an Electric Field *Ber. Bunsenges. Phys. Chem.* **1997**, *100*, 1515-1518.
- [18] G. von der Gönna, R. Keding, C. Rüssel: Oriented growth of mullite from a glass melt using electrochemical nucleation *J. Non-Cryst. Solids* **1999**, *243*, 109-115.
- [19] R. Keding, C. Rüssel: Oriented strontium fresnoite glass-ceramics prepared by electrochemically induced *J. Mater. Sci.* **2004**, *39*, 1433-1435.
- [20] R. Keding, D. Stachel, C. Rüssel: Oriented fluororichterite/diopsid glass-ceramics prepared by electrochemically induced nucleation *J. Non-Cryst. Solids* **2001**, *283*, 137-143.

- [21] K. Gerth, C. Rüssel, R. Keding, P. Schleevoigt, H. Dunken: Oriented crystallisation of lithium niobate containing glass ceramic in an electric field and determination of the crystallographic orientation by infrared spectroscopy *Eur. J. Glass Sci. Technol. B*, 1999, **40**, 135-139.
- [22] O. Anspach, R. Keding, C. Rüssel: Oriented lithium disilicate glass–ceramics prepared by electrochemically induced nucleation *J. Non-Cryst. Solids* 2005, **351**, 656-662.
- [23] T. Honma, Y. Benino, T. Fujiwara, R. Sato, T. Komatsu: New optical nonlinear crystallized glasses and YAG laser-induced crystalline dot formation in rare-earth bismuth borate system, *Opt. Mater.* **2002**, *20*, 27–33.
- [24] T. Honma, R. Ihara, Y. Benino, R. Sato, T. Fujiwara, T. Komatsu: Writing of crystal line patterns in glass by laser irradiation, *J. Non-Cryst. Solids* **2008**, *354*, 468–471.
- [25] R. Nagai, T. Honma, T. Komatsu: Laser Patterning of ZnO Crystals on the Surface of Borosilicate Glass, *J. Am. Ceram. Soc.* **2010**, *93*, 658–661.
- [26] F. Suzuki, T. Honma, T. Ishibashi, T. Komatsu, Y. Doi, Y. Hinatsu: Synthesis and laser patterning of Bi-doped Y<sub>3</sub>Fe<sub>5</sub>O<sub>12</sub> crystals in germanosilicate glasses, *J. Phys. Chem. Solids* **2010**, *71*, 906–912.
- [27] K.H.G. Ashbee: Anisotropic glass-ceramics produced by extrusion through opposed dies, *J. Mater. Sci.* **1975**, *10*, 911-917.
- [28] S. Habelitz, T. Höche, R. Hergt, G. Carl, C. Rüssel: Microstructural Design through Epitaxial Growth in Extruded Mica Glass-Ceramics, *Acta. Mater.* **1999**, *47*, 2831-2840.
- [29] D.I.H. Atkinson, P.W. McMillan: Glass-ceramics with random and oriented microstructures, *J. Mater. Sci.* **1977**, *12*, 443-450.
- [30] S. Habelitz, G. Carl, C. Rüssel, S. Thiel, U. Gerth, J.D. Schnapp, A. Jordanov, H. Knake: Mechanical properties of oriented mica glass ceramic, *J. Non-Cryst. Solids* **1997**, *220*, 291-298.
- [31] C. Moisescu, C. Jana, S. Habelitz, G. Carl, C. Rüssel: Oriented fluoroapatite glass-ceramics, *J. Non-Cryst. Solids* **1999**, *248*, 176-182.
- [32] I. Avramov, G. Völksch: Near-surface crystallization of cordierite glass. *J. Non-Cryst. Solids* **2002**, *304*, 25-30.
- [33] A.J. Schwartz, M. Kumar, B.L. Adams: Electron Backscatter Diffraction in Materials Science, Kluwer Academic/ Plenum Publishers, New York 2000.
- [34] A. Deal, T. Hooghan, A. Eades: Energy-filtered electron backscatter diffraction, *Ultramicroscopy* **2008**, *108*, 116-125.
- [35] L. Reimer: Scanning Electron Microscopy, Springer, Berlin 1985.
- [36] A. Winkelmann, C.S. Fadley, F.J.G. Abajo: High-energy photoelectron diffraction: model calculations and future possibilities, *New J. Phys.* **2008**, *10*, 113002.
- [37] R.E. DeWames, W.F. Hall: A Wave Mechanical Description of Electron and Positron Emission from Crystals, *Acta Crystallogr.* **1968**, *A 24*, 206-212.
- [38] D. Dingley: Progressive steps in the development of electron backscatter diffraction and orientation imaging microscopy, *J. Microsc.* **2004**, *213*, 214-224.
- [39] D. Dingley, V. Randle: Review - Microtexture determination by electron back- scatter diffraction, *J. Mater. Sci.* **1992**, *27*, 4545-4566.
- [40] K.Z. Baba-Kishi: Electron backscatter Kikuchi diffraction in the scanning electron microscope for crystallographic analysis, *J. Mater. Sci.* **2002**, *37*, 1715–1746.
- [41] B.S. El-Dasher, B.L. Adams, A.D. Rollett: Experimental recovery of geometrically necessary dislocation density in polycrystals, *Scripta Mater.* **2003**, *48*, 141-145.
- [42] V. Randle: Electron backscatter diffraction: Strategies for reliable data acquisition and processing, *Mater. Charact.* **2009**, *60*, 913-922.
- [43] A. Bhattacharyya, J. Eades: Use of an energy filter to improve the spatial resolution of electron backscatter diffraction, *Scanning* **2009**, *31*, 114-121.

- [44] C.D. Barrie, A. P. Boyle, N. J. Cook, D. J. Prior: Pyrite deformation textures in the massive sulfide ore deposits of the Norwegian Caledonides, *Tectonophysics*, **2010**, 483, 269-286.
- [45] C.D. Barrie, A.P. Boyle, M. Salter: How low can you go? Extending downwards the limits of plastic deformation in pyrite, *Mineral. Mag.*, **2009**, 73, 895-913.
- [46] I. Romeo, R. Capote, R. Lunar, N. Cayzer: Polyminerale orientation analysis of magmatic rocks using Electron Back-Scatter Diffraction: Implications for igneous fabric origin and evolution, *Tectonophysics*, **2007**, 444, 45-62.
- [47] J.P. Craddock, A.W. McKiernan: Tectonic implications of finite strain variations in Baraboo-interval quartzites (ca. 1700 Ma), Mazatzal orogen, Wisconsin and Minnesota, USA, *Precambrian Res.*, **2007**, 156, 175-194.
- [48] M. Palizdar, Y. Palizdar, T.P. Comyn, A.J.: Electron Backscattered Diffraction of MonoCrystalline Bismuth Titanate, *J. Am. Ceram. Soc.* **2010**, 93, 3604-3606.
- [49] L. Zhang, J. Vleugels, O. Van der Biest: Fabrication of textured alumina by orienting template particles during electrophoretic deposition, *J. Eur. Ceram. Soc.* **2010**, 30, 1195-1202.
- [50] L.Y. Zhang, M.L. Qin, X.H. Qu, Y.L. Lu, X.Y. Zhang: Microstructure and Mechanical Property Analysis of AlN Ceramic with Mo-Ni-Cu Alloy Active Braze Joints, *J. Inorg. Mater.*, **2009**, 24, 636-640.
- [51] A.J. DeArdo, M. J. Hua, K. G. Cho, C. I. Garcia: On strength of microalloyed steels: an interpretive review, *Mater. Sci. Tech-Lond.*, **2009**, 25, 1074-1082.
- [52] R. Penelle: Nucleation and growth during primary recrystallization of certain metals and alloys with a face-centered cubic structure: Formation of the cube texture, *Int. J. Mater. Res.*, **2009**, 24, 636-640.
- [53] Z. Zhu, B.P. Wynne, E. Ghassemieh, A. Siddiq: Microstructural Analysis of Ultrasonic Welded AA6061 by Electron Backscattered Diffraction, *Rare Metal Mat. Eng.*, **2009**, 38, 147-151.
- [54] Y.M. Huang, Y.M. Wu, C.X. Pan: EBSD study of solidification characteristics of austenitic stainless steel weld pool, *Mater. Sci. Tech-Lond.*, **2010**, 26, 750-753.
- [55] G. Völksch, R. Harizanova, C. Rüssel, S. Mitsche, P. Pölt: Crystallization in High Iron Containing Silicate Glasses – Electron Microscopy Investigations, *Glass. Sci. Technol.* **2004**, C 77, 438–441.
- [56] R. Carl, G. Völksch, C. Rüssel: Electron microscopic investigations of electrochemically induced mullite crystallisation in a glassy matrix, *Adv. Mater. Res.*, **2008**, 39-40, 387-390.
- [57] A.D. Rollett, S.-B. Lee, R. Campman, G.S. Rohrer: Three-Dimensional Characterization of Microstructure by Electron Back-Scatter Diffraction, *Annu. Rev. Mater. Res.* **2007**, 37, 627-658.
- [58] R. Wirth: Focused Ion Beam (FIB) combined with SEM and TEM: Advanced analytical studies of chemical composition, microstructure and crystal structure in geomaterials on a nanometre scale, *Chem. Geol.* **2009**, 261, 217–229.
- [59] V. Randle: Applications of electron backscatter diffraction to materials science: status in 2009, *J. Mater. Sci.* **2009**, 44, 4211–4218.
- [60] W. Wisniewski, G. Völksch, C. Rüssel: The Degradation of EBSD-Patterns as a Tool to Investigate Surface Crystallized Glasses and to Identify Glassy Surface Layers. submitted *Ultramicroscopy*.
- [61] M. Nagel, W. Wisniewski, G. Völksch, C. Borschel, C. Ronning, C. Rüssel: Composition and texture of barium silicate crystals in fresnoite glass-ceramics by various scanning electron microscopic techniques. CrystEngComm (2011) DOI: 10.1039/c0ce00876a.

## 6. Abbreviations

$\lambda$	wavelength
$\Theta_B$	Bragg angle
CCD	<u>charge coupled device</u>
CI	<u>confidence index</u>
$d_{hkl}$	lattice plane spacing
DTA	<u>differential thermal analysis</u>
e	elementary charge of an electron
E	energy
EBS	<u>electron backscatter diffraction</u>
EBSP	<u>electron backscattering pattern</u>
EDX	<u>energy dispersive X-ray spectroscopy</u>
EPR	<u>electron paramagnetic resonance</u>
FEG	<u>field emission gun</u>
h	Planck's constant
IPF	<u>inverse pole figure</u>
IQ	<u>image quality</u>
n	diffraction order
OIM	<u>orientation image mapping</u>
p	momentum
PF	<u>pole figure</u>
SEM	<u>scanning electron microscope</u>
U	accelerating voltage
XRD	X-ray diffraction



## 7. Presentations

- 7.1. “Electron Backscatter Diffraction und Orientation imaging Microscopy”  
Otto Schott Institut, Jena University (2008)
- 7.2. “Electron Backscatter Diffraction zur Untersuchung von Glaskeramiken“  
Technical Committee 1 “Physics and Chemistry of Glasses” of the German Glass Society (DGG) (2008)
- 7.3. “Electron Backscatter Diffraction zur Untersuchung Fresnoithaltiger Glaskeramiken“  
German Society of Material Science (DGM)/ German Society of Materials Research and -Testing (DVM) Research Group-Meeting EBSD (2009)
- 7.4. “Nachweis von Texturen in Fresnoit-Glaskeramiken“  
Otto Schott Institut, Jena University (2009)
- 7.5. “Oberflächenkristallisation von Fresnoit“  
Otto Schott Institut, Jena University (2009)
- 7.6. “Charakterisierung von BaAl<sub>2</sub>B<sub>2</sub>O<sub>7</sub>-Glaskeramiken mit EBSD”  
German Society of Material Science (DGM)/ German Society of Materials Research and -Testing (DVM) Research Group-Meeting EBSD (2010)
- 7.7. “Oriented surface crystallization in glasses”  
10th Conference of the European Society of Glass Science and Technology (ESG) (2010)
- 7.8. “Oberflächliche Orientierungsänderungen von Cordieritkristallen in 6 B<sub>2</sub>O<sub>3</sub>·10 MgO·25 Al<sub>2</sub>O<sub>3</sub>·59 SiO<sub>2</sub> – Glas”  
Otto Schott Institut, Jena University (2010)

## 8. Posters

- 8.1. “Texturen in Glaskeramiken“  
W. Wisniewski, M. Nagel, C. Rüssel, 83. Glastechnische Tagung, Amberg (2009)
- 8.2. “Cathodoluminescence of fresnoite glass-ceramics”  
M. Nagel, G. Völksch, W. Wisniewski, C. Borschel, C. Ronning, C. Rüssel, 10th Conference of the European Society of Glass Science and Technology (ESG), Magdeburg (2010)
- 8.3. “Orientierte Keimbildung in oberflächenkristallisierten Glaskeramiken“  
W. Wisniewski, M. Nagel, T. Zscheckel, G. Völksch, C. Rüssel, Messe „GlasTech“, Düsseldorf (2010)

## **9. Acknowledgements**

I would like to thank all my friends and colleagues for their respective contributions to this thesis. More precisely I would like to thank Gabi Möller for the sample preparation so essential to EBSD, Thomas Kittel for his contributions in optical microscopy, LSM and AFM measurements and Dr. Matthias Müller for the XRD measurements featured in this thesis. Further I would like to thank Prof. Dörte Stachel for her kind encouragement, especially during my time as a student. Of course coauthors Marcus Nagel, Tilman Zscheckel, Dr. Robert Carl and Dr. Ruzha Harizanova contributed significantly to this thesis in the form of creative discussions and sample fabrication.

Special thanks are in order to Dr. Günter Völksch for introducing me to electron microscopy and EBSD as well as general aspects of scientific work. Finally, I would like to thank Prof. Christian Rüssel for his mentoring of this thesis as well as his support during the interpretation and publication of the results.

## **Danksagung**

Hiermit möchte ich mich bei allen Freunden und Kollegen für ihren jeweiligen Beitrag zu dieser Arbeit bedanken. Konkret möchte ich Gabi Möller für die aufwändige Probenpräparation bedanken, ohne die EBSD nicht möglich ist. Dank gebührt weiterhin Thomas Kittel für die Untersuchungen mittels optischer Mikroskopie, der LSM und AFM, sowie Dr. Matthias Müller für die XRD-Messungen. Weiterhin möchte ich mich bei Prof. Dörte Stachel für ihre freundliche Unterstützung, besonders während des Studiums, bedanken. Natürlich gebührt den Koautoren Marcus Nagel, Tilman Zscheckel, Dr. Robert Carl und Dr. Ruzha Harizanova Dank für ihre Beiträge in Form von kreativen Diskussionen und Probenherstellung.

Besonderen Dank verdient Dr. Günter Völksch für seine Einführung in die Elektronenmikroskopie und EBSD sowie allgemeine Aspekte wissenschaftlichen Arbeitens. Schließlich möchte ich Prof. Christian Rüssel für die Betreuung dieser Arbeit und der Unterstützung bei der Auswertung und Publikation der Ergebnisse danken.

## **10. Statement**

I hereby state that this thesis has not been previously submitted to any university to initiate the conferral of a doctorate. All content obtained from references is marked and the references have been denoted.

Jena, the 28.th of January 2011

Wolfgang Wisniewski

## **Erklärung**

Ich erkläre, dass ich die vorliegende Arbeit selbständig und unter Verwendung der angegebenen Hilfsmittel, persönlichen Mitteilungen und Quellen angefertigt habe.

Jena, den 28. Januar 2011

Wolfgang Wisniewski

## 11. Curriculum Vitae / Lebenslauf

**Dipl. Ing. Wolfgang Wisniewski**  
Saalbahnhofstr. 25  
07743 Jena

Email: wolfgang.w@uni-jena.de  
geboren am 18. Mai 1982 in Jena

### Ausbildung und Studium:

- seit Okt. 2008            **Doktorand am Otto-Schott-Institut der Universität Jena**
- Nov. 2008                **Weiterbildung (1 Woche)**  
*EDAX/TSL „Pegasus“ Einweisungskurs der Fa. AMETEK GmbH*  
(Wiesbaden)
- Sept. 2008               **Diplom-Ingenieur** an der **Universität Jena**
- Juli 2007                 **Weiterbildung (2 Wochen) „Zerstörungsfreie Prüfung**  
*Grundlagenkenntnisse zur Stufe 3“* nach DIN EN 473 (Jan. 2006)  
**Deutsche Gesellschaft für Zerstörungsfreie Werkstoffprüfung e.V.**  
(Berlin)
- Okt. 2003 -  
Aug. 2008                **Studium der Werkstoffwissenschaft an der Universität Jena**  
**Diplomarbeit** zur Anwendbarkeit von EBSD auf Glaskeramiken  
**(Dr. G. Völksch, Prof. C. Rüssel)**
- Studienarbeit** zur Leitfähigkeit von Erbium substituierten Bismutoxid  
**(Dr. R. Kriegel, Prof. D. Stachel)**
- Komplexpraktikum** Lasermaterialbearbeitung **(Dr. G. Staupendahl)**
- Komplexpraktikum** Glasfaserziehen                    **(Dr. L. Kido)**
- Juni 2001                 **Abitur** mit **Latinum** am Adolf- Reichwein Gymnasium in Jena
- 1990 – 1992              **Green Meadow Waldorf School** in Spring Valley/ **New York (USA)**
- 1988 – 1990              **Grundschule** in Jena

**Berufliche Tätigkeit:**

- seit Okt. 2008      *Wissenschaftlicher Mitarbeiter* am **Otto-Schott-Institut** (Jena)
- Nov. - Dez. 2007    *Praktikant* bei der **Docter Optics GmbH** (Neustadt/Orla)
- Sept. - Okt. 2006    *Praktikant* am **Hermsdorfer Institut für Technische Keramik e.V.**(Hermsdorf)
- Aug. 2002 -  
Mai 2003            *Reise durch Australien*, Arbeit in der **Holzindustrie, Landwirtschaft**  
und **Tourismusbranche**
- Okt. 2001-  
Juli 2002            *Zivildienst* am **Universitätsklinikum Jena** als **Stationshilfe**  
(Klinik für Innere Medizin, Onkologie)

**Soziales Engagement:**

- 2005 - 2010        *Ehrenamtliches Engagement* im *Kletterwandausschuss* der  
Kletterhalle des Alpenvereins in Jena (Verwaltung der Halle,  
Wettkampfororganisation, Abrechnungen)
- seit 2004            *Ehrenamtliches Engagement* in der *Kletterhalle des Alpenvereins* in  
Jena (Betreuung öffentlicher Kletterzeiten und Jugendgruppen)
- 1998 - 2004        *Ehrenamtliches Engagement* als *Jugendwart* beim *See Sport Club-  
Jena e.V.*

**Sprachkenntnisse:**    fließend Englisch

**Computerkenntnisse:** Softwarepaket EDAX/TSL (EBSD, EDX, WDX), REM-Software der  
Fa. Jeol, Xara Xtreme, Sigma Plot, Irfan View, Hugin, sicherer Umgang  
mit Windows, Word, Powerpoint, Excel und dem Internet

Jena, den

Wolfgang Wisniewski